

Relativistic Analysis of the Constituent Quark Model for Mesons

Peter C. Tiemeijer

Relativistic Analysis of the
Constituent Quark Model for Mesons

CIP-GEGEVENS KONINKLIJKE BIBLIOTHEEK, DEN HAAG

Tiemeijer, Peter Christiaan

Relativistic analysis of the constituent quark model for mesons / Peter Christiaan Tiemeijer. - Utrecht : Universiteit Utrecht, Faculteit Natuur- en Sterrenkunde Proefschrift Universiteit Utrecht. -Met lit. opg. - Met samenvatting in het Nederlands.
ISBN 90-393-0427-0

Trefw.: elementaire deeltjes.

Relativistic Analysis of the Constituent Quark Model for Mesons

Relativistische analyse van het bouwsteen-quarkmodel voor mesonen

(met een samenvatting in het Nederlands)

Proefschrift

ter verkrijging van de graad van doctor aan de
Universiteit Utrecht, op gezag van de Rector
Magnificus Prof. Dr. J.A. van Ginkel, ingevolge
het besluit van het College van Decanen
in het openbaar te verdedigen op woensdag
8 september 1993 des namiddags te 2.30 uur

door

Peter Christiaan Tiemeijer

geboren op 4 februari 1966 te Son en Breugel

Promotor: Prof. Dr. J.A. Tjon

Instituut voor Theoretische Fysica
van de Universiteit Utrecht

Dit proefschrift kwam tot stand met de financiële steun van de Stichting voor Fundamenteel Onderzoek der Materie (FOM), die financieel wordt gesteund door de Nederlandse Organisatie voor Wetenschappelijk Onderzoek (NWO).

Abstract.

Extensions of the constituent quark potential model for mesons are formulated and analyzed which include relativistic dynamics and the full Dirac structure of both positive and negative energy states. The meson wave equations are transformed to configuration space where they can easily be solved numerically. Thus we present the first systematic description of the mass spectra of light, mixed and heavy mesons which takes into account the full Dirac structure without approximations. The pion form factor and radiative, leptonic and electroweak meson decay are studied. We find that the projection on the full Dirac structure of the confining potential and of the meson decay vertices gives unexpected large modifications to the nonrelativistic mass spectra and decay vertices.

Contents

1	Introduction and overview	1
2	Meson mass spectrum	9
2.1	Introduction	9
2.2	The quasipotential equations	11
2.2.1	Blankenbecler-Sugar-Logunov-Tavkhelidze equation	12
2.2.2	Equal-time approximation	15
2.3	The interaction	17
2.4	Parameter dependence	20
2.5	Confining force and Regge-trajectories	26
2.6	Meson mass spectrum	30
2.6.1	Improving the heavy meson spectrum	37
2.7	Concluding remarks	39
2.A	Partial wave projection	40
2.A.1	Blankenbecler-Sugar-Logunov-Tavkhelidze equation	40
2.A.2	Equal-time approximation	43
2.A.3	Potential	45
2.B	Short distance behavior of 1S_0 states	46
2.B.1	Blankenbecler-Sugar-Logunov-Tavkhelidze equation	46
2.B.2	Equal-time approximation	48
2.C	Bethe-Salpeter equation	49
3	Effects of negative energy components	53
3.1	Introduction	53
3.2	Review of model	54
3.3	Results	56
3.3.1	Comparison with Schrödinger equation results	57
3.3.2	Equal-time results	59
3.3.3	Sensitivity to vector confinement	60
3.4	Concluding remarks	60

4	Reactions	67
4.1	Meson current	67
4.1.1	Bethe-Salpeter current	67
4.1.2	Quasipotential current	70
4.2	Radiative decay	73
4.2.1	Nonrelativistic reduction	74
4.2.2	Comparison with nonrelativistic results	77
4.2.3	Parameter dependence	82
4.2.4	Comparison with experiment	82
4.2.5	Concluding remarks	86
4.3	Electromagnetic form factors	87
4.4	qq annihilation decay	90
4.4.1	Renormalization of $\psi(0)$	91
4.4.2	Numerical implementation	92
4.4.3	Calculated annihilation probabilities	96
4.4.4	Concluding Remarks	100
5	Samenvatting	101
	References	107
	Curriculum vitae	111

Chapter 1

Introduction and overview

The constituent quark potential model gives a simple and appealing description of mesons and baryons based on Quantum Chromo-Dynamics. In this model the elementary current quark fields of QCD are thought of as being dressed by clouds of virtual gluons and quarks. These extended quarks are the constituent quarks and they are treated as the basic degrees of freedom in the constituent quark model. Their charge, spin and flavor is equal to those of the current quarks but their masses can be much larger. A constituent quark-antiquark pair constitutes a meson and three constituent quarks build a baryon. This model offers a good qualitative understanding of observed masses and reaction probabilities of hadrons, and it gives remarkably good quantitative results in the low energy range of the heavy mesons.

This thesis gives an analysis of the role of relativity in the constituent quark model for mesons. This analysis is interesting for two reasons. In the first place we hope to get a better understanding of why the nonrelativistic constituent quark model offers such a good qualitative and quantitative description of hadron properties. This description is considerably better than can be expected from a simple estimate of the sizes of the relativistic effects. The second reason is related to the ongoing increase of energy and complexity of reactions considered in nuclear experiments and theories. This increase makes it worthwhile to look for hadron models which also give reliable quantitative results under these more extreme situations. At present it is not possible to extract numbers from QCD without making some simplifications, and all hadron models contain some of them. A clear understanding of the effects of these approximations helps to assess the reliability of these hadron models. In particular, the study of relativistic effects in the constituent quark model gives an indication of the reliability of the results obtained within the nonrelativistic model, and of the possibilities for applying the nonrelativistic model at high energies.

In the remainder of this introduction and overview we sketch how we extend the nonrelativistic constituent quark model to include various relativistic features and we present and discuss our results.

In the nonrelativistic constituent quark model the meson is basically described by the Schrödinger equation

$$\left[\frac{p^2}{m} + 2m - \frac{\alpha}{x} + \kappa x + c \right] \psi = M\psi. \quad (1.1)$$

The quark-antiquark interaction is modeled as the sum of a Coulomb-like α/x potential which comes from the short range one-gluon-exchange interaction, and a linearly rising part responsible for the confinement. Overviews of the results and successes of the nonrelativistic approach are given in Refs. [25, 50, 52]. Yet the motion of quarks inside hadrons can hardly be called nonrelativistic and authors have been taking the relativistic dynamics into account in various ways. A comparatively simple extension of the nonrelativistic Schrödinger equation was made by Isgur and co-workers [29] which led to a gauge point for further work in this area. In this work the nonrelativistic kinetic energy is relativized by replacing $p^2/2m + m \rightarrow \omega = \sqrt{p^2 + m^2}$, and various relativistic effects are parametrized by non-localities of the form m/ω .

A more ambitious approach is based on the generalization of the Schrödinger equation to the relativistic covariant Bethe-Salpeter equation (BSE)

$$S^{-1}(p)\psi(p) = - \int \frac{d^4 p'}{i(2\pi)^4} V(p-p') \psi(p') \quad (1.2)$$

(the dependence on the total momentum has been suppressed in this notation). The BSE differs from the nonrelativistic equation in two respects. The first difference is that the dependence of the bound state wave function ψ and the potential V on the relative three-momentum \mathbf{p} is extended to a dependence on the four momentum (p_0, \mathbf{p}) . Relativistic covariance also requires that for fermions the full Dirac structure is taken into account, and thus the second difference is that for quarks not only the positive energy states need to be considered but also their negative energy states must be included. At present the BSE for mesons has not been solved without approximations. The first obstacle is the numerical work involved which is highly non-trivial. A second and more fundamental obstacle is posed by the extension of the nonrelativistic confining potential to a four-momentum dependence. It is only known for the static case and no underlying theory is available that can give a prescription on how to extend it to a covariant form.

In view of these obstacles we restrict our investigations to quasipotential (QP) approximations to the BSE in which the p_0 dependence of the quark propagators is eliminated. The covariant Dirac structure can be kept in these. A well-known example of a QP approximation is the instantaneous or equal-time or Salpeter equation [65]. Here the Bethe-Salpeter propagator $S(p_0, \mathbf{p}) = S_1(p_1)S_2(p_2)$, which is the

product of the two one-body Dirac propagators, is simplified by integrating out the relative energy variable and replacing

$$S(p_0, \mathbf{p}) \rightarrow S_{\text{Salp}}(p_0, \mathbf{p}) = \delta(p_0) \left[\int \frac{dq_0}{2\pi i} S(q_0, \mathbf{p}) \right] \quad (1.3)$$

in the BSE, which leads to the Salpeter equation

$$S_{\text{Salp}}^{-1}(\mathbf{p})\psi(\mathbf{p}) = - \int \frac{d\mathbf{p}'}{(2\pi)^3} V(\mathbf{p} - \mathbf{p}') \psi(\mathbf{p}'). \quad (1.4)$$

The Salpeter equation and the potential and the wave functions do no longer depend on p_0 . This thesis concentrates on two QP equations, which are discussed in Section 2.2. The first (referred to as ET) is an extension of the Salpeter or equal-time equation proposed by Mandelzweig and Wallace [56, 73, 74]. For equal mass particles its propagator reads

$$S_{\text{ET}}^{-1}(\mathbf{p}) = 2(\omega - E)\Lambda^{++} - 2\omega(\Lambda^{+-} + \Lambda^{-+}) + 2(\omega + E)\Lambda^{--}, \quad (1.5)$$

where $E = M/2$ is half the meson mass and the $\Lambda^{\rho'\rho}$ project upon the various combinations of positive and negative energy states. The second is a generalization by Cooper and Jennings [17] of the Blankenbecler-Sugar-Logunov-Tavkhelidze (BSLT) equation [9]. For equal mass particles its propagator becomes

$$S_{\text{BSLT}}^{-1}(\mathbf{p}) = 4\omega \left[\frac{\omega - E}{\omega + E}\Lambda^{++} - \Lambda^{+-} - \Lambda^{-+} + \frac{\omega + E}{\omega - E}\Lambda^{--} \right]. \quad (1.6)$$

Both QP equations contain the full Dirac structure and reduce to the one-body Dirac equation in the one-body limit. We use the usual nonrelativistic interaction as in Eq. (1.1), and replace α by a running coupling constant. We take the Lorentz structure of the confining potential to be mostly scalar, but we do allow for some amount of vector confinement.

It seems obvious to solve the QP equations in momentum space because of the various momentum dependent factors that appear in them. Here one encounters a third obstacle namely that the Fourier transform to momentum space of the confining potential is highly singular at zero momentum transfer. From $V(p=0) = \int d^3x V(x)$ and the monotonic increase of the confining potential $V(x)$ one easily finds that $V(p)$ diverges stronger than p^{-3} for small momenta. Many authors have encountered this problem. Approximations to the infinitely rising potential are used in the Schwinger-Dyson-like calculations of Refs. [43, 63], where the confining potential is simply replaced by a delta function of the four-momentum. A less drastic approximation is to replace the confining potential by a rising function which drops to zero at some large cutoff distance [3, 19, 35, 41]. However, it is not necessary to approximate

the confining potential as shown by Refs. [38, 58, 72] who apply a partial integration to the singularity in the integral over the product of the potential and the wave function. This leads to Cauchy principal value integral which is well-suited for numerical evaluation (this method is probably also used in [28, 42, 47]). The singularity can also directly be regularized to a principal value integral by employing a proper subtraction term in the potential [32, 37, 59]. To our knowledge only a small number of relativistic meson spectra calculations have been published [37, 38, 59, 72], of which only [37] considers the light and heavy mesons simultaneously. None of these incorporate the full Dirac structure.

In this work we do not switch to momentum space but instead we Fourier transform the QP propagators to configuration space. If a proper choice of Dirac basis states is employed, i.e. the basis consisting of upper and lower components, then the potential becomes diagonal and local, and momentum dependent functions only appear in the QP propagator. This makes the partial wave projection and the Fourier transformation rather simple, as can be seen from the expressions in Appendix 2.A. In this way we are able to present the first systematic analysis of the mass spectra of the light, mixed and heavy mesons which includes the full Dirac spinor structure without approximations.

Certain difficulties as found in the one-particle Dirac equation also appear in the QP approach and set limitations on the physically allowed QP parameters. Let us for a moment consider one fermion in an external potential. If this particle experiences a potential which fluctuates more strongly than $\sim 2m$ over a distance shorter than its Compton length $x_C = 1/m$ new fermion-antifermion pairs can be created. This phenomenon cannot correctly be described by the Dirac equation which describes a one-particle theory and thus misses the interactions between the newly created pair and the starting particle. Since the Dirac equation does allow for antifermion components, solutions in this potential can have an unbound number of non-interacting fermions and antifermions, thus being unnormalizable and unphysical. This break-down of the Dirac equation is well-known as the Klein paradox [8]. Similar flaws emerge in the QP equations since they also contain negative energy components. Unbound solutions can be expected if the confining strength becomes too strong, $\kappa x_C \gtrsim 2m$ or $\kappa \gtrsim 2m^2$. Such values can be reached in light meson systems. The condition on κ depends on the Lorentz structure of the confining potential and is discussed in Section 2.5. The upper bound on κ disappears if the negative energy components are removed.

Similarly, if the OGE potential becomes too strong, $\alpha/x_C \gtrsim 2m$ or $\alpha \gtrsim 2$, solutions occur which are irregular at the origin and which represent the tumbling of the wave function in the OGE well. If the coupling constant of the OGE is below this maximal value, the wave function is normalizable but still divergent at the origin. Mesons with high orbital angular momenta are less sensitive to this effect because the centrifugal barrier hinders them in entering the short distance region. Taking a

running coupling constant instead of a fixed coupling removes the irregular solutions and diminishes the singular behavior. If the negative energy components are omitted, then the upper bound on α is shifted upward but it remains present. For an accurate solution of the QP equations the divergence must be analyzed and incorporated explicitly into the QP equation or QP wave functions. This analysis is carried out in Appendix 2.B. Other relativistic frameworks where the divergent behavior appears and for which it has been analyzed are e.g. the BSE [4, 15, 34], the Salpeter equation [58], perturbative QCD on the light-cone [48], the QP model of Ref. [36], and of course the Dirac hydrogen atom. The extent to which these singularities actually appear in expressions for physical probabilities is influenced by the way in which they are renormalized. In the light-cone calculations of Ref. [48] the divergence is ascribed to self-energy corrections of the one-body quark propagator; this has as consequence that the meson wave function must be renormalized at small distances and that the divergence has only small physical effect. A different view is given by Ito [41], who connects the divergence and renormalization solely to the quark-antiquark annihilation vertex. Consequently the divergence remains visible in other reactions such as in a large momentum tail in the pion electromagnetic form factor. This form factor is studied in Section 4.3 and shown in Fig. 4.2. The asymptotic effect is also seen in the full BSE analyses of the pion form factor in Refs. [15, 30]. Section 4.4 discusses the renormalization method of Ito and shows how it can be applied to the QP wave functions in configuration space.

In Chapter 2 we give an overview of properties of the two QP equations and their solutions. Apart from their derivation, partial wave projection and behavior for large coupling constants, attention is also paid to the dependence on the gauge of the vector interaction and to the linear Regge-trajectory behavior. The Chapter concludes with a fit to the complete meson mass spectrum which is listed in Table 2.3. This fit determines the parameter set in Table 2.2 that is used in the investigations of the following Chapters. For pure scalar confinement we find that the slope of the Regge-trajectories of the light mesons is much smaller in the QP models than in the nonrelativistic models. Stated differently, we find that the rotationally excited light QP mesons have much lower mass than their nonrelativistic counterparts. The Regge-slopes are greatly increased and almost doubled if a small amount of vector confinement is added (Klein's paradox admits only a small amount of vector confinement). With this vector admixture the experimental Regge-slopes are reproduced in the QP model at a confinement strength $\kappa \simeq 0.33 \text{ GeV}^2$. This is much more than the strength $\kappa \simeq 0.18 \text{ GeV}^2$ deduced from nonrelativistic potential models. This casts doubt on the reliability of the nonrelativistic value. Although this strong confinement gives good light meson masses, it does make it difficult to get a perfect fit for the heavy mesons. This may indicate that the confinement strength depends on the quark flavor.

Chapter 3 further investigates the differences between the nonrelativistic and

the QP meson mass spectra. We separate the effects due to the inclusion of the negative energy states from other effects. This is done by comparing the spectra of the nonrelativistic and relativized Schrödinger equations with those of the full QP model and those of the QP model with some or all negative energy states omitted. All equations are again solved in configuration space. Figures 3.1 – 3.4 show the spectra. The Figures show that most relativistic ingredients have big influence on the mass spectra and thus are important for determining the parameters of the $q\bar{q}$ interaction, especially the confinement strength κ . Yet the global structure of the spectrum —level ordering, relative sizes of splittings— remains rather untouched under the relativistic modifications. This confirms the conclusion drawn from the success of nonrelativistic quark models that most relativistic effects in $q\bar{q}$ spectroscopy can be mimicked by employing nonrelativistic dynamics together with effective parameters.

The Chapter also discusses the origin of the relativistic differences. The wave function restricted to positive energy states only consists mainly of upper spinor components, but because of the large quark momenta a considerable amount of the lower spinor components is mixed in as well. We note that the scalar confining potential is attractive for upper spinor components and repulsive for lower spinor components. The net result of the attraction and repulsion in the upper and lower parts of the positive energy states is that a large part of the confining strength cancels and that its confining effect is considerably reduced as compared to the nonrelativistic result. This phenomenon is mainly responsible for the great difference between the nonrelativistic mass spectrum and the relativistic QP mass spectrum. It explains why more confinement strength is needed in the QP model than in the Schrödinger model. Furthermore, it also explains why a small amount of vector confinement has such a great influence. The vector confinement is attractive for both the upper and lower components, so no cancellation takes place and the full strength of the vector confinement is felt by the QP wave.

The QP meson masses are slightly increased if the wave components consisting of one positive and one negative energy state are included. The admixture of the double negative energy states is small and their effect on the meson masses may be neglected for most mesons. However, their inclusion in the Salpeter and ET equations lowers the spin-singlet meson masses that much that they spoil the fair description of the mass spectrum found without them (cf. Fig. 3.3). This is caused by the overestimate of the propagation of the double negative states in these models. It is pointed out in Ref. [73] that the excessive propagation of the double negative energy states in the ET model can be reduced by employing the proper retardation in the matrix elements of the potential that connect to these states. This requires an extension of the static confining potential to retarded times, for which no unambiguous prescription exists. It may be remarked that the introduction of retarded times in the potential leads to extra nonlocalities in the QP equations which are probably too complicated to handle in the configuration space approach.

Chapter 4 analyzes some electromagnetic and electroweak meson interactions within the relativistic QP framework. Section 4.1 discusses the construction of the two-body current in the QP model. Section 4.2 investigates radiative decays of mesons; Table 4.4 gives an overview of the QP decay probabilities. For the heavy mesons they are often larger than other authors report [19, 29]. The comparison in Table 4.1 indicates which relativistic ingredients are important. The Table shows that a big relativistic contribution is given by the full projection of the decay operator on the positive energy components. We also note that it is important to account for all momentum dependencies in the Hamiltonian if one translates the momentum dipole moment to a configuration dipole moment by means of the commutator of the Hamiltonian with the position operator [as in Eq. (4.2.34)]. It is interesting to note that these two main relativistic contributions to the decay probability are also the main relativistic contributions to the meson mass spectrum, and that their effect on the decay vertex corresponds to their effect on the meson masses in such a way that they roughly compensate each other in the final decay probability. This shows the importance of treating the interactions consistently with the dynamics.

The contents of the last two Sections were already briefly mentioned. Section 4.3 discusses electromagnetic meson form factors and concentrates on the effect of the divergence of the wave function at the origin on the pion form factor, which is plotted in Fig. 4.2. It leads to a large tail in the form factor at high momenta. The divergence of the wave function at short distances and its renormalization are considered in detail in Section 4.4. We discuss the annihilation vertex renormalization scheme of Ito [41] and apply it to the pion wave function in configuration space. This illustrates how divergent loops can be regularized numerically in configuration space. The Section concludes with a comparison of the relativistic effects on the pseudoscalar decay constants, shown in Fig. 4.6, and with an overview of the annihilation probabilities of pseudoscalar and vector mesons, listed in Tables 4.7 and 4.8. Again we notice a correspondence between the importance and effects of relativistic ingredients on the meson annihilation vertex and meson masses, which tend to cancel in the final decay probability.

In summary, this thesis analyzes extensions of the nonrelativistic constituent quark potential model to relativistic forms which incorporate the full covariant Dirac structure of the quark and antiquark. All momentum dependent functions which appear in the relativistic equations are Fourier transformed to configuration space in order to avoid difficulties associated with the long-distance behavior of the confining potential. We present the first systematic analysis of the mass spectra of the light, mixed and heavy mesons which includes the full spinor structure. We observe that the introduction of the negative energy states can lead to problems in the two-quark system which are similar to those caused by Klein's paradox in the one-body Dirac equation. We find that the main differences with the nonrelativistic approach are related to the projection on the quark's Dirac spinor structure of the potential and of

the meson decay vertices. In the projection of the potential a large part of the scalar confinement is cancelled between the upper and lower spinor components, creating a major role for the vector confinement part. The reduction of the effect of the scalar confinement causes that, in order to obtain fair light meson masses, one needs a confinement strength in the relativistic model that is almost doubled as compared to the nonrelativistic model. The projection on the quark Dirac spinors of the meson decay vertices yields reductions of probabilities for processes such as radiative decay and annihilation decay. Compared to the effect of this projection, the negative energy states of the quark spinors have only rather moderate influence. Nevertheless they can account for up to 0.1 GeV of the binding of excited charmonium states and they may alter charmonium decay widths by up to 25%. Remarkably, the changes in the meson masses and decay vertices induced by the various relativistic ingredients tend to compensate each other in the final expression for the decay rates.

We conclude that a relativistic analysis is necessary for fixing absolute values of parameters in the constituent quark model, especially for determining the confinement strength and some decay probabilities. The relative values of the meson masses and of the meson decay probabilities are rather insensitive to the neglect of relativistic features. This reinforces the reliability of nonrelativistic calculations of these relative values.

Chapter 2

Meson mass spectrum

A method is described for solving relativistic quasipotential equations in configuration space. The Blankenbecler-Sugar-Logunov-Tavkhelidze and an equal-time equation, both relativistic covariant two-body equations containing the full Dirac structure of positive and negative energy states, are studied in detail. These equations are solved for a system of two constituent quarks interacting through a potential consisting of a one-gluon-exchange part with running coupling constant plus a linear confining potential which is mostly scalar and partly vector, and the spectrum of all light and heavy mesons is calculated. This Chapter is a slightly extended version of Ref. [70].

2.1 Introduction

It is rather surprising how well the nonrelativistic constituent quark model does describe the masses of the known mesons and baryons [29]. However, nonrelativistic models with or without relativistic corrections can be criticized easily of treating the quark dynamics inaccurately when high momentum processes or light quarks are considered. It is therefore interesting to study relativistic covariant extensions of the constituent quark model, which are still likely to reproduce the hadron spectroscopy with similar agreement as the older models, but with a more reliable dynamical framework at extreme momenta.

In this Chapter we investigate two different relativistic covariant approximations to the Bethe-Salpeter equation, namely the equal-time approximation [56, 73, 74] and the Blankenbecler-Sugar-Logunov-Tavkhelidze approximation [9, 17] and calculate the meson mass spectrum. The ingredients of the calculations are constituent quarks interacting through a instantaneous flavor-independent phenomenological quark-antiquark potential. The potential consists of a Coulomb-like one-gluon-exchange part with running coupling constant and of a linear plus constant confining part which is a mixture of scalar and vector character. For the vector part of the potential two different gauges, Feynman and Coulomb, are examined.

The Bethe-Salpeter equation (BSE) is the relativistic covariant generalization of the Lippmann-Schwinger equation for a two-quark bound state and can be written as

$$S^{-1}(P, p)\psi(P, p) = - \int \frac{d^4 p'}{i(2\pi)^4} V(P, p - p') \psi(P, p'), \quad (2.1.1)$$

where P and p are the total and relative momenta. Two new features are introduced as compared to the nonrelativistic equation. The first one is that the bound state wave function $\psi(P, p)$ and the potential $V(P, p - p')$ now also depend on the fourth component of the relative momentum. The second is that for each quark the number of degrees of freedom is doubled due to the introduction of the negative energy states. These extensions make the numerical work necessary for solving the BSE highly non trivial. In order to reduce the complexity one may remove all or some of the negative energy states, or one may eliminate the dependence on the fourth component of the relative momentum. The Lorentz invariance and the structure of the negative energy states can be kept if this component is eliminated.

There have been various suggestions how to approximate the relative energy dependence of the BSE [10], most of which are based on a prescription for modifying the two-body propagator in such a way that the relative energy is forced to some fixed value. This modification of the propagator is equivalent to a modification of the potential and the resulting wave equations are commonly called quasipotential equations. Here we study two of them. The first one is the Blankenbecler-Sugar-Logunov-Tavkhelidze (BSLT) approximation, originally proposed by Logunov and Tavkhelidze, and Blankenbecler and Sugar [9], and extended to unequal masses by Cooper and Jennings [17]. The second is a two-body Dirac equation due to Wallace and Mandelzweig [56, 73, 74], which may be viewed as an extension of the equal-time approximation of Salpeter [65]. These quasipotential equations are normally formulated in momentum space because many expressions in the equations depend on functions like $\sqrt{p_i^2 + m_i^2}$. However, the confining potential in momentum space is highly singular at zero relative momentum q . From $V(q = 0) = \int dx^3 V(x)$ and the monotonic increase of the confining potential $V(x)$ one finds that $V(q)$ diverges stronger than q^{-3} for small momenta. Special care must be given when solving such equations [32, 37, 38, 58, 59, 72]. This work uses a different approach. Using well-chosen representations of the quasipotential equations, we found that they can be Fourier transformed easily to configuration space, thus encompassing all problems associated with the confining potential.

This Chapter is organized as follows. In the next Section we discuss the derivation of the BSLT and ET equations and how they can be Fourier transformed from momentum space to configuration space. The partial wave projection of the equations is given in Appendix 2.A. In Section 2.3 we describe the interaction and its implications for the short distance behavior of the corresponding solutions. The

presence of the Coulomb-like potential makes the wave function singular at zero relative distance. This sets an upper bound for fixed coupling constants. The short distance behavior of the $J^P = 0^-$ states (e.g. the pion) is analyzed in detail in Appendix 2.B. In Section 2.4 we describe the method of solution of the resulting integro-differential equations. Also we study the parameter dependence and global behavior of relativistic effects in the meson mass spectrum. Section 2.5 discusses the Regge-trajectories which follow from the mass spectra of the BSLT and ET equations. The slopes of these trajectories are found to be dependent on the degree of admixture of vector character in the confining potential. If it becomes too large the potential becomes repulsive at long distances in some channels, making the solutions of the wave equation unbound. This gives an upper bound for the degree of the vector character in the confining potential. In Section 2.6 the full meson spectrum as obtained from the various quasipotential equations is discussed, and in the final Section some concluding remarks are made.

2.2 The quasipotential equations

For the full BSE it is of no importance how the total and relative momenta are defined. However, the prescriptions for the quasipotential approximation depend on the definition of the relative momentum. Let us follow Wightman and Garding [55] and define the total and relative momenta P and p for a two-particle system by

$$\begin{aligned} P &= p_1 + p_2, & p_1 &= \alpha(s)P + p, \\ p &= \beta(s)p_1 - \alpha(s)p_2, & p_2 &= \beta(s)P - p, \end{aligned} \quad (2.2.2)$$

and

$$\alpha(s) = \frac{s + m_1^2 - m_2^2}{2s}, \quad \beta(s) = \frac{s - m_1^2 + m_2^2}{2s}, \quad (2.2.3)$$

where $s = -P^2 = P_0^2 - \mathbf{P}^2$, and p_1 and p_2 denote the momenta of the two particles. In the center of mass system, where $P = (M, \mathbf{0})$, they read

$$p_1 = \left(\frac{M^2 + m_1^2 - m_2^2}{2M} + p_0, \mathbf{p} \right) = (E_1 + p_0, \mathbf{p}), \quad (2.2.4)$$

$$p_2 = \left(\frac{M^2 - m_1^2 + m_2^2}{2M} - p_0, -\mathbf{p} \right) = (E_2 - p_0, -\mathbf{p}). \quad (2.2.5)$$

This definition of p has the advantage that in the limit of one infinitely heavy particle, say $m_2 \rightarrow \infty$, that $E_1 \rightarrow M - m_2$. Now $M - m_2$ is precisely the total energy associated with the light particle, so this implies that the relative energy p_0 goes to zero. It turns out that this last property is essential to give quasipotential approximations which have the correct one-body limit, i.e., which reduce the one-body Dirac equation in the limit of one infinitely heavy particle.

2.2.1 Blankenbecler-Sugar-Logunov-Tavkhelidze equation

The propagator of the Bethe-Salpeter equation is

$$\begin{aligned} S(p_1, p_2) &= (\not{p}_1 - m_1)^{-1} (\not{p}_2 - m_2)^{-1} \\ &= (\not{p}_1 + m_1) (\not{p}_2 + m_2) S^{\text{scalar}}(p_1, p_2). \end{aligned} \quad (2.2.6)$$

The pole structure of this propagator is contained in the scalar part of the propagator $S^{\text{scalar}}(p_1, p_2)$. In the approximation first proposed by Logunov and Tavkhelidze, and Blankenbecler and Sugar [9], it is assumed that the pole structure of the scalar part may be approximated by means of a dispersion relation according to

$$\begin{aligned} S^{\text{scalar}} \rightarrow S_{\text{BSLT}}^{\text{scalar}} &= 2\pi i \int_{(m_1+m_2)^2}^{\infty} ds' \frac{f(s', s)}{s' - s} \delta^+([\alpha(s')P' + p]^2 + m_1^2) \\ &\quad \times \delta^+([\beta(s')P' - p]^2 + m_2^2), \end{aligned} \quad (2.2.7)$$

where $P' = \sqrt{s'/s}P$, and $f(s', s)$ is any function that satisfies $f(s, s) = 1$. Performing the integral gives in the center of mass (cm) system

$$S_{\text{BSLT}}^{\text{scalar}} = \frac{f((\omega_1 + \omega_2)^2, s)}{(\omega_1 + \omega_2)^2 - s} \frac{\omega_1 + \omega_2}{2\omega_1\omega_2} \delta(p_0), \quad (2.2.8)$$

with $\omega_i = \sqrt{\mathbf{p}^2 + m_i^2}$. Taking for $f(s', s)$ the simple form proposed by Cooper and Jennings [17], which yields the proper one-body limit in the case that one of the masses goes to infinity, one finds

$$S_{\text{BSLT}}^{\text{scalar}} = -\frac{1}{s - (\omega_1 + \omega_2)^2} \frac{1}{s - (\omega_1 - \omega_2)^2} \frac{2s}{\omega_1 + \omega_2} \delta(p_0), \quad (2.2.9)$$

and

$$S_{\text{BSLT}}(P, p) = (\not{p}_1 + m_1) (\not{p}_2 + m_2) S_{\text{BSLT}}^{\text{scalar}}(P, p). \quad (2.2.10)$$

The \tilde{p}_1 and \tilde{p}_2 follow from p_1 and p_2 by putting the relative energy to zero, thus $\tilde{p}_1 = (E_1, \mathbf{p})$ and $\tilde{p}_2 = (E_2, -\mathbf{p})$. This propagator may be cast in several forms. Note that the numerator of the BSLT propagator is proportional to

$$\begin{aligned} [s - (\omega_1 + \omega_2)^2][s - (\omega_1 - \omega_2)^2]/4s &= \\ &= [(s + \omega_1^2 - \omega_2^2)^2 - 4s\omega_1^2]/4s = (E_1^2 - \omega_1^2) = \tilde{p}_1^2 - m_1^2 \end{aligned} \quad (2.2.11)$$

$$= [(s + \omega_2^2 - \omega_1^2)^2 - 4s\omega_2^2]/4s = (E_2^2 - \omega_2^2) = \tilde{p}_2^2 - m_2^2. \quad (2.2.12)$$

Therefore one can also write

$$S_{\text{BSLT}} = -\frac{\delta(p_0)}{2(\omega_1 + \omega_2)} \frac{4s(\not{p}_1 + m_1)(\not{p}_2 + m_2)}{[s - (\omega_1 + \omega_2)^2][s - (\omega_1 - \omega_2)^2]} \quad (2.2.13)$$

$$= \frac{\delta(p_0)}{2(\omega_1 + \omega_2)} \frac{\not{p}_1 + m_1}{\not{p}_2 - m_2} \quad (2.2.14)$$

$$= \frac{\delta(p_0)}{2(\omega_1 + \omega_2)} \frac{\not{p}_2 + m_2}{\not{p}_1 - m_1}. \quad (2.2.15)$$

It is instructive to project the BSLT propagator upon positive and negative energy states. We take

$$\Lambda_i^{\rho_i}(\mathbf{p}_i) = \frac{\rho_i(\boldsymbol{\gamma}^{(i)} \cdot \mathbf{p}_i + m_i) + \omega_i \gamma_0^{(i)}}{2\omega_i} \quad (2.2.16)$$

and $\bar{\Lambda}_i^\rho(\mathbf{p}_i) = \Lambda_i^\rho(-\mathbf{p}_i)$ which satisfy

$$\left[c_+ \Lambda_i^+(\mathbf{p}_i) + c_- \Lambda_i^-(\mathbf{p}_i) \right]^{-1} = c_+^{-1} \bar{\Lambda}_i^+(\mathbf{p}_i) + c_-^{-1} \bar{\Lambda}_i^-(\mathbf{p}_i). \quad (2.2.17)$$

Introducing $\bar{\Lambda}^{\rho_1 \rho_2} = \bar{\Lambda}_1^{\rho_1}(\mathbf{p}) \bar{\Lambda}_2^{\rho_2}(-\mathbf{p})$ and using

$$\not{p}_i + m_i = (\omega_i + p_{0i} - i\varepsilon) \bar{\Lambda}_i^+(\mathbf{p}_i) - (\omega_i - p_{0i} - i\varepsilon) \bar{\Lambda}_i^-(\mathbf{p}_i), \quad (2.2.18)$$

gives

$$S_{\text{BSLT}} = \frac{\delta(p_0)}{2(\omega_1 + \omega_2)} \frac{1}{G} \left[(\omega_1 + E_1)(\omega_2 + E_2) \bar{\Lambda}^{++} - (\omega_1 + E_1)(\omega_2 - E_2) \bar{\Lambda}^{+-} \right. \\ \left. - (\omega_1 - E_1)(\omega_2 + E_2) \bar{\Lambda}^{-+} + (\omega_1 - E_1)(\omega_2 - E_2) \bar{\Lambda}^{--} \right], \quad (2.2.19)$$

where $G = \omega_1^2 - E_1^2 = \omega_2^2 - E_2^2$. This form clearly shows that the BSLT propagator is time-reversal invariant. It satisfies the condition that it does not change form if one interchanges simultaneously the energy labels $\rho_i \rightarrow -\rho_i$ and the particle energies $E_i \rightarrow -E_i$. If the potential is also time-reversal invariant, then the BSLT equation has the property that if a solution exists with mass M then there will also be a solution at $-M$, which is identical to the solution at M but with positive energy states changed to negative energy states and vice versa. These solutions at $-M$ correspond of course to the antiparticles of the solutions at M .

Since we want to solve the BSLT equation $S_{\text{BSLT}}^{-1}\psi = -V\psi$ in configuration space we have to Fourier transform it. In order to bring this equation in a form which may be easily transformed we multiply it by

$$D = \frac{\not{\mathbf{p}}_1 + \not{\mathbf{p}}_2 + m_1 + m_2}{2(\omega_1 + \omega_2)} \quad (2.2.20)$$

which, using Eqs. (2.2.14) and (2.2.15), gives

$$\begin{aligned} (\not{\mathbf{p}}_1 + \not{\mathbf{p}}_2 - m_1 - m_2)\psi(P, \mathbf{p}) &= \frac{1}{2(\omega_1 + \omega_2)}(\not{\mathbf{p}}_1 + \not{\mathbf{p}}_2 + m_1 + m_2) \\ &\times \int \frac{d\mathbf{p}'}{(2\pi)^3} V(\mathbf{p}' - \mathbf{p})\psi(P, \mathbf{p}'). \end{aligned} \quad (2.2.21)$$

In this form it is most clearly visible that in the limit that one of the particles masses goes to infinity, say $m_2 \rightarrow \infty$, the BSLT equation reduces to the Dirac equation

$$(\not{\mathbf{p}}_1 - m_1)\psi(\mathbf{p}_1) = \int \frac{d\mathbf{p}'_1}{(2\pi)^3} V(\mathbf{p}'_1 - \mathbf{p}_1)\psi(\mathbf{p}'_1). \quad (2.2.22)$$

The Fourier transform of the BSLT equation now reads

$$\begin{aligned} &\left[i\boldsymbol{\gamma}^{(1)} \cdot \boldsymbol{\nabla} + E_1\gamma_0^{(1)} - i\boldsymbol{\gamma}^{(2)} \cdot \boldsymbol{\nabla} + E_2\gamma_0^{(2)} - m_1 - m_2 \right] \psi(P, \mathbf{x}) = \\ &\int d\mathbf{x}' \frac{Z_{\text{BSLT}}(\mathbf{x}' - \mathbf{x})}{2(m_1 + m_2)} \\ &\times \left[i\boldsymbol{\gamma}^{(1)} \cdot \boldsymbol{\nabla} + E_1\gamma_0^{(1)} - i\boldsymbol{\gamma}^{(2)} \cdot \boldsymbol{\nabla} + E_2\gamma_0^{(2)} + m_1 + m_2 \right] V(\mathbf{x}')\psi(P, \mathbf{x}'). \end{aligned} \quad (2.2.23)$$

Due to the relativistic phase space factor in the BSLT propagator, a non-locality occurs in the relativistic equation, which is contained in the function

$$Z_{\text{BSLT}}(\mathbf{R}) = \int \frac{d\mathbf{p}}{(2\pi)^3} \frac{m_1 + m_2}{\omega_1 + \omega_2} e^{i\mathbf{p} \cdot \mathbf{R}}. \quad (2.2.24)$$

This integral can be found by rewriting

$$\frac{m_1 + m_2}{\omega_1 + \omega_2} = \frac{1}{m_1 - m_2} \left[(m_1^2 - \boldsymbol{\nabla}_R^2) \frac{1}{\omega_1} - (m_2^2 - \boldsymbol{\nabla}_R^2) \frac{1}{\omega_2} \right], \quad (2.2.25)$$

and using the Fourier transform of m_i/ω_i ,

$$Z_i(\mathbf{R}) = \int \frac{d\mathbf{p}}{(2\pi)^3} e^{i\mathbf{p} \cdot \mathbf{R}} \frac{m_i}{\omega_i} = \frac{m_i^2}{2\pi^2 R} K_1(m_i R). \quad (2.2.26)$$

K_1 is the modified Bessel function of the second kind of order one. A general formula for the Fourier transform of arbitrary powers of ω_i in arbitrary dimensions is given in Ref. [66]. The non-locality becomes

$$Z_{\text{BSLT}}(R) = \frac{1}{2\pi^2 R^2} \frac{1}{m_1 - m_2} \left[-m_1^2 K_2(m_1 R) + m_2^2 K_2(m_2 R) \right]. \quad (2.2.27)$$

which is invariant under the interchange $m_1 \leftrightarrow m_2$. Both $Z_{\text{BSLT}}(R)$ and $Z_i(R)$ behave like $1/R^2$ for short distances. If the two quarks have equal masses then the non-localities become identical, $Z_{\text{BSLT}}(R) = Z_1(R) = Z_2(R)$. In order to be solved, the BSLT equation is projected on eight basis states with definite spin and orbital momentum. These basis states, the partial wave analysis and the resulting eight coupled integro-differential equations are discussed in Appendix 2.A.1. As example, the reader may look at Eq. (2.B.73) to see the explicit BSLT equation for the pion.

2.2.2 Equal-time approximation

In the equal-time (ET) approximation the assumption is made that the $q\bar{q}$ -potential V does not depend on the relative energy in the cm system. This simplifies the BSE considerably. One may then introduce the equal-time wave function $\psi(\mathbf{p}) = 1/(2\pi i) \int dp_0 \psi(p_0, \mathbf{p})$, or $\psi(\mathbf{x}) = \psi(x_0 = 0, \mathbf{x})$, and integrate the BSE on both sides over p_0 to obtain an equation for the ET wave function:

$$\psi(\mathbf{p}) = - \left[\int \frac{dp_0}{2\pi i} S(p_1, p_2) \right] \int \frac{d\mathbf{p}'}{(2\pi)^3} V(\mathbf{p} - \mathbf{p}') \psi(\mathbf{p}'). \quad (2.2.28)$$

For the sake of clarity the derivations in this Section are formulated in the cm frame and therefore the ET approach does not show a manifestly relativistic covariant form. Yet it can be formulated in a fully manifestly relativistic covariant way, see Ref. [74].

The ET equation as it stands in Eq. (2.2.28) does not reduce to the Dirac equation if one of the particles masses becomes infinitely heavy and so it does not have the correct one-body limit. However, as has been pointed out by Wallace and Mandelzweig [74], the ET approximation can be improved considerably by adding a propagator S_{cross} to the integral between square brackets, which represents the propagation of the two particles within the crossed box diagram. With this extra term the ET propagator exhibits the one-body limit, and furthermore the contributions of the crossed diagrams are approximately taken into account. The propagator is now taken as

$$S_{\text{ET}} = \int \frac{dp_0}{2\pi i} [S(p_1, p_2) + S_{\text{cross}}(p_1, p_2)], \quad (2.2.29)$$

where in the cm system

$$S_{\text{cross}}(p_1, p_2) = S(p_1, p_2^{\text{cross}}), \quad p_2^{\text{cross}} = (E_2 + p_0, -\mathbf{p}). \quad (2.2.30)$$

The only difference between p_2 and p_2^{cross} is the sign in front of the relative energy. The origin of the different signs for p_0 can easily be understood from the different directions of flow of relative energy in the uncrossed and crossed diagrams. A detailed justification for this crossed box contribution based on the eikonal approximation has been given in Ref. [74]. The integral over p_0 can be evaluated easily by using Eq. (2.2.18) and expressing the propagators in positive and negative energy projections. This gives

$$S_{\text{ET}} = \frac{\bar{\Lambda}^{++}}{\omega_1 + \omega_2 - E_1 - E_2} - \frac{\bar{\Lambda}^{-+}}{\omega_1 + \omega_2 + E_1 - E_2} - \frac{\bar{\Lambda}^{+-}}{\omega_1 + \omega_2 - E_1 + E_2} + \frac{\bar{\Lambda}^{--}}{\omega_1 + \omega_2 + E_1 + E_2}. \quad (2.2.31)$$

The terms containing $\bar{\Lambda}^{++}$ and $\bar{\Lambda}^{--}$ are well-known and stem from the p_0 integration over S . They were first used by Salpeter [65]. The other two terms result from the p_0 integration over S_{cross} . This form shows that the ET propagator is time-reversal invariant, similar to the BSLT propagator. The most important difference between the BSLT and ET approximation is the degree to which the propagation of negative energy states is suppressed as compared to the propagation of the positive energy states. For particles of equal mass ($\omega_1 = \omega_2 = \omega$, and $E_1 = E_2 = E$), the ratio of the propagation for positive and negative states is for the ET case

$$\frac{S_{\text{ET}}^{++}}{S_{\text{ET}}^{--}} = \frac{\omega + E}{\omega - E}, \quad (2.2.32)$$

whereas Eq. (2.2.19) gives for the BSLT case

$$\frac{S_{\text{BSLT}}^{++}}{S_{\text{BSLT}}^{--}} = \left(\frac{\omega + E}{\omega - E} \right)^2. \quad (2.2.33)$$

Therefore we can expect a larger admixture of negative states in the ET solutions than in the BSLT solutions. Note that this ratio is always positive for the BSLT propagator whereas it can be negative for the ET propagator. For the full BSE it is always positive at $p_0 = 0$.

Writing out the projection operators $\Lambda^{\rho_1 \rho_2}$ gives

$$S_{\text{ET}}^{-1} = \frac{1}{\omega_1} \left[-\boldsymbol{\gamma}^{(1)} \cdot \mathbf{p} + m_1 \right] \left[\boldsymbol{\gamma}^{(2)} \cdot \mathbf{p} - \gamma_0^{(2)} E_2 + m_2 \right] + \frac{1}{\omega_2} \left[-\boldsymbol{\gamma}^{(1)} \cdot \mathbf{p} - \gamma_0^{(1)} E_1 + m_1 \right] \left[\boldsymbol{\gamma}^{(2)} \cdot \mathbf{p} + m_2 \right]. \quad (2.2.34)$$

The EI bound state wave equation $S_{\mathbb{F}\Gamma}^{-1}\psi = -V\psi$ may now be transformed easily to configuration space and becomes

$$\int d\mathbf{x}' \left[\frac{Z_1(\mathbf{x} - \mathbf{x}')}{m_1} \mathcal{S}_1(\mathbf{x}') + \frac{Z_2(\mathbf{x} - \mathbf{x}')}{m_2} \mathcal{S}_2(\mathbf{x}') \right] \psi(\mathbf{x}') = -V(\mathbf{x})\psi(\mathbf{x}), \quad (2.2.35)$$

with

$$\mathcal{S}_1(\mathbf{x}) = \left[i\boldsymbol{\gamma}^{(1)} \cdot \boldsymbol{\nabla} + m_1 \right] \left[-i\boldsymbol{\gamma}^{(2)} \cdot \boldsymbol{\nabla} - \gamma_0^{(2)} E_2 + m_2 \right], \quad (2.2.36)$$

$$\mathcal{S}_2(\mathbf{x}) = \left[i\boldsymbol{\gamma}^{(1)} \cdot \boldsymbol{\nabla} - \gamma_0^{(1)} E_1 + m_1 \right] \left[-i\boldsymbol{\gamma}^{(2)} \cdot \boldsymbol{\nabla} + m_2 \right], \quad (2.2.37)$$

and the non-localities Z_i have already been given in Eq. (2.2.26). The ET equation can be solved after projecting it on basis states with definite spin and orbital momentum. The resulting eight coupled integro-differential equations can be found in Appendix 2.A.2.

2.3 The interaction

It is widely accepted that the interaction between the two quarks consists of a short-range part describing the one-gluon-exchange (OGE) potential and a infinitely rising long-range part responsible for the confinement of the quarks [52]. We use

$$V(x) = -\frac{\alpha(x)}{x} \boldsymbol{\gamma}_\mu^{(1)} \boldsymbol{\gamma}^{\mu(2)} + (\kappa x + c) \left[(1 - \varepsilon) 1^{(1)} 1^{(2)} + \varepsilon \boldsymbol{\gamma}_\mu^{(1)} \boldsymbol{\gamma}^{\mu(2)} \right]. \quad (2.3.38)$$

(The color factor $4/3$ of the expectation value of the OGE in the meson color wave function has been absorbed in the definition of α .) The OGE potential is a pure vector interaction. The confining potential is mainly scalar, so it must be taken color-independent in order to assure that it is attractive between quark pairs in baryons. Wilson loop techniques suggest that the confining potential should be taken purely scalar [31], but relativistic potential calculations have been published [18, 28, 47] which show a need for (some) vector confinement. Therefore, we choose a confining potential which is in principle scalar, but we do allow, when it turns out to be necessary, for a small fraction ε of vector confinement. Asymptotic freedom requires that for short distances the OGE coupling constant decreases logarithmically as $\alpha(x) \sim \alpha_0 / \ln(x_0/x)$ where $\alpha_0 = 8\pi/(33 - 2n_F)$ and $x_0 = e^{-\gamma}/\Lambda_{\text{QCD}}$ [52]. Richardson [64] has given an elegant prescription for a running coupling constant which for small distances reproduces the correct asymptotic freedom and which gives for large distances a linearly rising potential. We do not use this prescription since it can not specify the vector and scalar character of the potential. At large distances the

confining interaction dominates and the exact behavior of $\alpha(x)$ becomes of little importance. If one assumes that the coupling constant grows to some saturation value α_{sat} then a smooth interpolation between the short and long range is given by [49]

$$\alpha_I(x) = \alpha_0 \ln^{-1} \left[\frac{x_0}{x} \exp(-\mu x) + \exp\left(\frac{\alpha_0}{\alpha_{\text{sat}}}\right) \right]. \quad (2.3.39)$$

Here the typical range of the running coupling regime is controlled by the parameter μ ; the maximum range is found at $\mu = 0$. A longer range can be obtained by interpolating

$$\alpha_{II}(x) = \alpha_0 \left[\ln \left(\frac{x_0 + x}{x} \right) + \frac{\alpha_0}{\alpha_{\text{sat}}} \right]^{-1}. \quad (2.3.40)$$

We use $\Lambda_{\text{QCD}} = 0.2 \text{ GeV}$ and $n_F = 3$. The dependence on Λ_{QCD} and n_F , which is not large, can be compensated for by modifying μ and α_{sat} .

In the BSE the solutions are independent of the choice of gauge for the vector part of the potential. This independence depends essentially on the presence of crossed diagrams in the interaction kernel [24]. However, in the BSLT and ET approximations the relative energy is fixed, so crossed diagrams do not occur and the gauge-independence of these quasipotential equations must be broken. In order to estimate the gauge-dependence of our results we study two gauges. The first one is the Feynman gauge as used in Eq. (2.3.38). The other is the Coulomb, transverse or radiation gauge which is obtained by replacing

$$\gamma_\mu^{(1)} \gamma^{\mu(2)} \rightarrow \gamma_\mu^{(1)} \gamma^{\mu(2)} + \frac{1}{2} \left[\boldsymbol{\gamma}^{(1)} \cdot \boldsymbol{\gamma}^{(2)} - \frac{(\boldsymbol{\gamma}^{(1)} \cdot \boldsymbol{x})(\boldsymbol{\gamma}^{(2)} \cdot \boldsymbol{x})}{x^2} \right] \quad (2.3.41)$$

in Eq. (2.3.38). Appendix 2.A.3 gives the partial wave projections of these potentials.

The presence of the $1/x$ term in the potential has important consequences for the short distance behavior of the wave functions. This can be understood from the following simple picture. Consider the probability of the meson decaying through the annihilation of the quark and the antiquark. This process is proportional to the wave function at zero relative distance, or equivalently, to the wave function integrated over all relative momenta. Using the wave equation the integral over the wave function can be expressed as a $\int dp \psi(p) = - \int dp S(p) \int dq V(p-q) \psi(q)$, that is, a loop integral over the propagator S and potential V plus additional corrections. This is illustrated diagrammatically in Fig. 2.1. Let us focus on the ultra-violet (uv) behavior of the momentum integration over the triangle diagram. It is divergent for most dynamical models due to the OGE potential. For example, in the BSE the two-fermion propagator and the OGE interaction both fall off as p^{-2} for large p (we neglect for the moment the additional $\ln p^2$ behavior of the running coupling constant). So for large relative momenta the loop integral takes the uv divergent form

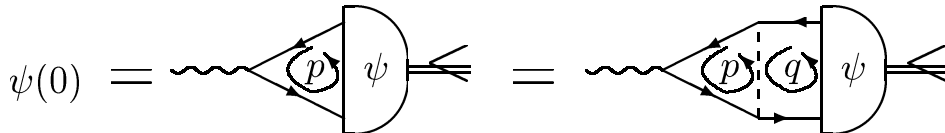


Figure 2.1: The meson wave function at zero relative distance written as a loop integral over the quark (quasi-) propagators and the potential, with additional corrections. If this loop integral is divergent, then the wave function is divergent at $x = 0$.

$\int d^4p p^{-4}$. Similarly, in the one-body Dirac equation and in the two-body quasipotential equations the propagators behave as p^{-1} and the potential as p^{-2} , what also leads to a uv divergent loop $\int d^3p p^{-3}$. Divergences also occur in the light-cone formalism where the propagator and potential go as p_{\perp}^{-2} and the two quark spinors as p_{\perp}^2 [48] resulting in $\int d^2p_{\perp} p_{\perp}^{-2}$. This suggests that the solutions of all these wave equations are singular at the origin. Indeed, at short distances the Dirac wave functions [57] and the Bethe-Salpeter wave functions [4, 34] behave like $\psi(x) \sim x^{\gamma}$, $-1 < \gamma < 0$, where γ is a decreasing function of the coupling constant α of the interaction. At some maximum value of α the exponent γ becomes smaller than -1 and physical acceptable solutions do no longer exist. These features are also shared by the BSLT and FT equations.

The extent to which these singularities actually appear in the physical wave functions is weakened, if the fixed coupling constant is replaced by a running coupling constant such that $\alpha(p) \sim \ln^{-1} p^2$ for $p \rightarrow \infty$. The triangle loop, however, is still uv divergent but the short distance behavior is like $\psi(x) \sim \ln^{\gamma} |x|$. Furthermore, the singular behavior can be removed by renormalizing the wave function by means of some cutoff scale. For example, this has been done in the light-cone calculations of Ref. [48]. Yet, the mathematical implications are important. Seemingly no attention has been given to the asymptotic behavior in most work on relativistic quark-quark dynamics such as in Refs. [42, 47]. In Appendix 2.B we analyze in detail the singular behavior of the wave functions of the $J^P = 0^-$ states (e.g. the pion) with a fixed coupling constant. In Section 4.3 we investigate the consequence of the singularity for the pion electromagnetic form factor. Section 4.4 discusses how the singularity can be regularized by a vertex renormalization.

2.4 Parameter dependence

In this Section we describe the calculational procedure to solve the quasipotential equations and we present some results on the parameter dependence of the spectrum of $J^{PC} = 0^{-+}$ states. For convenience we refer to these states as the 1S_0 states since their wave functions contain mostly 1S_0 components. Similarly, other J^{PC} states are also named by their main ${}^{2S+1}L_J$ components. Numerically stable solutions are obtained by taking explicitly into account the singularity in the bound state wave equation at $x = 0$ due to the presence of the OGE term. In Appendix B the behavior of the wave function of the 1S_0 state is analyzed in detail for small x . We find that the most singular component of it behaves as $\psi \sim x^\gamma$, $-1 < \gamma < 0$, and γ given by Eqs. (2.B.78), (2.B.84), (2.B.81) or (2.B.85). Let us introduce a function $f_\gamma(x)$ which for small arguments behaves as x^γ and for large arguments becomes unity. By substituting $\psi(x) = f_\gamma(x)\varphi(x)$ we get an equation for $\varphi(x)$ which is regular at $x = 0$. For the non 1S_0 states, no special precautions have to be taken, because the wave function for the coupling constant strengths considered in this work vanishes sufficiently fast in the origin. Numerically accurate solutions are found by using the same x^γ factor as for 1S_0 channel. The same holds when we have a running coupling constant, since the equations in this case are less singular than those with a fixed coupling constant.

The partial wave projection of the BSLT and EI equations leads to the coupled set of differential-integral equations (2.A.56) and (2.A.67) for n ($3 \leq n \leq 8$) components $\psi_i(x)$, which are expanded as $\psi_i(x) = f_\gamma(x) \sum_{j=1}^k c_{ij} S_j(x)$. The $S_j(x)$ are cubic Hermite spline functions (see e.g. Ref. [62]). The $\psi_i(x)$ are cut off at some maximum value x_{\max} and we impose $\psi_i(x_{\max}) = \psi'_i(x_{\max}) = 0$. Near $x = 0$ $\psi_i(x)$ is forced to be of order x^γ or higher. By evaluating Eqs. (2.A.56) or (2.A.67) at k fixed points x_1, \dots, x_k one obtains a set of $k \times n$ linear equations for the $k \times n$ spline coefficients c_{ij} , which only admits non-trivial solutions at the bound state energies. It should be noted that due to the multiplication of the BSLT equation by the operator D of Eq. (2.2.20) a continuum of additional solutions has been introduced in Eq. (2.2.21) for $M > m_1 + m_2$, which is not present in the original BSLT equation. The cutoff makes these continuum unphysical solutions into a discrete set, thus enabling to isolate and reject them. This is illustrated in Figs. 2.2(a) and (b) which show two 1S_0 solutions of the BSLT equation with $m = 0.2$ GeV, $\kappa = 0.2$ GeV², $\varepsilon = \alpha = c = 0$. The wave function shown in Fig. 2.2(a) is the ground state found at $M = 1.23$ GeV; the solution shown in Fig. 2.2(b) found at $M = 1.30$ GeV can easily be identified as an outgoing wave. As a result the latter solution should be rejected. The masses found for the physical bound states are insensitive to variations of x_{\max} , whereas the masses of the continuum solutions do depend on x_{\max} . Typical values that we used are $x_{\max} = 2$ fm and $k = 30$ for the heavy quark systems up to $x_{\max} = 5$ fm and $k = 120$ for the pion system. For the latter system a large number of splines is

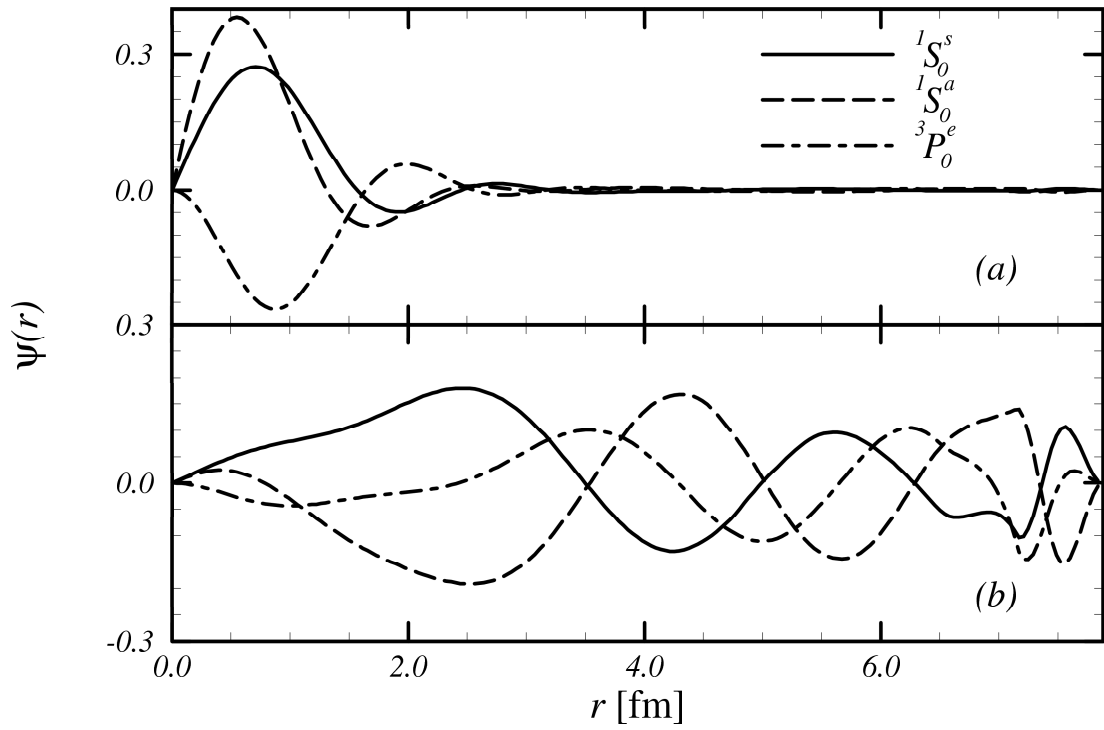


Figure 2.2: A physical bound state 1S_0 solution (a) at $M = 1.23$ GeV and an unphysical continuum 1S_0 solution (b) at $M = 1.30$ GeV obtained from the BSLT equation, with $m = 0.2$ GeV, $\kappa = 0.2$ GeV², $\alpha = c = \varepsilon = 0$.

needed to obtain good accuracy since its wave function can have a long oscillating tail. As an overall check on the method the configuration space program was also used to calculate the spectrum for a non-confining potential containing scalar and vector exchanges. The resulting masses were verified by solving the BSLT equation in momentum space [26]; agreement was found within 0.1%.

Let us now consider some important differences between the nonrelativistic and the relativistic equations. In the conventional nonrelativistic models as discussed for example in Ref. [29], the hyperfine interaction resulting from the OGE contribution is singular near the origin and as a result it has to be regularized by introducing a phenomenological cutoff. On the other hand, our relativistic equations are well defined, at least up to a critical coupling constant of the OGE interaction. In this case a natural cutoff essentially occurs due to relativity, where the scale is given by the mass of the constituent quarks. The singular behavior of the wave function at $x = 0$ induced by the Coulomb-like interaction in the relativistic equations considerably modifies the meson mass if the coupling constant α is close to its maximum value. Figure 2.3 shows the masses of a mostly nonrelativistic 1S_0 system ($m = 5$ GeV and $\kappa = 0.2$ GeV²) as a function of the coupling constant. For small α the spectrum agrees well with the Schrödinger result. However, if the limit $\alpha \rightarrow \alpha_{\max}$ is taken, the relativistic results differ considerably; $dM(\alpha)/d\alpha \rightarrow -\infty$ and $M(\alpha) \rightarrow M_0$, where generally M_0 is not equal to zero.

Furthermore, for the nonrelativistic Schrödinger-like equations an additional constant c in the potential causes only an overall shift in the meson mass spectrum. This does not happen in the relativistic case. Because the quasipotential equations are time-reversal invariant each solution for a meson at some positive mass is accompanied by its anti-meson solution at the same negative mass. If the constant c is added to the potential and we let c grow to negative values, the absolute masses of both solutions decrease until both mesons become massless. At this c the solutions coincide and for more negative c no bound state can be found except for higher excitations. This can clearly be seen from Fig. 2.4 where the 1S_0 spectrum is plotted as a function of c for the BSLT and FT equations.

The replacement of the nonrelativistic kinetic energy $p^2/2m$ by the relativistic expression $\sqrt{p^2 + m^2}$ and the introduction of the negative energy states greatly reduces the spacings between the ground state solution and the successive excitations for small quark masses. This feature is extensively discussed in Chapter 3. Figure 2.5 shows the calculated 1S_0 mass spectrum as a function of the quark mass with the confinement taken such that κ^2/m is fixed. This confinement gives constant binding energies for the Schrödinger equation. The figure illustrates nicely that for large masses the nonrelativistic results are obtained, whereas for small masses the level density becomes considerably higher.

Finally, another aspect which is absent in nonrelativistic models is the presence of solutions describing a heavy quark and a light quark-hole. Their presence is

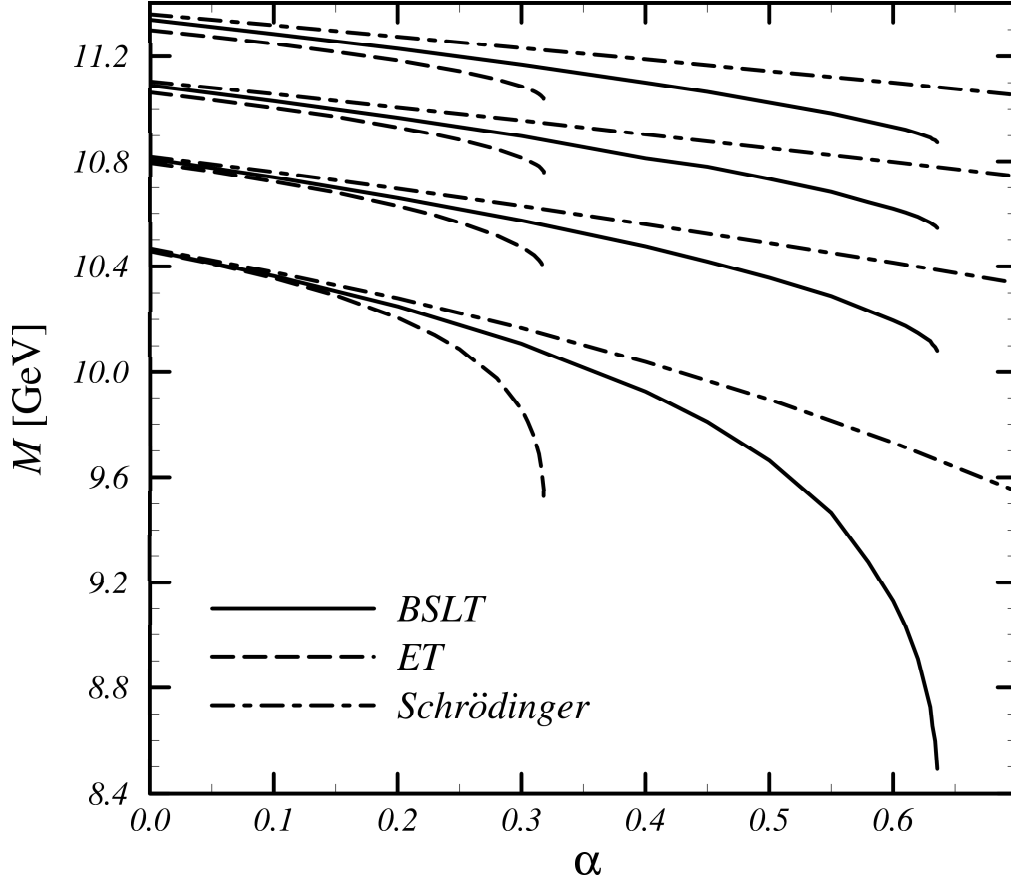


Figure 2.3: The masses of the ground state and the first few excitations of the 1S_0 systems are shown as a function of the fixed coupling constant α (calculated in the Feynman gauge with $m = 5$ GeV, $\kappa = 0.2$ GeV², $\varepsilon = c = 0$). The solid lines are for BSLT, broken lines for ET, and dotted lines for Schrödinger.

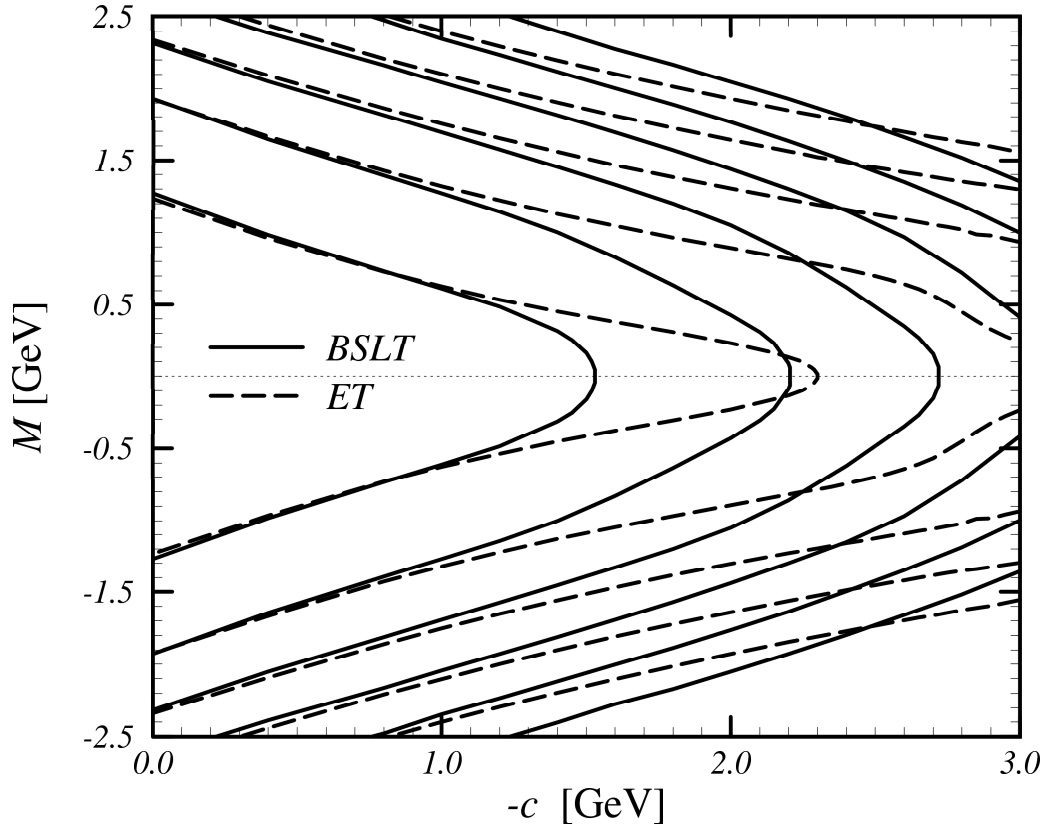


Figure 2.4: The masses of the ground state and the first few excitations of the 1S_0 system are shown as a function of the constant term c in the $q\bar{q}$ potential (calculated with $m = 0.2$ GeV, $\kappa = 0.2$ GeV², $\varepsilon = \alpha = 0$). States with negative mass represent anti-mesons. The solid lines are for BSLT, broken lines for ET.

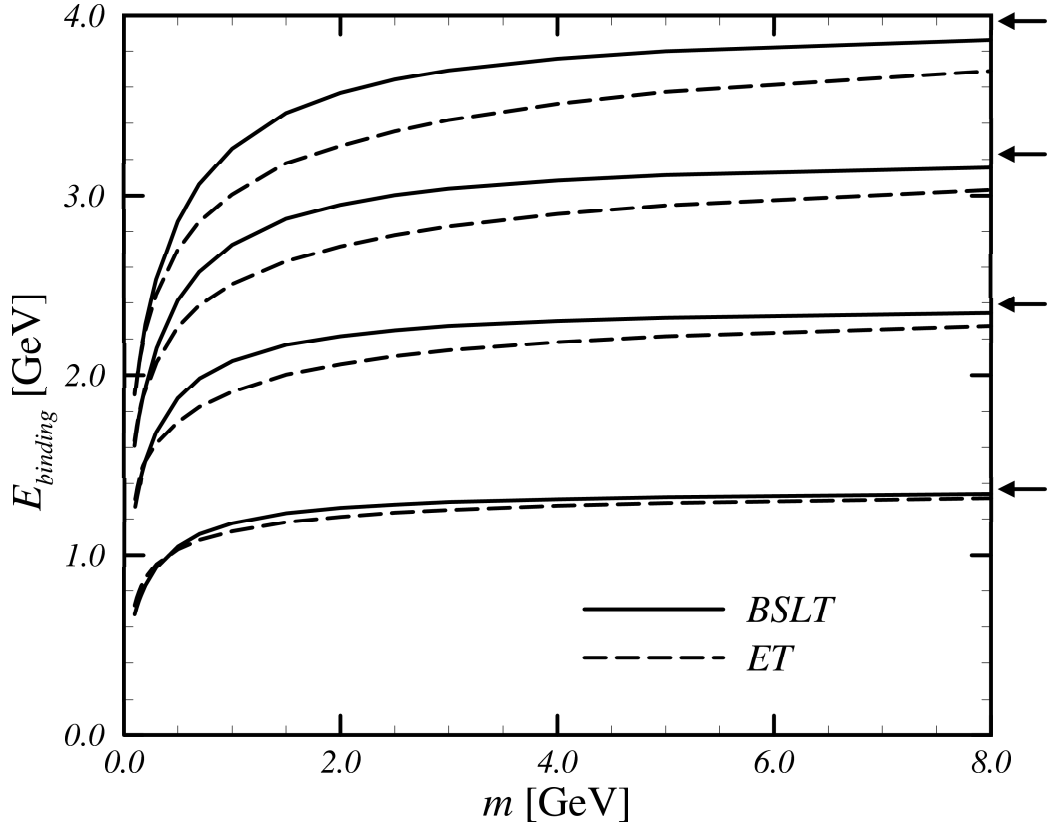


Figure 2.5: The masses of the ground state and the first few excitations of the 1S_0 systems are shown as a function of the quark mass (calculated with $c = \varepsilon = \alpha = 0$), but with the ratio $\kappa^2/m = 0.2 \text{ GeV}^3$ fixed. Under this condition the Schrödinger levels are independent of m ; they are indicated by the arrows on the right of the figure. The solid lines are for BSLT, broken lines for ET.

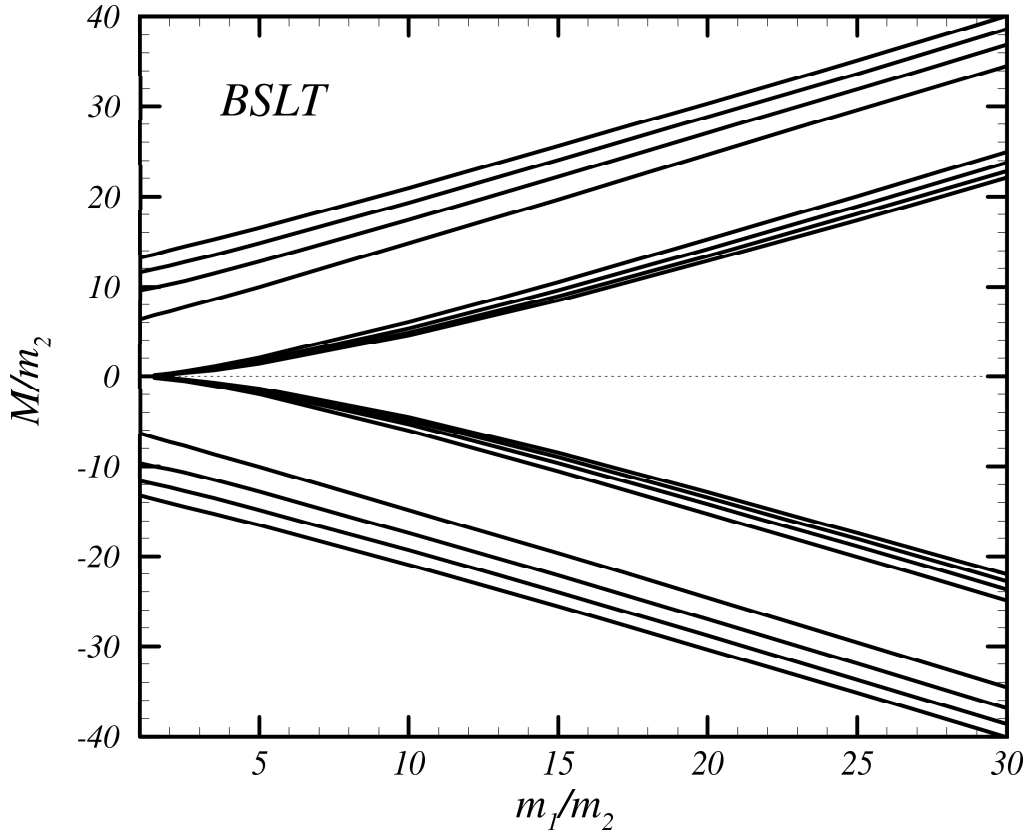


Figure 2.6: The masses of the ground state and the first few excitations of the 1S_0 systems in the BSLT equation are shown as a function of the mass m_1 of the first quark (calculated with $m_2 = 0.2$ GeV, $\kappa = 0.2$ GeV², $c = \varepsilon = \alpha = 0$).

a consequence of the requirement that the one-body Dirac equation is obtained in the limit that one particle becomes very heavy, and they can be interpreted in an analogous way as the negative energy states in the one-fermion Dirac hole theory. Figure 2.6 shows the 1S_0 mass spectrum for fixed mass of the second quark and various masses of the first quark. At equal masses the hole-quark states are not present, but as m_1 grows they emerge from the zero total mass axis, and at large m_1 two spectra symmetric around $M = \pm m_1$ are generated.

2.5 Confining force and Regge-trajectories

Experimentally it is found that the masses of the light mesons lie on a linear Regge-trajectory, that is, for large angular momenta J the squares of the masses M of the

Table 2.1: Slope β (in GeV^2) of the Regge-trajectories shown in Figs. 2.7 and 2.8. Listed values follow from a fit from $J = 2$ to $J = 6$.

	family	$\varepsilon = 0$	$\varepsilon = 0.15$ Feynman	$\varepsilon = 0.15$ Coulomb
BSLT	π	0.69	1.20	1.06
	ρ	0.69	1.13	1.01
	a_1	0.66	1.12	1.01
ET	π	0.67	0.47	0.64
	ρ	0.69	1.04	0.99
	a_1	0.65	0.92	0.83

mesons are proportional to their angular momenta

$$M^2 = \beta J + c, \quad (2.5.42)$$

where the Regge-slope $\beta \simeq 1.2 \text{ GeV}^2$ [52]. The value of the slope depends almost exclusively on the confinement strength and can be used to fix it. Figures 2.7 and 2.8 show the Regge behavior as obtained from the numerical solutions of the BSLT and ET equations using $m = 0.25 \text{ GeV}$, $\alpha = 0$, $c = -1.0 \text{ GeV}$ and a linear scalar confining potential with $\kappa = 0.33 \text{ GeV}^2$. The figures indeed show a linear relation between M^2 and J . However, the Regge-slope is considerably smaller than predicted by nonrelativistic models with energy operator $\sqrt{p^2 + m^2}$, where $\beta = 8\kappa$ [52]. These nonrelativistic models give a good description of the $c\bar{c}$ and $b\bar{b}$ systems when $\kappa \simeq 0.18 \text{ GeV}^2$ (see e.g. [29]). It turns out that a small admixture of vector confinement ε , as in Eq. (2.3.38), greatly affects the Regge-slopes. Figures 2.7 and 2.8 also show the Regge behavior for a fraction $\varepsilon = 0.15$ of vector confinement in the Feynman gauge and in the Coulomb gauge. All trajectories are increased except for the spin-singlet trajectory in the ET model in the Feynman gauge, which is decreased. Table 2.1 summarizes the resulting Regge-slopes.

A vector admixture in the confining interaction introduces a spin dependence through the presence of the $|-\ +\rangle$, $|+\ -\rangle$ and $|-\ -\rangle$ components. Because of this when too much vector confinement is chosen, $\varepsilon > 0.2$, some light mesons are no longer bound, i.e. certain channels may become deconfined. This effect can be interpreted as the two-body analog of Klein's paradox. It can be used to set an upper bound on the degree of allowed vector admixture. Reference [11] presents a similar analysis of this upper bound. Consider the strength of the confining potential in the $^1J_J^e$ channel in the Feynman gauge. From Eq. (2.A.69) we see that the projection of $\gamma_\mu^{(1)}\gamma^{\mu(2)}$ in

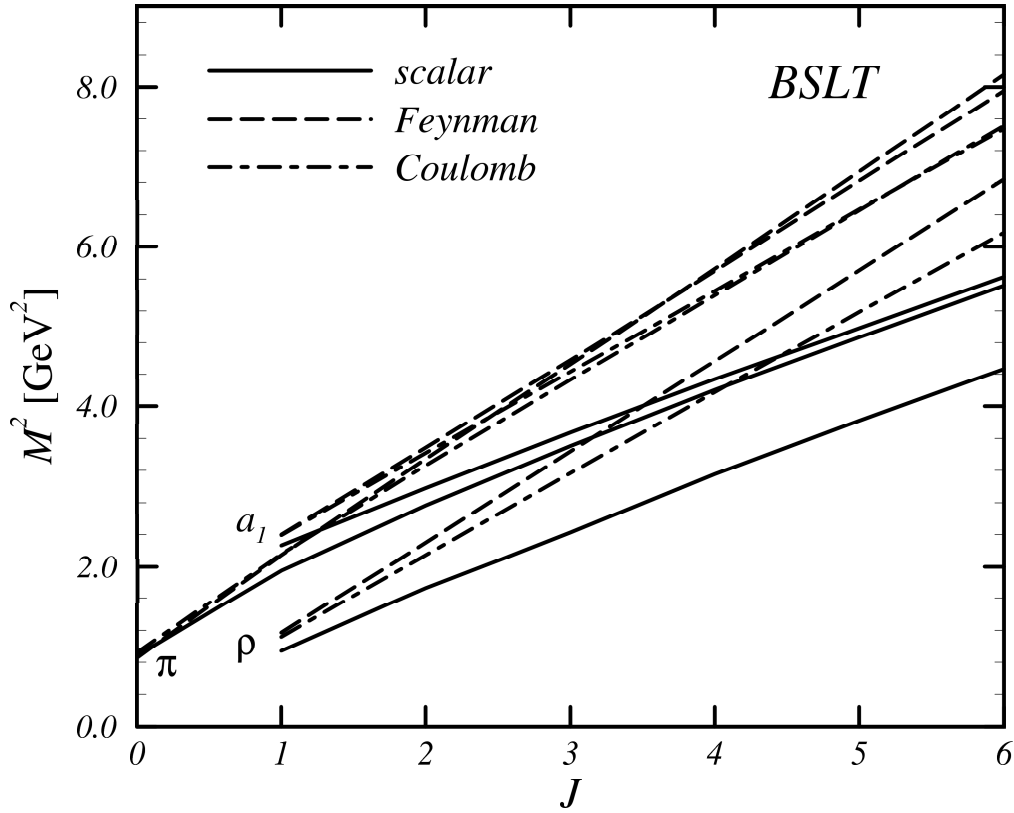


Figure 2.7: Regge-slopes in the BSLT model. The squared meson masses are plotted as a function of the total angular momentum J of the unexcited mesons (calculated with $m = 0.25$ GeV, $\alpha = 0$, $c = -1.0$ GeV and $\kappa = 0.33$ GeV²). Solid lines show the masses for a pure scalar confinement ($\varepsilon = 0$), broken lines for mixture of vector and mainly scalar confinement in the Feynman gauge ($\varepsilon = 0.15$), and dotted lines for the same mixture using the Coulomb gauge. The lines labeled π represent the π family [$P = (-)^{J+1}$ and $C = (-)^J$], and similarly for the ρ family [$P = C = (-)^{J+1}$] and the a_1 family [$P = C = (-)^J$]. The corresponding Regge-slopes are listed in Table 2.1.

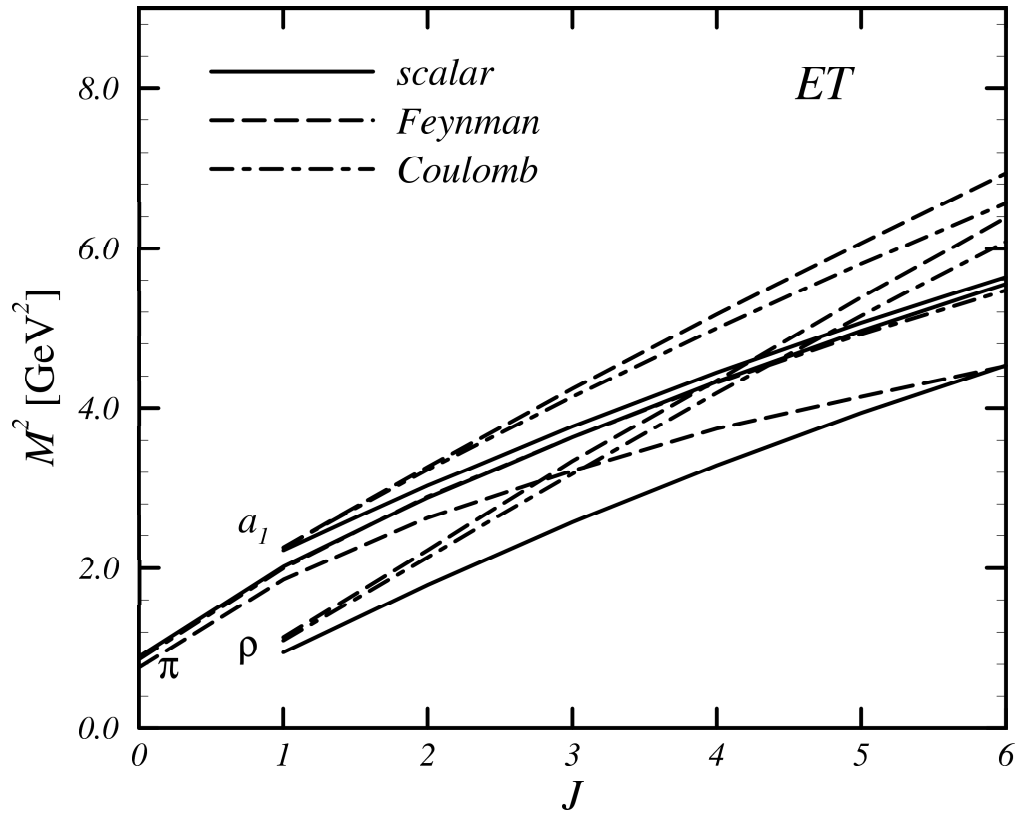


Figure 2.8: Identical to Fig. 2.7, but now for the ET equation.

this channel is -4 , so the linear part of the $q\bar{q}$ interaction in this channel is

$$\kappa x \left[(1 - \varepsilon) 1^{(1)} 1^{(2)} + \varepsilon \gamma_\mu^{(1)} \gamma^{\mu(2)} \right] \xrightarrow{1J_J^e} \kappa x \left[(1 - \varepsilon) - 4\varepsilon \right]. \quad (2.5.43)$$

Hence, if $\varepsilon > 0.2$ the potential becomes repulsive for large distances; the interaction tends to $-\infty$ for $x \rightarrow \infty$, which is clearly not physically allowed. This suggests that the $P = (-)^J$ mesons of the light quark system, of which the wave functions contain the $1J_J^e$ channel and have $|-\rangle$ components of size comparable to the $|+\rangle$ components, do not have a bound state solution if $\varepsilon > 0.2$. This is confirmed by the numerical solutions. In the Coulomb gauge a slightly larger value is allowed, namely $\varepsilon = 0.25$. In order to avoid these problems we demand that the admixture of the vector interaction in the confining potential does not reach or exceed these values.

It is interesting to note that also in the one-body Dirac equation, which can be used to describe a system of a very heavy and a light quark a similar problem arise. Such a framework has recently been used to study the spectrum of the D and B mesons [67]. A pure scalar confinement interaction was used. The repulsion exercised by the vector confinement on the negative components gives in this case also an upper limit on the allowed degree of vector admixture in the confining potential. Consider the Dirac equation

$$(m - i\cancel{\partial})\psi(\mathbf{x}) = -\kappa x[(1 - \varepsilon) + \varepsilon\gamma_0]\psi(\mathbf{x}). \quad (2.5.44)$$

Projection upon states of definite L gives

$$\begin{pmatrix} m - E & D_{J+3/2} \\ D_{-J+1/2} & m + E \end{pmatrix} \psi(x) = -\kappa x \begin{pmatrix} 1 & 0 \\ 0 & 1 - 2\varepsilon \end{pmatrix} \psi(x), \quad (2.5.45)$$

and D_ℓ as defined in Eq. (2.A.50). Eliminating the lower component of $\psi(x)$ in favor of the upper component of $\psi_1(x) = F(x)/x$ and letting $x \rightarrow \infty$ leads to

$$\left\{ \left[-\frac{\partial^2}{\partial x^2} + \frac{1}{x} \frac{\partial}{\partial x} + \frac{1}{x^2} (J - 3/2)(J + 1/2) \right] + (1 - 2\varepsilon)\kappa^2 x^2 \right\} F(x) = 0. \quad (2.5.46)$$

For $\varepsilon > 0.5$ the potential term becomes negative and the solutions for $F(x)$ are no longer bound.

2.6 Meson mass spectrum

Table 2.2 lists the parameters that we used to calculate the meson mass spectrum. We did not include the light isoscalar mesons (η , f , h). The masses of these mesons are expected to be modified by the process of $q\bar{q}$ annihilation and creation, making the transitions $u\bar{u} \leftrightarrow d\bar{d} \leftrightarrow s\bar{s}$ likely.

Table 2.2: Parameters for the BSLT and ET model (in units of GeV).

	BSLT Feynman gauge	BSLT Coulomb gauge	ET Coulomb gauge
$m_{u,d}$	0.200	0.250	0.250
m_s	0.404	0.447	0.390
m_c	1.715	1.779	1.719
m_b	5.121	5.199	5.096
κ	0.33	0.33	0.33
c	-0.8	-1.0	-1.0
ε	0.2	0.25	0.2
α_{sat}	0.8	0.8	0.8
running type	$\alpha_I, \mu = 1$	$\alpha_I, \mu = 1$	α_{II}

We determine the strength of the confinement from the condition that the experimental Regge-slope $\beta \simeq 1.2 \text{ GeV}^2$ of the light meson spectrum is found. If the confinement is taken purely scalar then a confinement strength $\kappa \approx 0.5 \text{ GeV}^2$ is needed. This is much stronger than the strength that gives a good description of the cc and bb systems in nonrelativistic models. Since we want to describe the light and heavy mesons with one flavor-independent potential we are therefore forced to introduce a vector part in the confining potential, and we take the maximum of allowed vector admixture which gives a maximum Regge-slope at a fixed confinement strength. So in the BSLT model we take $\varepsilon = 0.2$ in the Feynman gauge and $\varepsilon = 0.25$ in the Coulomb gauge. With these values the experimental Regge-slopes of the light mesons are reproduced at $\kappa \simeq 0.33 \text{ GeV}^2$. Although this strong confinement is compatible with the lattice result $\kappa = 0.33_{-0.23}^{+0.82} \text{ GeV}^2$ [53], it makes it difficult to get a perfect fit for the heavy quark systems. As can be seen from Table 2.1 and Figs. 2.7 and 2.8, an increase of vector confinement in the Feynman gauge in the ET model gives an increase in the Regge-slopes at the spin-triplet states but a decrease at the spin-singlet states. It is therefore impossible in the ET model in the Feynman gauge to obtain simultaneously a fair description of the heavy mesons and of the Regge-slopes of the light mesons, so for the fit of the meson mass spectrum we only used the ET model in the Coulomb gauge. For this last case we took the value $\varepsilon = 0.2$ which is slightly less than the maximum $\varepsilon = 0.25$; above $\varepsilon \simeq 0.2$ the spatial extension of the ${}^1J_J^c$ components becomes more than $\sim 10 \text{ fm}$ which is unphysically large.

For the OGE part of the potential the choice of the saturation value α_{sat} of the running coupling constant is not important since it only plays a role at large distances where the confining part dominates. Fair fits can be found with $\alpha_{\text{sat}} = 0.6$ as well with $\alpha_{\text{sat}} = 1.0$. We choose the commonly accepted value $\alpha_{\text{sat}} = 0.8$. The typical range of the running coupling constant regime is much more important. In

the Coulomb gauge the maximum fixed coupling constants allowed in the BSLT and in ET model are respectively $\alpha_{\max} = 8/(3\pi) \simeq 0.85$ and $\alpha_{\max} = 4/(3\pi) \simeq 0.42$ [see Eqs. (2.B.81) and (2.B.85)]. If the running coupling constant regime is small and the saturation value is approximately equal or larger than the maximum allowed fixed coupling constant, $\alpha_{\text{sat}} \gtrsim \alpha_{\max}$, then at medium small distances the wave function exhibits the singular behavior of the fixed coupling constant equations. Especially, the spectrum shows much lower energies for the 1S_0 states than the nonrelativistic spectrum. Since α_{\max} is rather low in the ET model this effect occurs rather strongly in the ET spectrum, and one must choose a much larger running coupling regime for the ET equations than for the BSLT equations. So we use for the BSLT model the coupling α_I of Eq. (2.3.39) and for the ET model the coupling α_{II} of Eq. (2.3.40). Yet, even with this choice the 1S_0 states are considerably lower in the ET fit than in the BSLT fits.

The masses of the u and d quarks are taken equal and chosen together with the constant c to give a fair description of the light non-strange mesons. Next the masses of the s, c, and b quarks are fitted to the 3S_1 states K^* , J/ψ and Υ , except for the c mass in the ET model where a correct K^* mass would lead to a far too low K mass.

Table 2.3 presents the resulting mass spectra of the BSLT approach in both the Feynman and in the Coulomb gauge and of the ET approach in the Coulomb gauge, together with the known experimental mass spectrum. As can be seen from these numbers the BSLT approach in the Feynman gauge gives the best description, but the differences between the BSLT results obtained from the Feynman gauge and those from the Coulomb gauge are minor. The ET model does not give a very good spectrum.

Let us discuss the spectra in more detail. The ground states of the $d\bar{d}$ and $d\bar{s}$ systems, the π and K mesons, are considerably lighter than the BSLT fits predict. The light masses of these mesons are commonly explained within in the framework of broken chiral symmetry where these mesons correspond to almost massless Goldstone bosons. Since the quasipotential equations do not incorporate the chiral symmetry they give too heavy π and K . The correct mass of the π in the ET is a coincidence and due to the too singular behavior of the 1S_0 states in the ET model.

The description of the 1P_1 -states in the ET model is not good. According to the Breit reduction of the potential, the mass of this state should be equal to the center of gravity of the 3P states up to order $1/m^2$. Clearly none of the 1P_1 -states in the ET model satisfy this condition, in contrast to the BSLT model where this condition is more or less satisfied. In Section 3.3 it is shown that this is due to the too strong propagation of the double negative energy states in the ET model, and that better results are found if these states are omitted. The splittings between the various 3S_1 and 3D_1 states, especially in the dd and $d\bar{s}$ system, are much too small in the ET model. We conclude that the ET model with the double negative energy

Table 2.3: The meson mass spectrum (in GeV). The experimental data are from the particle data group [61]. Numbers between brackets need confirmation. Only experimental errors larger than 0.01 GeV are given. The column labeled $N^{2S+1}L_J$ displays the quantum numbers of the main component of the wave function. Underlined values have been fitted. The most satisfying results are found from the BSLT using the Feynman gauge.

quark content	meson	J^{PC}	$N^{2S+1}L_J$	Observed mass	BSLT Feynman	BSLT Coulomb	FT Coulomb
uu, dd	π	0^{-+}	1^1S_0	0.135	0.439	0.521	0.134
	π'	0^{-+}	2^1S_0	1.30 ± 0.10	1.441	1.424	1.361
	π''	0^{-+}	3^1S_0	(1.77 ± 0.03)	2.246	2.193	1.978
	ρ	1^{--}	1^3S_1	0.768	0.798	0.796	0.838
	ρ'	1^{--}	1^3D_1	1.47 ± 0.03	1.454	1.470	1.613
	ρ''	1^{--}	2^3S_1	1.70 ± 0.02	1.653	1.594	1.649
	ρ'''	1^{--}	2^3D_1	(2.14 ± 0.03)	2.185	2.180	2.230
	ρ''''	1^{--}	3^3S_1		2.367	2.308	2.248
	b_1	1^{+-}	1^1P_1	1.23	1.091	1.136	1.196
	a_0	0^{++}	1^3P_0	0.983	0.993	1.001	1.186
	a_1	1^{++}	1^3P_1	1.26 ± 0.03	1.126	1.142	1.249
	a_2	2^{++}	1^3P_2	1.318	1.297	1.277	1.311
	π_2	2^{-+}	1^1D_2	1.67 ± 0.02	1.524	1.552	1.569
	b_3	3^{+-}	1^1F_3		1.886	1.896	1.820
	π_4	4^{-+}	1^1G_4		2.205	2.198	2.011
	b_5	5^{+-}	1^1H_5		2.494	2.471	2.164
	π_6	6^{-+}	1^1I_6		2.761	2.722	2.291
	ρ_3	3^{--}	1^3D_3	1.69	1.689	1.654	1.660
	a_4	4^{++}	1^3F_4	(2.04 ± 0.03)	2.021	1.973	1.946
	ρ_5	5^{--}	1^3G_5	(2.35)	2.314	2.253	2.191
a_6	6^{++}	1^3H_6	(2.45 ± 0.13)	2.583	2.507	2.407	
ρ_2	2^{--}	1^3D_2		1.547	1.562	1.624	
a_3	3^{++}	1^3F_3	(2.08 ± 0.04)	1.897	1.903	1.904	
ρ_4	4^{--}	1^3G_4		2.202	2.199	2.133	
a_5	5^{++}	1^3H_5		2.479	2.465	2.330	
ρ_6	6^{--}	1^3I_6		2.732	2.709	2.503	

continued on next page →

Table 2.3: Continued.

quark content	meson	J^{PC}	$N^{2S+1}L_J$	Observed mass	BSLT Feynman	BSLT Coulomb	ET Coulomb	
d \bar{s}	K	0^-	1^1S_0	0.498	0.593	0.660	0.350	
	K'	0^-	2^1S_0	(1.46)	1.560	1.530	1.457	
	K''	0^-	3^1S_0	(1.83)	2.326	2.268	2.069	
	K^*	1^-	1^3S_1	0.896	<u>0.896</u>	<u>0.896</u>	0.910	
	$K^{*'}$	1^-	1^3D_1	1.41	1.584	1.599	1.692	
	$K^{*''}$	1^-	2^3S_1	1.71 ± 0.02	1.727	1.680	1.700	
	K_1	1^+	1^1P_1	1.27	1.232	1.257	1.282	
	K_0^*	0^+	1^3P_0	1.43	1.113	1.129	1.262	
	K_1'	1^+	1^3P_1	1.40	1.261	1.268	1.333	
	K_2^*	2^+	1^3P_2	1.425	1.389	1.373	1.376	
	K_2	2^-	1^1D_2	1.77	1.655	1.669	1.672	
	K_3	3^+	1^1F_3	(2.32 ± 0.02)	2.005	2.008	1.943	
	K_4	4^-	1^1G_4	(2.49 ± 0.02)	2.331	2.304	2.153	
	K_5	5^+	1^1H_3		2.590	2.571	2.326	
	K_3^*	3^-	1^3D_3	1.77	1.776	1.749	1.726	
	K_4^*	4^+	1^3F_4	2.05	2.107	2.069	2.018	
	K_5^*	5^-	1^3G_5	(2.38 ± 0.03)	2.399	2.350	2.271	
	uc	D	0^-	1^1S_0	1.864	1.868	1.912	1.855
		D^*	1^-	1^3S_1	2.007	2.015	2.032	2.058
		D_1	1^+	1^1P_1	2.42	2.388	2.404	2.423
D_0^*		0^+	1^3P_0		2.321	2.327	2.632	
D_1'		1^+	1^3P_1		2.415	2.420	2.494	
D_2^*		2^+	1^3P_2	2.459	2.458	2.461	2.474	
D_s		0^-	1^1S_0	1.969	1.952	1.983	1.939	
s \bar{c}	D_s^*	1^-	1^3S_1	(2.110)	2.104	2.110	2.115	
	D_{s1}	1^+	1^1P_1	2.537	2.500	2.509	2.491	
	D_{s0}^*	0^+	1^3P_1		2.427	2.419	2.510	
	D'_{s1}	1^+	1^3P_1		2.516	2.502	2.550	
	D_{s2}^*	2^+	1^3P_2	(2.564)	2.569	2.559	2.547	

continued on next page \rightarrow

Table 2.3: Continued.

quark content	meson	J^{PC}	$N^{2S+1}L_J$	Observed mass	BSLT Feynman	BSLT Coulomb	ET Coulomb	
$c\bar{c}$	η_c	0^{-+}	1^1S_0	2.980	2.969	2.988	2.883	
	η'_c	0^{-+}	2^1S_0	(3.59)	3.742	3.713	3.680	
	J/ψ	1^{--}	1^3S_1	3.097	<u>3.096</u>	<u>3.098</u>	<u>3.097</u>	
	ψ'	1^{--}	2^3S_1	3.686	3.810	3.779	3.789	
	ψ''	1^{--}	1^3D_1	3.770	3.873	3.854	3.872	
	ψ'''	1^{--}	3^3S_1	4.04	4.370	4.325	4.308	
	ψ^{iv}	1^{--}	2^3D_1	4.16 ± 0.02	4.409	4.372	4.363	
	ψ^v	1^{--}	3^3S_1	4.42	4.860	4.805	4.744	
	h_{c1}	1^{+-}	1^1P_1	3.526^a	3.517	3.513	3.486	
	χ_{c0}	0^{++}	1^3P_0	3.415	3.461	3.442	3.486	
	χ_{c1}	1^{++}	1^3P_1	3.511	3.526	3.510	3.521	
	χ_{c2}	2^{++}	1^3P_2	3.556	3.572	3.559	3.553	
	$d\bar{b}$	B	0^-	1^1S_0	5.279	5.302	5.331	5.349
		B^*	1^-	1^3S_1	5.324	5.360	5.383	5.391
B_1		1^+	1^1P_1		5.741	5.756	5.741	
B_0^*		0^+	1^3P_0		5.714	5.717	5.800	
B_1'		1^+	1^3P_1		5.760	5.766	5.817	
B_2^*		2^+	1^3P_2		5.770	5.781	5.760	
$s\bar{b}$		B_s	0^-	1^1S_0	(5.38 ± 0.03)	5.371	5.383	5.390
	B_s^*	1^-	1^3S_1	(5.43 ± 0.03)	5.434	5.443	5.441	
	B_{s1}	1^+	1^1P_1		5.839	5.841	5.805	
	B_{s0}^*	0^+	1^3P_0		5.802	5.789	5.848	
	B_{s1}'	1^+	1^3P_1		5.846	5.838	5.865	
	B_{s2}^*	2^+	1^3P_2		5.869	5.866	5.827	
	$c\bar{b}$	B_c	0^-	1^1S_0		6.260	6.260	6.228
B_c^*		1^-	1^3S_1		6.331	6.329	6.336	
B_{c1}		1^+	1^1P_1		6.760	6.754	6.719	
B_{c0}^*		0^+	1^3P_0		6.724	6.702	6.724	
B_{c1}'		1^+	1^3P_1		6.767	6.745	6.742	
B_{c2}^*		2^+	1^3P_2		6.794	6.781	6.758	

^a Ref. [1].*continued on next page* \rightarrow

Table 2.3: Continued.

quark content	meson	J^{PC}	$N^{2S+1}L_J$	Observed mass	BSLT Feynman	BSLT Coulomb	ET Coulomb
$b\bar{b}$	η_b	0^{-+}	1^1S_0		9.401	9.402	9.350
	η'_b	0^{-+}	2^1S_0		10.067	10.047	9.980
	Υ	1^{--}	1^3S_1	9.460	<u>9.460</u>	<u>9.459</u>	<u>9.460</u>
	Υ'	1^{--}	2^3S_1	10.023	10.099	10.081	10.039
	Υ''	1^{--}	1^3D_1		10.206	10.187	10.138
	Υ'''	1^{--}	3^3S_1	10.355	10.556	10.532	10.467
	Υ^{iv}	1^{--}	2^3D_1		10.629	10.603	10.533
	Υ^v	1^{--}	4^3S_1	10.58	10.943	10.911	10.827
	h_{b1}	1^{+-}	1^1P_1		9.881	9.879	9.823
	χ_{b0}	0^{++}	1^3P_0	9.860	9.862	9.843	9.831
	χ_{b1}	1^{++}	1^3P_1	9.892	9.890	9.876	9.845
	χ_{b2}	2^{++}	1^3P_2	9.913	9.911	9.901	9.863
	h'_{b1}	1^{+-}	2^1P_1		10.383	10.363	10.288
	χ'_{b0}	0^{++}	2^3P_0	10.232	10.363	10.335	10.289
	χ'_{b1}	1^{++}	2^3P_1	10.255	10.384	10.360	10.301
	χ'_{b2}	2^{++}	2^3P_2	10.268	10.400	10.379	10.316

states included does not give the correct fine structure. At this point we would like to note that within a constituent quark model with flavor independent potential it is not possible to have simultaneously a correct description of the P -states in the $d\bar{d}$ and $d\bar{s}$ systems. The only difference between these systems is that one of the constituent quarks is a little heavier, so it can be expected that the levels of the $d\bar{s}$ system are raised a little as compared to the levels of the $d\bar{d}$ system, with a little smaller fine structure splitting. The observed spacings between the P -states of the $d\bar{d}$ and $d\bar{s}$ mesons do not follow this pattern, however.

2.6.1 Improving the heavy meson spectrum

Moderate deviations between the experimental masses and the calculated masses appear in the excited states of the cc and $b\bar{b}$ systems. This is due to the large confinement strength κ that was chosen in order to have proper Regge-slopes for the light mesons. We have searched for various simple prescriptions to improve on the potential in such a way that the masses of the excited states of the heavy systems show better agreement. In this Subsection two such prescriptions are discussed. The first one is based on a modification of the spatial dependence of the confining potential for short distances. In the second approach the Lorentz structure of the confining potential is adjusted.

The masses of the heavy mesons are partially determined by the behavior of the confining potential at short distances, whereas the Regge-slopes of the light mesons is mostly determined by the strength of the confining potential at large distances. This clearly suggests that maybe a better overall description can be found if one takes a smaller κ at short distances than at large distances. We examined this possibility by modifying the potential at short distances according to

$$V_{\text{conf}}(x) \rightarrow \tilde{V}_{\text{conf}}(x) = \begin{cases} \kappa'x + c' + Ax^2 & x < x_0, \\ \kappa x + c & x > x_0, \end{cases} \quad (2.6.47)$$

with the two regions smoothly matching, $\kappa' < \kappa$, $A > 0$ and various character (vector or scalar) for $\tilde{V}_{\text{conf}} - V_{\text{conf}}$. We found that it was indeed possible to get the right Regge-slopes for the light mesons and simultaneously the $b\bar{b}$ excitations at the correct levels. But this also increased the fine structure splittings in the non-strange P -states up to values as 0.3 GeV for the difference $M(a_2) - M(a_1)$ which is known to be only 0.051 GeV. Furthermore, the decrease of the splitting $M(2^3P_1) - M(1^3S_1)$ in $b\bar{b}$ caused almost a similar reduction of the shift $M(1^3P_1) - M(1^3S_1)$ in $c\bar{c}$ which is undesirable. These two differences depend more or less in the same way on the potential since the excited levels 2^3P_1 of $b\bar{b}$ and 1^3P_1 of $c\bar{c}$ both have approximately the same spatial extension.

We also examined the possibilities for improving the heavy meson spectrum by changing the Lorentz structure of the confining potential. A different Lorentz

structure may lead to steeper Regge-slopes than the mainly scalar confinement. With such a Lorentz structure the correct Regge-slopes $\beta \simeq 1.2 \text{ GeV}^2$ of the light mesons can already be obtained at $\kappa \simeq 0.2 \text{ GeV}^2$, which value is known to give a good description of the heavy mesons. It should be mentioned that nonrelativistic fits to the heavy mesons suggest that this structure should be dominantly scalar, and that theoretical arguments exist [31] which admit pseudoscalar and pseudovector and tensor contributions to the confining potential, but which exclude vector admixtures. An indication of the effect of the different Lorentz structures on the Regge-slopes is provided by the spin-independent Breit corrections up to order $1/m^2$ of these potentials [52]. These are small for the pseudo and tensor contributions, and our numerical results confirm that these contributions do not lead to a significant improvement of the mass spectra.

However, a small admixture of vector confinement can greatly increase the Regge-slopes, as was discussed in Section 2.5. Unfortunately Klein's paradox leads to an upper bound on this admixture which prevents one from taking a vector admixture large enough to give $\beta \simeq 1.2 \text{ GeV}^2$ at $\kappa \simeq 0.2 \text{ GeV}^2$. We can circumvent this paradox by restricting the QP models to positive energy states only, in which case the upper bound on the vector confinement is absent, and then we can take as much vector confinement as necessary. The method of solution of the QP equations with only positive energy states is discussed in Chapter 3.

In absence of the negative energy states, we find that the requirements $\kappa \simeq 0.2 \text{ GeV}^2$ and $\beta \simeq 1.2 \text{ GeV}^2$ are satisfied for an admixture of vector confinement $\varepsilon \simeq 0.5$. Here, the differences between the BSLT and ET dynamics, and between the Coulomb and Feynman gauge are of the order of 10%, and the Feynman gauge and the BSLT model give the largest β . With these κ and ε we searched for better fits to the light and heavy meson mass spectra. In this way we could reproduce the known $c\bar{c}$ and $b\bar{b}$ masses within $\sim 0.05 \text{ GeV}$. Here the largest deviations are due to the spin-orbit corrections introduced by the vector contribution, which lead to rather large splittings between the 3P -states. It is likely that the spectrum can be improved further by adjusting the running behavior of the strong coupling constant $\alpha(x)$. The large ε leads to the correct Regge-slopes of the light mesons, but it gives rather close spacings between the radially excited states. For example, we now find $M(\rho''') \sim 1.8 \text{ GeV}$, whose (unconfirmed) experimental value is $\simeq 2.14 \text{ GeV}$. Furthermore, the large vector contribution leads to far too large spin-orbit splittings between the light 3P -states (a_0, a_1, a_2). For $m_{u,d} = 0.25 \text{ GeV}$ we now find that $M(a_2) - M(a_0) \sim 0.6 \text{ GeV}$, whereas the experimental value is only 0.335 GeV . These theoretical 3P -splittings may be reduced by increasing the quark masses; then we recover the experimental splitting at the unbelievable large value $m_{u,d} \sim 0.8 \text{ GeV}$.

2.7 Concluding remarks

We studied two approximations to the Bethe-Salpeter equation for the two-quark system, the Blankenbecler-Sugar-Logunov-Tavkhelidze (BSLT) equation and an equal-time (ET) equation. In these quasipotential approximations the relative energy dependence of the wave function was eliminated by assuming a simplified form for the two-body propagator. The full Dirac structure of positive and negative energy states was kept. Both two-body propagators reduce to the one-body Dirac propagator if one of the particles is taken infinitely heavy. We applied these equations to a system of two constituent quarks interacting through a phenomenological potential which consisted of two parts. The first part was a Coulomb-like one-gluon-exchange (OGE) part, the second part was a linear confining potential which was taken mostly scalar-like and partly vector-like. For the vector part we studied both the Feynman and the Coulomb gauge. Since the confining potential is highly singular in momentum space we transformed the quasipotential equations to configuration space.

It was shown that for a fixed coupling constant for the OGE potential a maximum value exists —depending on the model and gauge— above which the ground state solutions no longer exist. Also the admixture of vector character in the confining potential has a maximum value (20% and 25% in the Feynman and Coulomb gauge respectively), above which some mesons become unbound. The latter effect could be explained from the repulsion between positive and negative energy states. We found linear Regge-trajectories for both models and gauges, but their Regge-slopes were much smaller than predicted by Schrödinger-like models.

Using the BSLT and ET equations we calculated the full known meson mass spectrum of all light and heavy mesons. As compared to the nonrelativistic model predictions [29] given the limited number of parameters used here, the fit can be considered satisfactory. We believe that our prediction of the spectrum is of comparable or better quality than other relativistic studies based on quasipotential and Dirac equations [18, 33]. We found only a small gauge dependence in the BSLT spectrum. For the ET equation we only used the Coulomb gauge since it was impossible to get satisfying Regge-slopes in the Feynman gauge. The fine structure of the spectrum, such as the spacings between the P -states and between the 3S_1 and 3D_1 states, as calculated from the ET equations did not follow the experimental spacings nor did it follow predictions of the Breit reduction of the potential. The BSLT fine structure agreed more or less with these predictions. Probably the moderate deviations that were found between the calculated meson mass spectrum and the experimental spectrum can be reduced by introducing some flavor dependence in the confining potential such that the confining strength is less for the heavy quark systems. Also, one would like to incorporate chiral symmetry in the model in order to reproduce the correct π and K mass.

The wave functions found in these calculations can in principle be used to

perform relativistic covariant calculations on interactions between mesons and other particles. Especially at high momenta significant deviations from the nonrelativistic calculations can be expected; this will be discussed in Chapter 4.

2.A Partial wave projection

In this Appendix we describe the projection of the potential and the BSLT and ET equations on sets of basis states with definite spin and orbital momentum. The equations and basis states are formulated for a two-quark system; they can easily be transformed to a quark-antiquark system by performing a charge-conjugation on one of the quarks. The complete meson wave function is written as a combination of the states $|JLSJ_z\rangle \otimes |\rho_z^{(1)}\rho_z^{(2)}\rangle \otimes \chi_{\text{color}} \otimes \chi_{\text{flavor}}$. The color and flavor parts of the wave function are well-known and can be found e.g. in Ref. [29]. For the ρ -spin basis states we do not use the energy eigenstates projected out by the $\Lambda^{\rho_1\rho_2}$, but instead the four eigenstates of $\gamma_0^{(1)}\gamma_0^{(2)}$, corresponding to the four combinations of upper and lower components of the quark spinors. The energy eigenstates have the advantage that the propagator is simply diagonal on this basis as is shown by Eqs. (2.2.19) and (2.2.31). However, on this basis the matrix elements of the potential are complicated and many in number. In principle it is possible to transform them all to configuration space, but the numerical work involved is huge. On the other hand, on the basis of the eigenstates of $\gamma_0^{(1)}\gamma_0^{(2)}$ the matrix elements of the potential are almost trivial, whereas the projection of the propagator on this set gives only a limited number of functions to be transformed. For the BSLT propagator there is only one such function namely Z_{BSLT} (2.2.27), whereas for the ET propagator two functions Z_1 and Z_2 (2.2.26) are needed.

2.A.1 Blankenbecler-Sugar-Logunov-Tavkhelidze equation

We decompose the kinetic part of the BSLT propagator into pieces acting in the subspaces of the spin and rho-spin:

$$\begin{aligned} \not{p}_1 + \not{p}_2 &= i\boldsymbol{\gamma}^{(1)} \cdot \boldsymbol{\nabla} + E_1\gamma_0^{(1)} - i\boldsymbol{\gamma}^{(2)} \cdot \boldsymbol{\nabla} + E_2\gamma_0^{(2)} \\ &= -\rho_2^{(1)}\boldsymbol{\sigma}^{(1)} \cdot \boldsymbol{\nabla} + E_1\rho_3^{(1)} + \rho_2^{(2)}\boldsymbol{\sigma}^{(2)} \cdot \boldsymbol{\nabla} + E_2\rho_3^{(2)}. \end{aligned} \quad (2.A.48)$$

For a given total spin J there are four basis states for the spin subspace. In the spectroscopic notation $^{2S+1}L_J$ they are $\{^1J_J, ^3J_J, ^3(J-1)_J, ^3(J+1)_J\}$. After some

Clebsch-Gordan algebra one finds that on this basis

$$\boldsymbol{\sigma}^{(1)} \cdot \nabla = \begin{pmatrix} 0 & 0 & c_1 D_{-J+1} & -c_2 D_{J+2} \\ 0 & 0 & -c_2 D_{-J+1} & -c_1 D_{J+2} \\ c_1 D_{J+1} & -c_2 D_{J+1} & 0 & 0 \\ -c_2 D_{-J} & -c_1 D_{-J} & 0 & 0 \end{pmatrix}, \quad (2.A.49)$$

where

$$D_\ell = \frac{\partial}{\partial x} + \frac{\ell}{x}, \quad c_1 = \sqrt{\frac{J}{2J+1}}, \quad c_2 = \sqrt{\frac{J+1}{2J+1}}. \quad (2.A.50)$$

The matrix of $\boldsymbol{\sigma}^{(2)} \cdot \nabla$ is identical to Eq. (2.A.49), except for the first row and first column —these correspond to the antisymmetric spin-singlet state— which change sign. Let us combine the four eigenstates of $\gamma_0^{(1)} \gamma_0^{(2)}$ into the rho-spin combinations

$$\begin{aligned} s &= \frac{|++\rangle - |--\rangle}{\sqrt{2}}, & a &= \frac{|++\rangle + |--\rangle}{\sqrt{2}}, \\ e &= \frac{|+-\rangle + |-+\rangle}{\sqrt{2}}, & o &= \frac{|+-\rangle - |-+\rangle}{\sqrt{2}}. \end{aligned} \quad (2.A.51)$$

Phase factors i between the eigenstates are used according to

$$|++\rangle = -i\rho_1^{(1)}|-+\rangle = -i\rho_1^{(2)}|+-\rangle = \rho_1^{(1)}\rho_1^{(2)}|--\rangle. \quad (2.A.52)$$

This ensures that the final equations will be real. Following Kubis [45] and Gam-mel [27] we combine the spin and rho-spin bases to form the basis set \mathcal{B} of eight states with unnatural parity $P = (-)^{J+1}$,

$$\mathcal{B} = \{^1J_J^s, ^1J_J^a, ^3J_J^s, ^3J_J^a, ^3(J-1)_J^e, ^3(J-1)_J^o, ^3(J+1)_J^e, ^3(J+1)_J^o\}, \quad (2.A.53)$$

and the basis set \mathcal{B}^* of eight states with natural parity $P = (-)^J$,

$$\mathcal{B}^* = \{^1J_J^e, ^1J_J^o, ^3J_J^e, ^3J_J^o, ^3(J-1)_J^s, ^3(J-1)_J^a, ^3(J+1)_J^s, ^3(J+1)_J^a\}. \quad (2.A.54)$$

These basis states for two quarks can be related to the often used Dirac matrix set for a quark and an antiquark [51] by performing a charge conjugation on one of the spinors. The relation is shown in Table 2.4. Let us expand the expression Eq. (2.A.48)

Table 2.4: 16-component vector qq-basis states and corresponding 4×4 matrix qq-basis states. The angular dependence of the wave functions of the $q\bar{q}$ -triplet states must determine to which qq-triplet state they correspond. For a correct normalization, all matrix states should be multiplied by $1/2$; furthermore, matrix states proportional to P or p need an extra factor $1/M$ and $1/|p|$, respectively. The correspondence is only valid in the cm system and $p_0 = 0$ is assumed.

qq-state	$q\bar{q}$ -state
${}^1J_J^s$	$-\gamma_5 \not{P}$
${}^1J_J^a$	γ_5
${}^1J_J^e$	-1
${}^1J_J^o$	\not{P}
${}^3J_{J,J}^s, {}^3(J-1)_{J,J}^s, {}^3(J+1)_{J,J}^s$	$-\not{p}$
${}^3J_{J,J}^a, {}^3(J-1)_{J,J}^a, {}^3(J+1)_{J,J}^a$	$i\sigma_{\mu\nu}P^\mu p^\nu$
${}^3J_{J,J}^e, {}^3(J-1)_{J,J}^e, {}^3(J+1)_{J,J}^e$	$-\gamma_5 i\sigma_{\mu\nu}P^\mu p^\nu$
${}^3J_{J,J}^o, {}^3(J-1)_{J,J}^o, {}^3(J+1)_{J,J}^o$	$\gamma_5 \not{p}$

for $\not{p}_1 + \not{p}_2$ on the set \mathcal{B} (2.A.53) of unnatural parities and denote the resulting 8×8 matrix by $\mathbf{D}(x)$. This gives

$$\frac{\mathbf{D}}{2} = \begin{pmatrix} 0 & E & 0 & 0 & -c_1 D_{-J+1} & 0 & c_2 D_{J+2} & 0 \\ E & 0 & 0 & 0 & 0 & 0 & 0 & 0 \\ 0 & 0 & 0 & E & 0 & 0 & 0 & 0 \\ 0 & 0 & E & 0 & 0 & -c_2 D_{-J+1} & 0 & -c_1 D_{J+2} \\ -c_1 D_{J+1} & 0 & 0 & 0 & 0 & \Delta & 0 & 0 \\ 0 & 0 & 0 & -c_2 D_{J+1} & \Delta & 0 & 0 & 0 \\ c_2 D_{-J} & 0 & 0 & 0 & 0 & 0 & 0 & \Delta \\ 0 & 0 & 0 & -c_1 D_{-J} & 0 & 0 & \Delta & 0 \end{pmatrix}, \quad (2.A.55)$$

with $2E = E_1 + E_2 = M$ and $2\Delta = E_1 - E_2 = (m_1^2 - m_2^2)/M$. The matrix \mathbf{D}^* of $\not{p}_1 + \not{p}_2$ for the set \mathcal{B}^* (2.A.54) of natural parity states can be obtained from \mathbf{D} by interchanging $E \leftrightarrow \Delta$. The complete partial wave projected BSLT equation is the following set of eight coupled integro-differential equations

$$[\mathbf{D}(x) - \mathbf{M}]\psi(x) = \frac{1}{2(m_1 + m_2)} \int dx' x'^2 \mathbf{Z}_{\text{BSLT}}(x, x') [\mathbf{D}(x') + \mathbf{M}]\mathbf{V}(x')\psi(x'). \quad (2.A.56)$$

The matrix \mathbf{M} is equal to $m_1 + m_2$ times the identity, and the diagonal matrix \mathbf{Z}_{BSLT} has as i -th diagonal element the projection $Z_{\text{BSLT}}^{(i)}$ of Z_{BSLT} on the orbital

angular momentum ℓ_i of the i -th basis state,

$$Z_{\text{BSLT}}^{(\ell)}(x, x') = 2\pi \int_{-1}^1 d\gamma P_\ell(\gamma) Z_{\text{BSLT}}(\sqrt{x^2 + x'^2 - 2xx'\gamma}). \quad (2.A.57)$$

The number of coupled channels becomes less if the quarks have equal masses. In that case $\Delta = 0$ and the matrix \mathbf{D} for the the unnatural parity $P = (-)^{J+1}$ states falls apart into two 4×4 parts describing the charge-parity $C = (-)^J$ states and the $C = (-)^{J+1}$ states,

$$\{^1J_J^s, ^1J_J^a, ^3(J-1)_J^e, ^3(J+1)_J^e\} \quad \text{and} \quad \{^3J_J^s, ^3J_J^a, ^3(J-1)_J^o, ^3(J+1)_J^o\}, \quad (2.A.58)$$

respectively. If the masses are equal the set of natural parity $P = (-)^J$ states can be split into the $C = (-)^J$ states and the $C = (-)^{J+1}$ states,

$$\{^1J_J^e, ^3J_J^o, ^3(J-1)_J^s, ^3(J-1)_J^a, ^3(J+1)_J^s, ^3(J+1)_J^a\} \quad \text{and} \quad \{^1J_J^o, ^3J_J^e\}, \quad (2.A.59)$$

respectively. The latter $C = (-)^{J+1}$ set contains no $|++\rangle$ components and therefore it has no nonrelativistic analog. However since Eq. (2.A.56) is independent of \mathbb{E} for this case, no bound states exist in this sector.

2.A.2 Equal-time approximation

As with the BSLT propagator, the parts $\mathcal{S}_1(\mathbf{x})$ and $\mathcal{S}_2(\mathbf{x})$ in Eqs. (2.2.36) and (2.2.37) of the ET propagator can be projected on the partial wave bases. One finds for the set \mathcal{B} (2.A.53) of unnatural parity states

$$\mathbf{S}_1 = m_1 m_2 \mathbf{I} + \begin{pmatrix} \partial_J^2 & -m_1 E_2 & 0 & 0 \\ -m_1 E_2 & -\partial_J^2 & 0 & 0 \\ 0 & 0 & -\partial_J^2 & -m_1 E_2 \\ 0 & 0 & -m_1 E_2 & \partial_J^2 \\ c_1 A D_{J+1} & -c_1 E_2 D_{J+1} & c_2 B D_{J+1} & c_2 E_2 D_{J+1} \\ c_1 E_2 D_{J+1} & c_1 B D_{J+1} & -c_2 E_2 D_{J+1} & c_2 A D_{J+1} \\ -c_2 A D_{-J} & c_2 E_2 D_{-J} & c_1 B D_{-J} & c_1 E_2 D_{-J} \\ -c_2 E_2 D_{-J} & -c_2 B D_{-J} & -c_1 E_2 D_{-J} & c_1 A D_{-J} \end{pmatrix}$$

$$\begin{pmatrix}
c_1 A D_{-J+1} & c_1 E_2 D_{-J+1} & -c_2 A D_{J+2} & -c_2 E_2 D_{J+2} \\
-c_1 E_2 D_{-J+1} & c_1 B D_{-J+1} & c_2 E_2 D_{J+2} & -c_2 B D_{J+2} \\
c_2 B D_{-J+1} & -c_2 E_2 D_{-J+1} & c_1 B D_{J+2} & -c_1 E_2 D_{J+2} \\
-c_2 E_2 D_{-J+1} & c_2 A D_{-J+1} & c_1 E_2 D_{J+2} & c_1 A D_{J+2} \\
-\frac{1}{2J+1} \partial_{J-1}^2 & m_1 E_2 & -2c_1 c_2 H_2 & 0 \\
m_1 E_2 & \frac{1}{2J+1} \partial_{J-1}^2 & 0 & 2c_1 c_2 H_2 \\
-2c_1 c_2 H_1 & 0 & \frac{1}{2J+1} \partial_{J+1}^2 & m_1 E_2 \\
0 & 2c_1 c_2 H_1 & m_1 E_2 & -\frac{1}{2J+1} \partial_{J+1}^2
\end{pmatrix}, \tag{2.A.60}$$

with D_ℓ , c_1 , c_2 as defined in (2.A.50), $A = m_1 + m_2$, $B = m_1 - m_2$, and

$$H_1 = \frac{\partial^2}{\partial x^2} + \frac{-2J+1}{x} \frac{\partial}{\partial x} - \frac{-J^2+1}{x^2}, \tag{2.A.61}$$

$$H_2 = \frac{\partial^2}{\partial x^2} + \frac{2J+3}{x} \frac{\partial}{\partial x} - \frac{-J^2-2J}{x^2}, \tag{2.A.62}$$

$$\partial_\ell^2 = \frac{\partial^2}{\partial x^2} + \frac{2}{x} \frac{\partial}{\partial x} - \frac{\ell(\ell+1)}{x^2}. \tag{2.A.63}$$

The projection \mathbf{S}_1^* of \mathcal{S}_1 for the set \mathcal{B}^* (2.A.54) of natural parity states is given by

$$\mathbf{S}_1^* = \mathbf{T} \mathbf{S}_1 \mathbf{T}, \quad \mathbf{T} = \text{diag}(1, -1, 1, -1, 1, -1, 1, -1). \tag{2.A.64}$$

The projection \mathbf{S}_2 of \mathcal{S}_2 for the set \mathcal{B} can be expressed as

$$\mathbf{S}_2(m_1, m_2, E_1, E_2) = \mathbf{C} \mathbf{S}_1(m_2, m_1, E_2, E_1) \mathbf{C}, \tag{2.A.65}$$

with diagonal charge-parity matrix $\mathbf{C} = \text{diag}(1, 1, -1, -1, 1, -1, 1, -1)$. And finally,

$$\mathbf{S}_2^* = \mathbf{T} \mathbf{S}_2 \mathbf{T} \quad \text{or} \quad \mathbf{S}_2^*(m_1, m_2, E_1, E_2) = \mathbf{C}^* \mathbf{S}_1^*(m_2, m_1, E_2, E_1) \mathbf{C}^*, \tag{2.A.66}$$

with charge-parity matrix $\mathbf{C}^* = \mathbf{T} \mathbf{C} = \text{diag}(1, -1, -1, 1, 1, 1, 1, 1)$. The complete partial wave projected ET equation becomes the following set of eight coupled integro-differential equations

$$\int dx' x'^2 \left[\frac{1}{m_1} \mathbf{Z}_1(x, x') \mathbf{S}_1(x') + \frac{1}{m_2} \mathbf{Z}_2(x, x') \mathbf{S}_2(x') \right] \boldsymbol{\psi}(x') = -\mathbf{V}(x) \boldsymbol{\psi}(x). \tag{2.A.67}$$

The diagonal matrices \mathbf{Z}_i have as j-th diagonal element the projection $Z_i^{(\ell_j)}$ of Z_i on the orbital angular momentum ℓ_j of the j-th basis state,

$$Z_i^{(\ell)}(x, x') = 2\pi \int_{-1}^1 d\gamma P_\ell(\gamma) Z_i(\sqrt{x^2 + x'^2 - 2xx'\gamma}). \quad (2.A.68)$$

2.A.3 Potential

The vector structure of the $q\bar{q}$ interaction gives

$$\gamma_\mu^{(1)} \gamma^{\mu(2)} = \rho_3^{(1)} \rho_3^{(2)} + \rho_2^{(1)} \rho_2^{(2)} \boldsymbol{\sigma}^{(1)} \cdot \boldsymbol{\sigma}^{(2)} = \begin{pmatrix} 1+f & 0 & 0 & 0 \\ 0 & 1-f & 0 & 0 \\ 0 & 0 & -1+f & 0 \\ 0 & 0 & 0 & -1-f \end{pmatrix} \quad (2.A.69)$$

on the basis (2.A.51). Here $f = -3$ for spin-singlet states and $f = 1$ for spin-triplet states. Choosing the Coulomb gauge amounts to replacing

$$\boldsymbol{\sigma}^{(1)} \cdot \boldsymbol{\sigma}^{(2)} \rightarrow \frac{1}{2} \left[\boldsymbol{\sigma}^{(1)} \cdot \boldsymbol{\sigma}^{(2)} + \frac{(\boldsymbol{\sigma}^{(1)} \cdot \mathbf{x})(\boldsymbol{\sigma}^{(2)} \cdot \mathbf{x})}{x^2} \right]. \quad (2.A.70)$$

Thus in the Coulomb gauge the spin-spin interaction is reduced. The difference with the Feynman gauge can be expressed as

$$\frac{1}{2} \left[\boldsymbol{\gamma}^{(1)} \cdot \boldsymbol{\gamma}^{(2)} - \frac{(\boldsymbol{\gamma}^{(1)} \cdot \mathbf{x})(\boldsymbol{\gamma}^{(2)} \cdot \mathbf{x})}{x^2} \right] = \begin{pmatrix} 1 & 0 & 0 & 0 & 0 & 0 & 0 & 0 \\ 0 & -1 & 0 & 0 & 0 & 0 & 0 & 0 \\ 0 & 0 & 0 & 0 & 0 & 0 & 0 & 0 \\ 0 & 0 & 0 & 0 & 0 & 0 & 0 & 0 \\ 0 & 0 & 0 & 0 & -c_1^2 & 0 & c_1 c_2 & 0 \\ 0 & 0 & 0 & 0 & 0 & c_1^2 & 0 & -c_1 c_2 \\ 0 & 0 & 0 & 0 & c_1 c_2 & 0 & -c_2^2 & 0 \\ 0 & 0 & 0 & 0 & 0 & -c_1 c_2 & 0 & c_2^2 \end{pmatrix} \quad (2.A.71)$$

both for the bases (2.A.53) and (2.A.54). The constants c_i are given in Eq. (2.A.50).

2.B Short distance behavior of 1S_0 states

Here we discuss in detail the singular behavior of the wave function of the $J^P = 0^-$ states (e.g. pion), to which we refer as 1S_0 states for convenience because their wave functions contain mostly 1S_0 components. At short distances, or equivalently at high momenta, the masses of the two quarks can be neglected, so the short distance behavior for the unequal quark mass case is identical to the equal quark mass case. Thus in this Appendix only the equal mass case needs to be considered. Reference [36] gives an analysis of the short distance behavior for unequal masses near the one-body limit.

2.B.1 Blankenbecler-Sugar-Logunov-Tavkhelidze equation

Since $J = 0$ the $^3(J-1)_J^e$ state is removed from the basis in (2.A.58) and the wave function is decomposed as

$$\psi(x, \Omega) = \frac{1}{x} \left[\psi_1(x) |^1S_0^s \rangle + \psi_2(x) |^1S_0^a \rangle + \psi_3(x) |^3P_0^e \rangle \right]. \quad (2.B.72)$$

In this basis the BSLT equation (2.A.56) reduces to

$$\begin{aligned} & \begin{pmatrix} -m & E & D_1 \\ E & -m & 0 \\ D_{-1} & 0 & -m \end{pmatrix} \begin{pmatrix} \psi_1(x) \\ \psi_2(x) \\ \psi_3(x) \end{pmatrix} = \\ & \frac{1}{4m} \int_0^\infty dx' xx' \begin{pmatrix} Z^{(0)}(x, x') & 0 & 0 \\ 0 & Z^{(0)}(x, x') & 0 \\ 0 & 0 & Z^{(1)}(x, x') \end{pmatrix} \begin{pmatrix} m & E & D_1 \\ E & m & 0 \\ D_{-1} & 0 & m \end{pmatrix} \\ & \times \left[\begin{pmatrix} -2 & 0 & 0 \\ 0 & 4 & 0 \\ 0 & 0 & 0 \end{pmatrix} V_V(x') + \begin{pmatrix} 1 & 0 & 0 \\ 0 & 1 & 0 \\ 0 & 0 & 1 \end{pmatrix} V_S(x') \right] \begin{pmatrix} \psi_1(x') \\ \psi_2(x') \\ \psi_3(x') \end{pmatrix}. \end{aligned} \quad (2.B.73)$$

In this formula $E = M/2$ and $V_V(x)$ and $V_S(x)$ denote the vector and scalar part of the $q\bar{q}$ potential. The Feynman gauge is assumed. We first consider the case of a fixed coupling constant α . Assuming that $\psi_i(x) = c_i x^{\gamma_i}$ for $x \rightarrow 0$ one can reduce in

leading order in x the BSLT equation to

$$\begin{cases} -mc_1x^{\gamma_1} \\ +Ec_2x^{\gamma_2} + c_3(\gamma_3 + 1)x^{\gamma_3-1} \end{cases} = -\frac{\alpha}{4} \left[-2mc_1x^{\gamma_1}I^{(0)}(\gamma_1) + 4Ec_2x^{\gamma_2}I^{(0)}(\gamma_2) \right] \\ \begin{cases} Ec_1x^{\gamma_1} - mc_2x^{\gamma_2} \\ c_1(\gamma_1 - 1)x^{\gamma_1-1} - mc_3x^{\gamma_3} \end{cases} = -\frac{\alpha}{4} \left[-2Ec_1x^{\gamma_1}I^{(0)}(\gamma_1) + 4mc_2x^{\gamma_2}I^{(0)}(\gamma_2) \right] \\ = -\frac{\alpha}{4} \left[-2c_1(\gamma_1 - 2)x^{\gamma_1-1}I^{(1)}(\gamma_1 - 1) \right], \end{cases} \quad (2.B.74)$$

where the $I^{(\ell)}$ follow from

$$\frac{1}{m} \int_0^\infty dx' xx' Z^{(\ell)}(x, x') x'^{\gamma-1} = x^\gamma I^{(\ell)}(\gamma), \quad (2.B.75)$$

which is well-defined if $x \rightarrow 0$ and $|\gamma| < 1$. Assuming that Eq. (2.B.74) does not solely determine the energy eigenvalue E , we may exclude the case that $\gamma_1 = \gamma_2$. As a result we find that the exponents satisfy $\gamma_2 < \gamma_1$, $\gamma_3 = \gamma_2 + 1$ and $\alpha^{-1} = I^{(0)}(\gamma_2)$. Taking the explicit form of

$$Z^{(0)}(x, x') = \frac{m}{\pi xx'} \left[K_0(m|x - x'|) - K_0(m|x + x'|) \right] \quad (2.B.76)$$

we get

$$I^{(0)}(\gamma) = \frac{1}{\pi} \int_0^1 \frac{d\eta}{\eta} \ln \left(\frac{1+\eta}{1-\eta} \right) (\eta^\gamma + \eta^{-\gamma}) = \frac{1}{\gamma} \tan \frac{\pi\gamma}{2}. \quad (2.B.77)$$

Explicit expressions for general $I^{(\ell)}$ are given in Ref. [58]. Hence

$$\alpha = \frac{1}{I^{(0)}(\gamma_2)} \leq \frac{2}{\pi}. \quad (\text{BSLT-Feynman}) \quad (2.B.78)$$

This may be compared with the asymptotic behavior of the BSE [34], where

$$\gamma_2 = \gamma_3 - 1 = \sqrt{1 - \frac{4\alpha}{\pi}} \rightarrow \alpha \leq \frac{\pi}{4}, \quad (\text{BSE}) \quad (2.B.79)$$

$$\gamma_1 = \gamma_4 = \sqrt{5 - 2\sqrt{4 + \frac{\alpha}{\pi} \left(1 + \frac{\alpha}{\pi} \right)}}. \quad (\text{BSE}) \quad (2.B.80)$$

Here γ_4 is the exponent of the $^3P_0^o$ component which does not decouple in the BSE. Note that the dependence of γ_2 on α is to first order identical for the BSLT equation as for the BSE.

Replacing the Feynman gauge by the Coulomb gauge gives

$$\alpha = \frac{2}{3}\gamma_2(1 - \gamma_2)I^{(0)}(1 - \gamma_2) \leq \frac{4}{3\pi}. \quad (\text{ET-Coulomb}) \quad (2.B.85)$$

The same singular behavior has been found by Murota [58] for the Salpeter equation, which is obtained from the FT equation by removing the $|+-\rangle$ and $|-+\rangle$ components.

If the short distance attraction of the Coulomb-like potential is weakened by taking a running coupling constant $\alpha(x) \sim \ln^{-1}(x)$ then the singular short distance behavior of the ψ_i is also weakened to $\psi(x) = c_i |\ln(x)|^{\gamma_i}$. However, to numerically construct the solutions to the quasipotentials equations it is not necessary to know the expressions for the γ_i . The equations can be solved by assuming the singular behavior associated with a fixed coupling constant which is taken equal to the running coupling constant at a typical small distance.

2.C Bethe-Salpeter equation

The Bethe-Salpeter equation (BSE) can also be formulated in configuration space, completely analogous to the QP equations. An analysis of its short distance behavior is given in Ref. [34], and the form of BSE wave functions for large distances is discussed by Ref. [66]. The BSE is more complicated since it is a partial differential equation depending both on the relative distance x and the relative time t . Yet it is also simpler than the QP equations since it is local. As a consequence the corresponding equation for the spline coefficients has sparse matrices and does not need much computer memory.

In the QP equations the short distance singularity is only present at one point, the origin, but in the BSE this singularity is more complicated because it covers the whole light-cone. Probably it can be handled in the same way as it was treated in the QP equations: its analytical behavior must be analyzed and split off from the BSE equation. It will be difficult for the $q\bar{q}$ system to perform a Wick rotation to complex times in order to reduce the light-cone singularity to a single point. In his proof of the analyticity of the continuation to complex energies, Wick needs a positive binding energy [75], which is generally not at hand in qq systems. Furthermore, it can easily be shown that any potential that is a function of $t^2 - x^2$ and that reduces to a confining potential in the nonrelativistic limit by taking $V_{\text{NR}}(r) = \int dt V(t^2 - x^2)$ must have an infinite number of singularities. These singularities should be accounted for if the potential is continued to complex times. Note that the potential

$$V(t, x) = \begin{cases} \frac{\kappa}{2} & t^2 - x^2 < 0 \\ 0 & t^2 - x^2 > 0, \end{cases} \quad (2.C.86)$$

which reduces to a linear confining potential in the nonrelativistic limit, becomes a constant after Wick rotation.

A popular extension of the confining potential to a four-momentum dependence is based on the replacement $\mathbf{q}^2 \rightarrow \mathbf{q}^2 - q_0^2$ in the nonrelativistic potential, as in Eq. (3.4.21). Here one should be *very* careful in the treatment of the singularity at zero momentum. Apart of the precautions needed for handling the q^{-4} singularity, also attention should be paid to the choice and effects of the infinitely small imaginary part in the potential. The choice determines whether the Fourier transform to configuration space yields the potential of Eq. (2.C.86) or the senseless potential of Eq. (3.4.22) or something else.

After these caveats let us now give the partial wave projection of the BSE. The BSE Eq. (2.1.1) reads in configuration space in the cm system

$$S^{-1}(t, \mathbf{x})\psi(t, \mathbf{x}) = -V(t, \mathbf{x})\psi(t, \mathbf{x}), \quad (2.C.87)$$

with

$$S^{-1}(t, \mathbf{x}) = (-i\partial\!\!\!/ + m_1)^{(1)}(-i\partial\!\!\!/ + m_2)^{(2)}. \quad (2.C.88)$$

The partial wave projection of the inverse propagator yields for the set \mathcal{B} (2.A.53) of unnatural parity states

$$\mathbf{S}^{-1} = m_1 m_2 \mathbf{I} + \begin{pmatrix} \partial_J^2 + \bar{E}_1 \bar{E}_2 & -m_1 \bar{E}_2 - m_2 \bar{E}_1 & 0 & 0 \\ -m_1 \bar{E}_2 - m_2 \bar{E}_1 & -\partial_J^2 + \bar{E}_1 \bar{E}_2 & 0 & 0 \\ 0 & 0 & -\partial_J^2 + \bar{E}_1 \bar{E}_2 & -m_1 \bar{E}_2 - m_2 \bar{E}_1 \\ 0 & 0 & -m_1 \bar{E}_2 - m_2 \bar{E}_1 & \partial_J^2 + \bar{E}_1 \bar{E}_2 \\ c_1 A D_{J+1} & -2c_1 E D_{J+1} & c_2 B D_{J+1} & -2c_2 \bar{\Delta} D_{J+1} \\ -2c_1 \bar{\Delta} D_{J+1} & c_1 B D_{J+1} & -2c_2 E D_{J+1} & c_2 A D_{J+1} \\ -c_2 A D_{-J} & 2c_2 E D_{-J} & c_1 B D_{-J} & -2c_1 \bar{\Delta} D_{-J} \\ 2c_2 \bar{\Delta} D_{-J} & -c_2 B D_{-J} & -2c_1 E D_{-J} & c_1 A D_{-J} \end{pmatrix}$$

$$\left(\begin{array}{cccc}
c_1 AD_{-J+1} & -2c_1 \Delta D_{-J+1} & -c_2 AD_{J+2} & 2c_2 \Delta D_{J+2} \\
-2c_1 ED_{-J+1} & c_1 BD_{-J+1} & 2c_2 ED_{J+2} & -c_2 BD_{J+2} \\
c_2 BD_{-J+1} & -2c_2 ED_{-J+1} & c_1 BD_{J+2} & -2c_1 ED_{J+2} \\
-2c_2 \bar{\Delta} D_{-J+1} & c_2 AD_{-J+1} & -2c_1 \bar{\Delta} D_{J+2} & c_1 AD_{J+2} \\
-\frac{\partial_{J-1}^2}{2J+1} - \bar{E}_1 \bar{E}_2 & m_1 \bar{E}_2 - m_2 \bar{E}_1 & -2c_1 c_2 H_2 & 0 \\
m_1 \bar{E}_2 - m_2 \bar{E}_1 & \frac{\partial_{J-1}^2}{2J+1} - \bar{E}_1 \bar{E}_2 & 0 & 2c_1 c_2 H_2 \\
-2c_1 c_2 H_1 & 0 & \frac{\partial_{J+1}^2}{2J+1} - \bar{E}_1 \bar{E}_2 & m_1 \bar{E}_2 - m_2 \bar{E}_1 \\
0 & 2c_1 c_2 H_1 & m_1 \bar{E}_2 - m_2 \bar{E}_1 & -\frac{\partial_{J+1}^2}{2J+1} - \bar{E}_1 \bar{E}_2
\end{array} \right), \tag{2.C.89}$$

where $\bar{E}_1 = E_1 + i\partial_t$, $\bar{E}_2 = E_2 - i\partial_t$ and $2\bar{\Delta} = \bar{E}_1 - \bar{E}_2$. The c_i , A, B and H_i are defined in Appendix 2.A. The matrix \mathbf{S}^{-1*} of S^{-1} for the set \mathcal{B}^* (2.A.54) of natural parity states can be obtained from \mathbf{S}^{-1} by changing $E_2 \rightarrow -E_2$. The complete partial wave projected BSE becomes the following set of eight coupled partial-differential equations

$$\mathbf{S}^{-1}(t, x)\boldsymbol{\psi}(t, x) = -\mathbf{V}(t, x)\boldsymbol{\psi}(t, x). \tag{2.C.90}$$

Chapter 3

Effects of negative energy components

Relativistic covariance requires that in the constituent quark model for mesons the positive energy states as well as the negative energy states are included. Using relativistic quasipotential equations the contribution of the negative energy states is studied for the light and charmonium mesons. It is found that these states change the meson mass spectrum significantly but leave its global structure untouched. This Chapter has been published as Ref. [71].

3.1 Introduction

The application of the constituent quark model to mesons and baryons has been very successful, in spite of various nonrelativistic approximations. How much is neglected in these approximations? Generalization of the ordinary Schrödinger equation to a relativistic covariant form results in the well-known Bethe-Salpeter equation (BSE), which differs from the nonrelativistic equation in two respects. First, the dependence of the bound state wave function on the relative three-momentum \mathbf{p} becomes a dependence on the four-momentum (p_0, \mathbf{p}) . Second, covariance requires that for fermions the full Dirac structure is taken into account, so for quarks not only the positive energy states are to be considered, but also their negative energy states must be included. In this Chapter we investigate the effect on the meson mass spectrum of the inclusion of these negative energy states in the relativistic constituent quark model.

Quasipotential (QP) approximations to the BSE exist which eliminate the p_0 dependence of the quark propagators, and moreover circumvent the problem of introducing a confining potential in the full Minkowski space. The covariant Dirac structure is kept in these. In Chapter 2 we used two QP models to calculate the full meson mass spectrum. One of the biggest differences found with the Schrödinger

approach was the much stronger confinement needed and the sensitivity of the mass spectrum to small vector contributions to the confining potential. To get some more insight about the various aspects we have performed calculations in the same framework but with leaving out various negative energy states. This enables us to trace back and understand the origin of the phenomena found in Chapter 2 and to establish the importance of the negative energy states. For simplicity the calculations are restricted to the equal mass case.

In the next Section the model is briefly summarized and some of the QP equations properties which give upper bounds on the parameters of the potential are discussed. Section 3.3 deals with the truncation of the relativistic QP equations in the coordinate representation with regards to the negative energy spinor states. It also presents the comparison of the calculations with corresponding nonrelativistic predictions. In particular the $u\bar{u}$ and $c\bar{c}$ spectra are considered in various approximations to various QP models. Differences in the spectra are discussed. Finally, the Chapter closes with some concluding remarks.

3.2 Review of model

We briefly describe the relativistic constituent quark model of Chapter 2. The model consists of two pointlike fermions bound together by a phenomenological potential V to form a meson. The meson wave function ψ satisfies

$$S^{-1}(\mathbf{p})\psi(\mathbf{p}) = - \int \frac{d\mathbf{q}}{(2\pi)^3} V(\mathbf{p} - \mathbf{q})\psi(\mathbf{q}). \quad (3.2.1)$$

The dependence of the propagator S on the relative four-momentum (p_0, \mathbf{p}) has been simplified to a dependence on the three-momentum. In Chapter 2 we studied two QP approximations which eliminate the dependence of the equation on p_0 : the Blankenbecler-Sugar-Logunov-Tavkhelidze (BSLT) approximation [9, 17], and an equal-time (ET) approximation [56, 73, 74]. They give for quarks of equal mass in the center of mass system

$$S_{\text{BSLT}}^{-1}(\mathbf{p}) = 4\omega \left[\frac{\omega - E}{\omega + E} \Lambda^{++} - \Lambda^{+-} - \Lambda^{-+} + \frac{\omega + E}{\omega - E} \Lambda^{--} \right], \quad (3.2.2)$$

and

$$S_{\text{ET}}^{-1}(\mathbf{p}) = 2(\omega - E)\Lambda^{++} - 2\omega(\Lambda^{+-} + \Lambda^{-+}) + 2(\omega + E)\Lambda^{--}, \quad (3.2.3)$$

where $\omega = \sqrt{\mathbf{p}^2 + m^2}$, and $E = M/2$, M being the total meson mass. The $\Lambda^{\rho_1\rho_2}$ project upon positive and negative energy states, $\Lambda^{\rho_1\rho_2} = \Lambda_1^{\rho_1}(\mathbf{p})\Lambda_2^{\rho_2}(-\mathbf{p})$ with

$$\Lambda_i^{\rho_i}(\mathbf{p}) = \frac{\rho_i(\boldsymbol{\gamma}^{(i)} \cdot \mathbf{p} + m_i) + \omega_i \gamma_0^{(i)}}{2\omega_i}. \quad (3.2.4)$$

Let us define the eigenstates of these projection operators by

$$\Lambda^{\rho_1\rho_2}\gamma_0^{(1)}\gamma_0^{(2)}|\rho_1\rho_2\rangle_{\text{pw}} = |\rho_1\rho_2\rangle_{\text{pw}}. \quad (3.2.5)$$

The subscript pw is used to distinguish these plane wave states from the canonical positive and negative states defined through

$$\gamma_0^{(1)}\gamma_0^{(2)}|\rho_1\rho_2\rangle_{\text{ca}} = \rho_1\rho_2|\rho_1\rho_2\rangle_{\text{ca}}, \quad (3.2.6)$$

which correspond to the various combinations of upper and lower components of the Dirac spinors. Clearly

$$|\rho_1\rho_2\rangle_{\text{pw}} = |\rho_1\rho_2\rangle_{\text{ca}} + \mathcal{O}(p/m). \quad (3.2.7)$$

The instantaneous interaction V between the quarks is modeled as the sum of a Coulomb-like part describing the one-gluon-exchange (OGE) interaction and a linearly rising part for the confinement. It takes in coordinate space the form

$$V(x) = -\frac{\alpha(x)}{x}\Gamma_V + (\kappa x + c) \left[(1 - \varepsilon)\mathbf{1}^{(1)}\mathbf{1}^{(2)} + \varepsilon\Gamma_V \right]. \quad (3.2.8)$$

The vector contribution to the interaction is studied in the Feynman gauge as well as in the Coulomb gauge:

$$\Gamma_V^{\text{Feynman}} = \gamma_\mu^{(1)}\gamma^{\mu(2)}, \quad (3.2.9)$$

$$\Gamma_V^{\text{Coulomb}} = \gamma_\mu^{(1)}\gamma^{\mu(2)} + \frac{1}{2} \left[\boldsymbol{\gamma}^{(1)} \cdot \boldsymbol{\gamma}^{(2)} - (\boldsymbol{\gamma}^{(1)} \cdot \hat{\boldsymbol{x}})(\boldsymbol{\gamma}^{(2)} \cdot \hat{\boldsymbol{x}}) \right]. \quad (3.2.10)$$

This defines the relativistic quasipotential model. Note that we do allow for a fraction ε of vector-confinement. The running coupling constant behaves as $\alpha(x) \sim (8/27)\pi/\ln(x_0/x)$ for small distances x , and grows to some maximum saturation value α_{sat} for large separations, according to the interpolation given in Chapter 2.

The resulting wave equation were studied extensively in coordinate space. It should be noted that certain difficulties as found in the one-particle Dirac equation should be expected in such a relativistic quasipotential approach. Let us for a moment consider one fermion in an external potential. If this particle experiences a potential which fluctuates more strongly than $\sim 2m$ over a distance shorter than its Compton length $x_C = 1/m$ new fermion-antifermion pairs can be created. This phenomenon cannot correctly be described by the Dirac equation which describes a one-particle theory and thus misses the interactions between the newly created pair and the starting particle. Since the Dirac equation does allow for antifermion components, solutions in this potential can have an unbound number of non-interacting fermions and antifermions thus being unnormalizable and unphysical. This break-down of the

Dirac equation is well-known as the Klein paradox [8]. Similar flaws emerge in the QP equations of this work since they also contain negative energy components. In view of the complexity of the various two-body equations we do not fully analyze under what conditions they break down. Instead, let us note that unbound solutions can be expected if the confining strength becomes too strong, $\kappa x_C \gtrsim 2m$ or $\kappa \gtrsim 2m^2$. This domain can be reached in light meson systems. The condition on κ depends on the fraction ε of vector confinement as indicated by the discussion in Chapter 2. Similarly, if the OGE potential becomes too strong, $\alpha/x_C \gtrsim 2m$ or $\alpha \gtrsim 2$, irregular solutions may be expected. Mesons with high orbital angular momenta are less sensitive to this effect because the centrifugal barrier prevents them from entering the short distance region. If a running coupling constant is taken instead of a fixed one then the irregular solutions disappear and the singular behavior becomes less. Whereas the upper bound on κ disappears as the negative energy components are removed, the upper bound on α is shifted upward but still present, reflecting that only positive energy states can also tumble in a OGE potential. Detailed discussions on the short distance behavior were given in the appendix of Chapter 2.

3.3 Results

Since the wave equations as described in the previous Section are solved in the coordinate space using the representation of the canonical states Eq. (3.2.6), a convenient way to switch off the coupling to the negative energy plane wave states is to explicitly project out these states in the interaction. The projection is done by rewriting the BSLT equation as

$$\begin{aligned} & [(\omega - E)\Lambda^{++} - E(\Lambda^{+-} + \Lambda^{-+}) - (i_{bb}\omega + E)\Lambda^{--}] \psi = \\ & -\frac{1}{4\omega} [(\omega + E)\Lambda^{++} + i_b E(\Lambda^{+-} + \Lambda^{-+}) + i_{bb}(E - \omega)\Lambda^{--}] \gamma_0^{(1)} \gamma_0^{(2)} V \psi. \end{aligned} \quad (3.3.11)$$

For $i_b = i_{bb} = 1$ we recover the BSLT equation with all negative energy states included. If i_b is put to zero, then the single negative energy states are projected to zero, provided $E \neq 0$, and similarly for i_{bb} when we want to drop the coupling to the $|--\rangle_{\text{pw}}$ states in the calculations. One can rewrite the ET equation in a similar way:

$$\begin{aligned} & 2 [(\omega - E)\Lambda^{++} - \omega(\Lambda^{+-} + \Lambda^{-+}) + (i_{bb}\omega + E)\Lambda^{--}] \psi = \\ & - [\Lambda^{++} + i_b(\Lambda^{+-} + \Lambda^{-+}) + i_{bb}\Lambda^{--}] \gamma_0^{(1)} \gamma_0^{(2)} V \psi. \end{aligned} \quad (3.3.12)$$

Although the number of coupled channels does not change, the above Eqs. (3.3.11) and (3.3.12) have as a major advantage that they can be solved in the same way as the full BSLT and ET equations were solved in Chapter 2. First we Fourier transform

Table 3.1: Parameters of the BSLT-Coulomb $q\bar{q}$ model.

	$u\bar{u}$	$c\bar{c}$	
m	0.250	1.779	GeV
κ	0.33	0.33	GeV ²
c	-1.0	-1.0	GeV
ε	0.25	0.25	
$\alpha_{\text{sat}}^{\text{a}}$	0.8	0.8	
β_1	0.25	0.8	GeV
β_2	0.10	0.6	GeV

^a Running according to Eq. (2.3.39) with $\mu = 1.0$ GeV.

them to configuration space and make an angular momentum decomposition. This gives a set of coupled integral-differential equations which are reduced to a set of linear equations by expanding the wave function on a set of spline functions. The resulting matrix equation for the various spline coefficients can be solved straightforwardly by standard methods. As a check on the accuracy of our calculational procedures we used this method to calculate the charmonium mass spectrum in the model of Hirano *et al.* [58], which includes only the $|++\rangle_{\text{pw}}$ and $|--\rangle_{\text{pw}}$ states. Agreement was found within 1 MeV.

3.3.1 Comparison with Schrödinger equation results

To study the effects of various relativistic contributions we consider the mass spectra for the light mesons and the charmonium system. In the limit of large quark masses the BSLT can be reduced to the nonrelativistic Schrödinger equation

$$\left[2 \left(-\frac{\nabla^2}{2m} + m \right) + V_{\text{NR}}(x) + V_{\text{SD}}(x) \right] \psi(x) = M\psi(x), \quad (3.3.13)$$

where V_{NR} is the nonrelativistic reduction of the potential,

$$V_{\text{NR}}(x) = -\frac{\alpha(x)}{x} + \kappa x + c, \quad (3.3.14)$$

and V_{SD} contains the spin-dependent corrections of order $1/m^2$ [52],

$$\begin{aligned} V_{\text{SD}}(x) &= \frac{1}{m^2} \left[\frac{3V'_V - V'_S}{2x} \mathbf{L} \cdot \mathbf{S} + \frac{2}{3} (\nabla^2 V_V) \mathbf{S}_1 \cdot \mathbf{S}_2 + \left(\frac{1}{x} V'_V - V''_V \right) S_{12} \right], \\ S_{12} &= (\mathbf{S}_1 \cdot \hat{\mathbf{x}})(\mathbf{S}_2 \cdot \hat{\mathbf{x}}) - \frac{1}{3} \mathbf{S}_1 \cdot \mathbf{S}_2. \end{aligned} \quad (3.3.15)$$

Here V_V and V_S denote the vector and scalar contributions to the potential. The potential in Eq. (3.3.15) is singular at the origin, and therefore a regularization is needed. The delta function appearing in $\nabla^2 V_V$ is replaced by a Gaussian of width β_1^{-1} , and the x^{-1} and x^{-3} singularities are cut off at $x_0 = \beta_2^{-1}$ and replaced by smoothly fitting Gaussians. We take the same parameters for the potential as in Chapter 2, which are summarized in Table 3.1, and take the β_i such that they reproduce approximately the same splittings between the S - and P -states as the full BSLT calculation. With these parameters we find the spectra as shown in the first column of Figs. 3.1 and 3.2 of the $u\bar{u}$ and $c\bar{c}$ systems. The spectra of the various columns in these figures will be referred to as Fig. 3.1(a), 3.1(b), etc.

The first natural step in relativizing the Schrödinger equation is to replace the kinetic energy according to

$$\frac{\mathbf{p}^2}{2m} + m \rightarrow \omega = \sqrt{\mathbf{p}^2 + m^2} \quad (3.3.16)$$

in Eq. (3.3.13). Figures 3.1(b) and 3.2(b) show the corresponding spectra. They are shifted downwards as compared to the nonrelativistic ones, indicating that the interaction has become more attractive. Also the shift becomes larger as the level of excitation increases. For charmonium one finds shifts between 0.05 and 0.13 GeV, whereas for the light mesons these shifts are more substantial and range between 0.5 and 1.5 GeV. The second relativistic correction which can be included is to replace the approximation of the potential $V_{NR} + V_{SD}$ by the complete projection of the potential Eq. (3.2.8) on positive energy states $V^{++,++} \equiv {}_{\text{pw}}\langle ++ | V \gamma_0^{(1)} \gamma_0^{(2)} | ++ \rangle_{\text{pw}}$. The singular behavior of V_{SD} is no longer present in the complete projection, and hence the cutoff parameters β_i are principally absent in the resulting wave equations. Note the factors $\gamma_0^{(1)} \gamma_0^{(2)}$ in $V^{++,++}$ and in the right hand sides of Eqs. (3.3.11) and (3.3.12) which reflect that the energies of the quarks are the fourth components of their four-momenta. This replacement gives a rather large effect (0.00 – 0.16 GeV for cc and 0.0 – 0.8 GeV for $u\bar{u}$) as is illustrated by the spectra in Fig. 3.1(c) and 3.2(c) and which is easily understood. For a potential $V(x) = V_S(x)\mathbf{I} + V_V(x)\gamma_0^{(1)}\gamma_0^{(2)}$ and low momenta of the in- and outgoing states

$$V^{++,++} \approx {}_{\text{ca}}\langle ++ | V_S \gamma_0^{(1)} \gamma_0^{(2)} + V_V(x)\mathbf{I} | ++ \rangle_{\text{ca}} = V_S(x) + V_V(x). \quad (3.3.17)$$

But for relativistic momenta considerable contributions to $V^{++,++}$ are to be expected from the contributions

$${}_{\text{ca}}\langle -+ | V_S \gamma_0^{(1)} \gamma_0^{(2)} + V_V(x)\mathbf{I} | -+ \rangle_{\text{ca}} = -V_S(x) + V_V(x). \quad (3.3.18)$$

For scalar confinement it leads to a considerable reduction of the strength of the confinement. This effect can also qualitatively be seen from the spin-independent

corrections of order $1/m^2$ [52] to a nonrelativistic scalar potential. It is given by

$$V_{\text{SI}}(x) = \frac{1}{m^2} \left[\frac{1}{4}(\nabla^2 V_S) + V_S' \frac{d}{dx} + V_S \nabla^2 \right]. \quad (3.3.19)$$

This potential, however, does not give an accurate approximation since for large distances $m^{-2}V_S \nabla^2$ is not a small enough parameter to expand in.

To obtain the explicit form of the BSLT propagator we may replace

$$(\omega - E) \rightarrow \frac{2\omega}{\omega + E}(\omega - E). \quad (3.3.20)$$

This leads to the BSLT equation restricted to only positive energy states. Figures 3.1(d) and 3.2(d) show how the masses are increased.

Figure 3.1(e) shows the effect of the introduction of the single negative energy states $|+-\rangle_{\text{pw}}$ and $|-+\rangle_{\text{pw}}$. For the light mesons we do not show this case since for some mesons it leads to unbound systems, similar to the Klein paradox mentioned in the previous Section. The introduction of these states leads to an increase of the cc spectrum by up to 0.10 GeV. They are mostly made out of $|+-\rangle_{\text{ca}}$ and $|-+\rangle_{\text{ca}}$ states which have a negative expectation value of scalar confinements, Eq. (3.3.18). Together with the negative propagation of these states this leads to a positive interaction which raises the mass levels.

Finally, if the $|--\rangle_{\text{pw}}$ states are included, one arrives at the full BSLT spectra shown in Figs. 3.1(f) and 3.2(e). The inclusion of these states changes little ($\lesssim 1$ MeV for $c\bar{c}$), as could be expected from their smallness. The lowest-lying mesons, however, are considerably influenced by what is related to the singular behavior of the wave function at small distances. The OGE potential concentrates the wave function to small distances with strong potential, thus lowering the mass levels. The singular behavior becomes stronger if more negative energy states are included or if the level of excitation is less. Figure 3.1(g) shows the charmonium spectrum in the Salpeter approximation, which includes only the $|++\rangle_{\text{pw}}$ and $|--\rangle_{\text{pw}}$ states. The small masses for the low-lying excitations are still present, but the increase associated with the single negative states is absent.

3.3.2 Equal-time results

Let us briefly discuss what effects are found if we use the equal-time (ET) propagator. In Fig. 3.3 is shown the corresponding charmonium spectrum calculated with the same parameters as Fig. 3.1. Three differences can be noted. First, the ET spectrum is lowered as compared to the BSLT one. This is a consequence of the different propagators for the $|++\rangle_{\text{pw}}$ states [cf. Eq. (3.3.20)]. Second, the introduction of the single negative energy states causes a shift upwards in the ET model which is

approximately twice that seen in BSLT. This is due to the fact that these states are roughly twice as important in the ET wave function as in the BSLT one in view of a twice as large propagator for these states, $S_{\text{ET}}^{++} = -1/2\omega$ versus $S_{\text{BSLT}}^{++} = -1/4\omega$. Third, the $|--\rangle_{\text{pw}}$ energy states lower the singlet states much more strongly in the ET model than in BSLT. Again, this is a consequence of the importance of these states in the ET wave function. They are larger due to the large S_{ET}^{--} propagator. As already remarked in [73], this is a defect of the ET equation when an unretarded potential is used, and this disappears if the proper retardation is inserted in the matrix elements for V that connect to double negative energy states. However, it should be stressed that there is no unambiguous extension of the instantaneous confining potential to retarded times.

3.3.3 Sensitivity to vector confinement

In Chapter 2 we discussed the large raising of the light meson spectrum when a part of vector confinement is added to a scalar confining potential. Figure 3.4 shows the uu spectrum for various dynamical models using scalar confinement without and with a vector contribution. As can be seen from the figure, when only positive energy states are taken the raising of the energy levels decreases for a given amount of vector confinement. As a result a larger string tension would be needed to get the same Regge-slope as found in a full calculation.

In Fig. 3.4 is also shown the same spectrum if the vector contribution is taken in the Feynman gauge, Eq. (3.2.9). In this gauge the spin-spin interaction is less suppressed so the vector contribution has more effect.

3.4 Concluding remarks

In summary, we have calculated for the light and charmonium systems mass spectra using the (relativized) Schrödinger equation and the relativistic quasipotential equations of Chapter 2, which differ from the Schrödinger approach in that no $1/m^2$ approximation is made, and that the QP equations contain the full Dirac structure of positive and negative energy states. We studied the importance of these differences by solving the QP equations while leaving out negative energy components. We find that the projection of the confining potential on positive energy states leads to a considerably lower confinement strength than the nonrelativistic potential gives. This is partly compensated for by the introduction of the single negative energy states which are more bound than the positive states, and hence increase the masses. Finally we find that the double negative energy states have little influence except for short distances where the singular behavior of the mesons is strengthened.

The total picture strongly suggests that the differences here studied are important for determining the parameters of the $q\bar{q}$ interaction, especially the confine-

ment strength κ . Yet the global structure of the spectrum —level ordering, relative sizes of splittings— remains rather untouched under the relativistic modifications. This confirms the conclusion drawn from the success of nonrelativistic quark models that most relativistic effects in $q\bar{q}$ spectroscopy can be mimicked by employing nonrelativistic dynamics together with effective parameters. It will be interesting to study whether the relativistic modifications to meson wave functions will lead to sizable changes in cross section for processes involving these mesons. This is examined in Chapter 4.

In this Chapter we have studied relativistic effects within the framework of quasipotential equations. In so doing we have not addressed entirely the role of the relative energy variable p_0 . Apart from the complexity of a calculation including this say in a Bethe-Salpeter equation approach, a more fundamental obstacle is posed by the extension of the definition of the confining potential, as we have used here, to a four-momentum dependence. The confining potential is only known for the static case. There is at this moment no underlying theory which can give a prescription on how to extend it to a covariant form. Let us illustrate this by considering the commonly used generalization of the potential $V(x) = \kappa x$ which reads in momentum space

$$V(q_0, \mathbf{q}) = \frac{\kappa}{2\pi^2} \lim_{\eta \rightarrow 0} \left[\frac{\partial^2}{\partial \eta^2} \frac{1}{\mathbf{q}^2 - q_0^2 + \eta^2(1 - i\varepsilon)} \right], \quad (3.4.21)$$

but its Fourier transform yields

$$V(t, x) = \frac{\kappa}{\pi} \lim_{\eta \rightarrow 0} [K_0(\eta R) - \eta R K_1(\eta R)] = \infty \quad (3.4.22)$$

(with $R^2 = x^2 - t^2$), which is clearly physically unacceptable. Exploring QCD may lead to ways of reconstructing such a confining force, which can be used in such an off mass shell approach as we have discussed here.

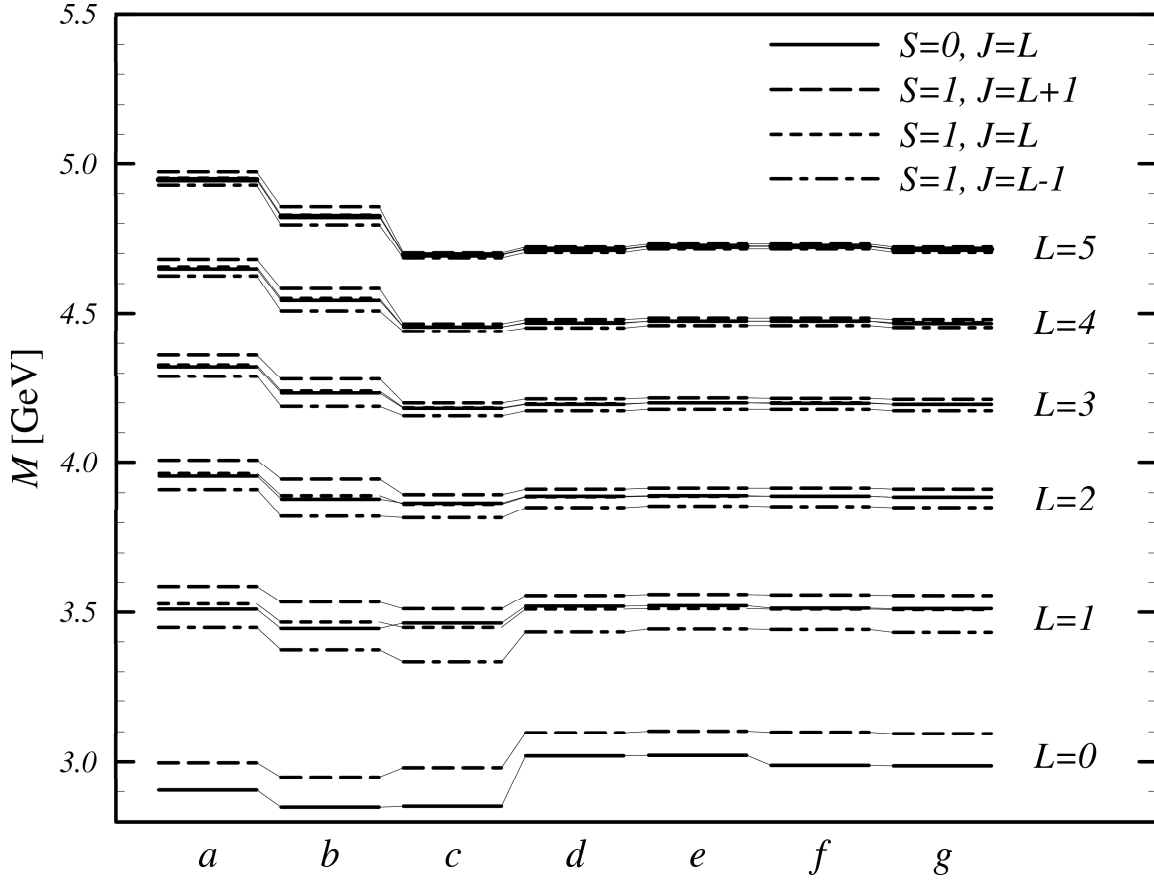


Figure 3.1: Charmonium spectrum of the radially unexcited states. (a) Schrödinger equation with $p^2/2m$ and Breit interaction, (b) Schrödinger equation with $\sqrt{p^2 + m^2}$ and Breit interaction, (c) Schrödinger equation with $\sqrt{p^2 + m^2}$ and full projection of potential in Coulomb-gauge, i.e. FT with $|++\rangle_{\text{pw}}$, (d) BSLT with $|++\rangle_{\text{pw}}$, (e) BSLT with $|++\rangle_{\text{pw}}$, $|+-\rangle_{\text{pw}}$ and $| - + \rangle_{\text{pw}}$, (f) BSLT with all states, (g) BSLT with $|++\rangle_{\text{pw}}$ and $|--\rangle_{\text{pw}}$.

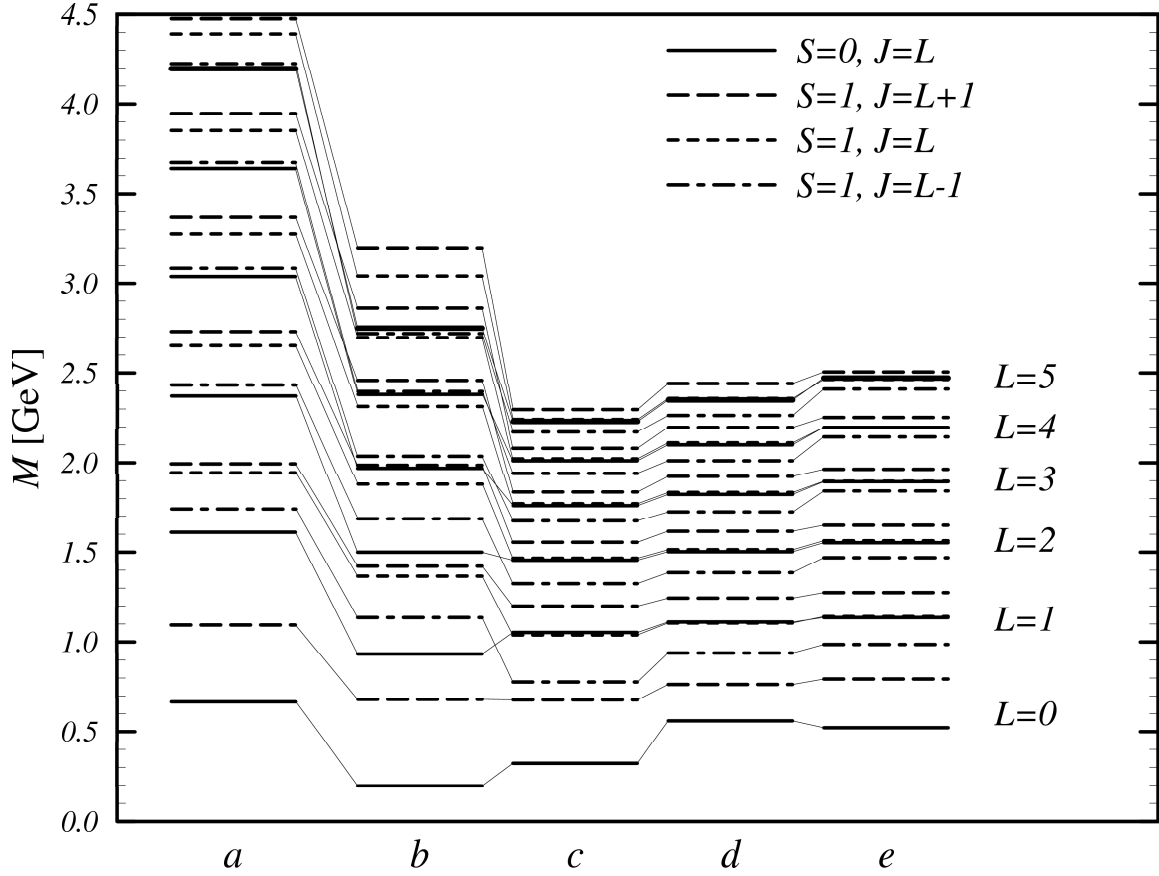


Figure 3.2: Light meson spectrum of the radially unexcited states. (a) Schrödinger equation with $p^2/2m$ and Breit interaction, (b) Schrödinger equation with $\sqrt{p^2 + m^2}$ and Breit interaction, (c) Schrödinger equation with $\sqrt{p^2 + m^2}$ and full projection of potential in Coulomb-gauge, i.e. $E1\Gamma$ with $|++\rangle_{\text{pw}}$, (d) BSLT with $|++\rangle_{\text{pw}}$, (e) BSLT with all states.

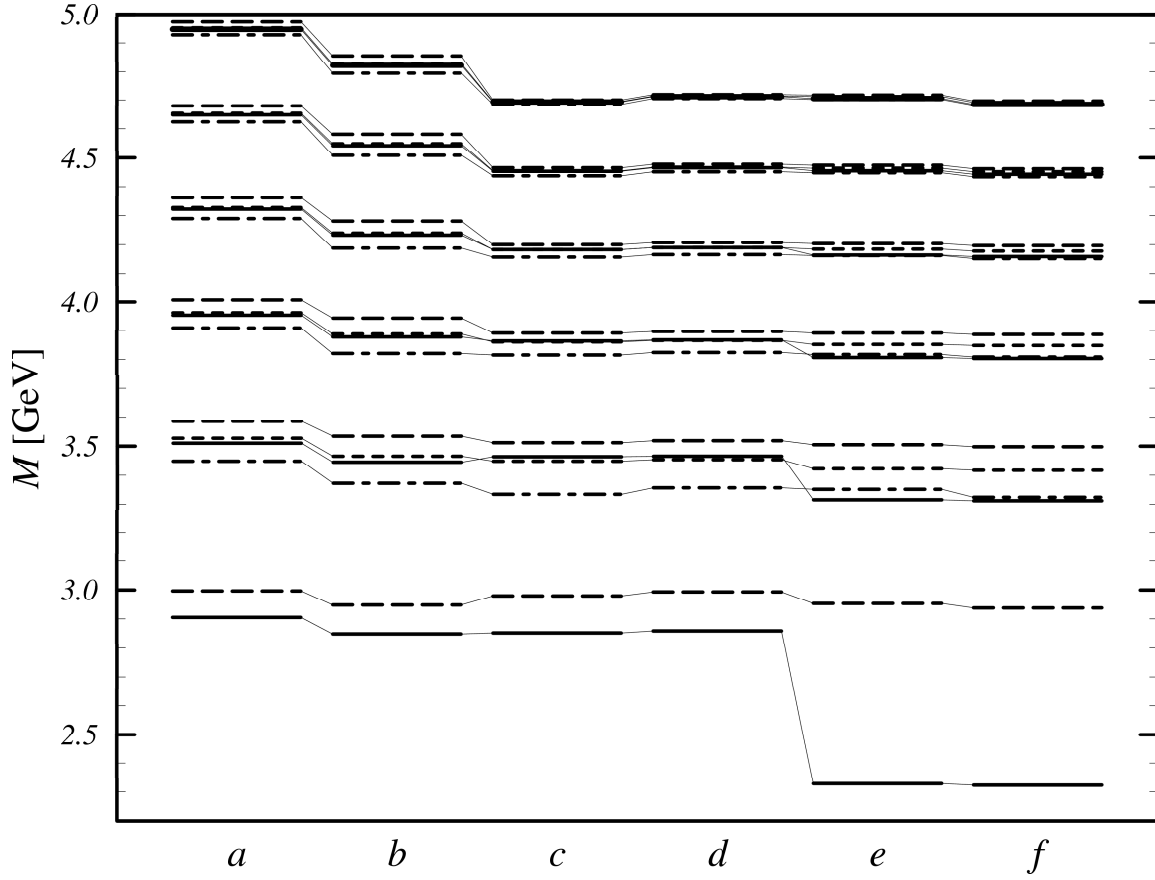


Figure 3.3: Charmonium spectrum of the radially unexcited states (legend as in Fig. 3.1). (a) Schrödinger equation with $p^2/2m$ and Breit interaction, (b) Schrödinger equation with $\sqrt{p^2 + m^2}$ and Breit interaction, (c) Schrödinger equation with $\sqrt{p^2 + m^2}$ and full projection of potential, i.e. ET with $|++\rangle_{\text{pw}}$, (d) ET with $|++\rangle_{\text{pw}}$, $|+-\rangle_{\text{pw}}$ and $| - + \rangle_{\text{pw}}$, (e) ET with all states, (f) ET with $|++\rangle_{\text{pw}}$ and $|--\rangle_{\text{pw}}$.

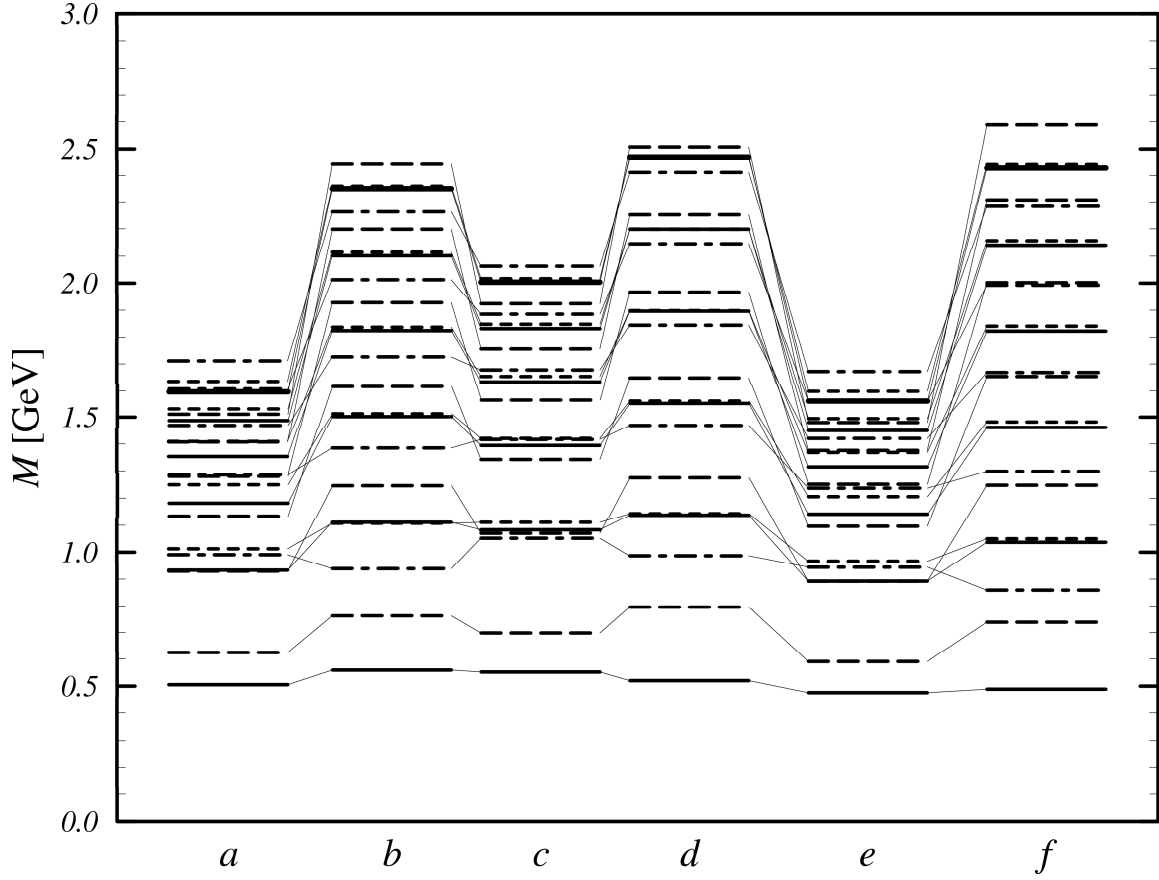


Figure 3.4: Light meson spectrum of the radially unexcited states (legend as in Fig. 3.1). (a) BSLT in Coulomb gauge with $|++\rangle_{\text{pw}}$ and $\varepsilon = 0$, (b) BSLT in Coulomb gauge with $|++\rangle_{\text{pw}}$ and $\varepsilon = 0.25$, (c) BSLT in Coulomb gauge with all states and $\varepsilon = 0$, (d) BSLT in Coulomb gauge with all states and $\varepsilon = 0.25$, (e) BSLT in Feynman gauge with $|++\rangle_{\text{pw}}$ and $\varepsilon = 0$, (f) BSLT in Feynman gauge with $|++\rangle_{\text{pw}}$ and $\varepsilon = 0.25$.

Chapter 4

Reactions

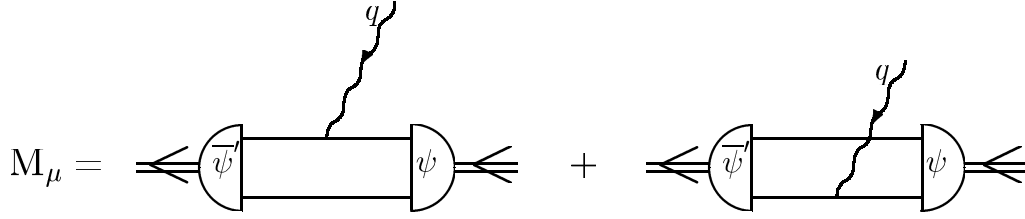
The relativistic constituent quark model is used to study radiative transitions, electromagnetic form factors and annihilation decay of mesons. We show how the divergence of the meson wave function at small distances, which troubles relativistic calculations of annihilation decay, can be renormalized in configuration space. The divergence can give a pion form factor with the same large tail for large momenta as asymptotic QCD models predict. We pay special attention to the connection between the nonrelativistic and the relativistic reaction probabilities and to the influence of the various relativistic ingredients of the model. It is observed that in a consistent treatment of the meson dynamics and the meson interaction the relativistic effects in the meson masses partly compensate for the effects in the interaction, thus leading to only modest adjustments of reaction probabilities. Part of Section 4.3 has been published in [69].

4.1 Meson current

Before formulating the expression for the meson current in the quasipotential (QP) model, we take a brief look at this expression in the framework of the Bethe-Salpeter equation (BSE); it nicely illustrates some properties of the current that can be used as a guideline for constructing the QP current.

4.1.1 Bethe-Salpeter current

The electromagnetic current J_μ of the meson is proportional to the amplitude M_μ for the photon-meson interaction. Assuming that the meson-photon coupling takes place through the possible couplings of the photon to individual pointlike quarks, one can

Figure 4.1: Contributions to the photon-meson amplitude M_μ .

write down for the electromagnetic current [6]

$$\begin{aligned}
 J_\mu &= \frac{1}{2\sqrt{\omega_{P'}\omega_P}} M_\mu, \\
 M_\mu &= -i \int \frac{d^4p}{(2\pi)^4} \left[e_A \bar{\psi}'(P', p + \beta q) \Gamma_\mu^A \psi(P, p) + e_B \bar{\psi}'(P', p - \alpha q) \Gamma_\mu^B \psi(P, p) \right]
 \end{aligned}
 \tag{4.1.1}$$

where unprimed variables refer to the initial meson, primed variables refer to the final meson, $P' = P + q$, $\omega_P = \sqrt{M^2 + \mathbf{P}^2}$, ψ and ψ' are the wave functions of the mesons, q is the photon momentum. The quark momenta are defined in Chapter 2 and the e_i are the charges of quark A and B . Note that the subscripts A and B have the same meaning as the subscripts (1) and (2) used in the previous Chapters. The vertices $\Gamma^{(i)}$ are given by

$$\Gamma_\mu^A = \gamma_\mu^A S_B^{-1}(p_B) \quad \text{and} \quad \Gamma_\mu^B = S_A^{-1}(p_A) \gamma_\mu^B,
 \tag{4.1.2}$$

with the one-body propagators $S_i(p_i) = (\not{p}_i - m_i)^{-1}$. This matrix element is diagrammatically illustrated in Fig. 4.1. We introduce a short-hand notation $\langle \Gamma^{(i)} \rangle$ for the evaluation of the vertices $\Gamma^{(i)}$ between the initial and final state. Eq. (4.1.1) can then be written as

$$M_\mu = e_A \langle \Gamma_\mu^A \rangle + e_B \langle \Gamma_\mu^B \rangle.
 \tag{4.1.3}$$

If the two quarks have equal masses, one can use the charge exchange symmetry of the meson wave functions to simplify M_μ to

$$M_\mu = (e_A + \eta'_C \eta_C e_B) \langle \Gamma_\mu^A \rangle
 \tag{4.1.4}$$

where the $\eta_C = \pm 1$ are the charge-parity eigenvalues of the meson wave functions, as listed e.g. in Table 2.3.

A normalization condition for the wave function ψ can be found from the condition that the zeroth component of the current for a zero momentum photon should be equal to the meson charge. This leads to

$$\begin{aligned} e_A + e_B &= \frac{1}{2\omega_P} \langle e_A \Gamma_0^A + e_B \Gamma_0^B \rangle \\ &= -\frac{i}{2\omega_P} \int \frac{d^4 p}{(2\pi)^4} \left[\bar{\psi}(P, p) \left\{ e_A \Gamma_0^A + e_B \Gamma_0^B \right\} \psi(P, p) \right]. \end{aligned} \quad (4.1.5)$$

Another normalization for ψ can be derived from the full two-body propagator for the two-quark system. This propagator has poles in the total momentum P when P^2 equals a possible bound state mass squared. The residues at these poles correspond to the bound state wave functions. From the normalization of the two-body propagator S_{AB} one can thus find a normalization condition [54]

$$1 = \frac{1}{2\omega_P} \int \frac{d^4 p'}{(2\pi)^4} \frac{d^4 p}{(2\pi)^4} \left[\bar{\psi}(P, p') \left\{ \frac{\partial}{\partial P_0} S_{AB}^{-1}(P, p', p) \right\} \psi(P, p) \right]. \quad (4.1.6)$$

The inhomogeneous Bethe-Salpeter equation expresses the inverse two-body propagator as

$$S_{AB}^{-1}(P, p', p) = S_A^{-1}(p_A) S_B^{-1}(p_B) (2\pi)^4 \delta^4(p' - p) - V(P, p', p). \quad (4.1.7)$$

In the ladder approximation the potential V is independent of the total momentum P and Eq. (4.1.6) simplifies to

$$1 = -\frac{i}{2\omega_P} \int \frac{d^4 p}{(2\pi)^4} \left[\bar{\psi}(P, p) \left\{ \frac{\partial}{\partial P_0} S_A^{-1}(p_A) S_B^{-1}(p_B) \right\} \psi(P, p) \right], \quad (4.1.8)$$

which is equivalent to the charge normalization of Eq. (4.1.5). (The differentiation with respect to P_0 should be performed with some care, especially in the case of unequal mass particles, since not all momenta are independent variables; this is discussed in Ref. [6], which also gives a proof of the consistency of the two normalization schemes for general propagators and potential.) It is instructive to consider the expressions in curly brackets in Eqs. (4.1.5) and (4.1.8) and express them for the equal mass and charge case and zero relative energy difference ($p_0 = 0$) in terms of positive and negative energy states

$$\Gamma_{\text{norm}} = \frac{1}{2}(\Gamma_0^A + \Gamma_0^B) = (E - \omega)\Lambda^{++} + E(\Lambda^{+-} + \Lambda^{-+}) + (E + \omega)\Lambda^{--}, \quad (4.1.9)$$

where $\omega = \sqrt{m^2 + \mathbf{p}^2}$, $E = M/2$, and the projection operators are as defined in Chapter 2. In this form the distinguished roles for the various energy states are clearly shown.

In most applications, one has only solved the wave function in the center of mass system (cm), i.e. for $P = P_{\text{cm}} = (M, \mathbf{0})$. Since the BSE is Lorentz invariant, the wave function at $P \neq P_{\text{cm}}$ can directly be found from [76]

$$\psi(P, p) = \Lambda(\mathcal{L})\psi(\mathcal{L}^{-1}P, \mathcal{L}^{-1}p), \quad (4.1.10)$$

where \mathcal{L} is a Lorentz transformation such that $\mathcal{L}^{-1}P = P_{\text{cm}}$ and $\Lambda(\mathcal{L})$ describes the associated boost of the spin coordinates

$$\Lambda(\mathcal{L}) = \prod_{i=A,B} \sqrt{\frac{\omega_P + M}{2\omega_P}} \left[1 + \gamma_0^{(i)} \frac{\boldsymbol{\gamma}^{(i)} \cdot \mathbf{P}}{\omega_P + M} \right]. \quad (4.1.11)$$

Hence the meson current can be expressed in terms of the cm wave functions as

$$J_\mu = -\frac{i}{2\sqrt{\omega_{P'}\omega_P}} \int \frac{d^4p}{(2\pi)^4} \left[e_A \bar{\psi}'(P'_{\text{cm}}, k') \Lambda^{-1}(\mathcal{L}') \Gamma_\mu^A \Lambda(\mathcal{L}) \psi(P_{\text{cm}}, k) \right. \\ \left. + e_B \bar{\psi}'(P'_{\text{cm}}, k'') \Lambda^{-1}(\mathcal{L}') \Gamma_\mu^B \Lambda(\mathcal{L}) \psi(P_{\text{cm}}, k) \right], \quad (4.1.12)$$

where the Lorentz boosts are defined through

$$P_{\text{cm}} = \mathcal{L}^{-1}P, \quad P'_{\text{cm}} = \mathcal{L}'^{-1}(P + q), \quad (4.1.13)$$

and the relative momenta by

$$k = \mathcal{L}^{-1}p, \quad k' = \mathcal{L}'^{-1}(p + \beta q), \quad k'' = \mathcal{L}'^{-1}(p - \alpha q). \quad (4.1.14)$$

4.1.2 Quasipotential current

Let us now turn to the quasipotential (QP) models. If we want to write down the current matrix element along the same lines as in the BSE two complications are encountered. The first one is due to the fact that the p_0 dependence has been eliminated from the BSE propagator by approximating it by the QP propagator. The two one-body propagators $S_A(p_A)S_B(p_B)$ have been merged into one effective propagator $S_{\text{QP}}(\mathbf{p})$. For the construction of M_μ in Eq. (4.1.1) one uses the inverse propagator of the spectator quark S_i^{-1} . However, in the QP model it is not clear how to extract an effective inverse one-quark propagator $S_{i,\text{eff}}^{-1}(p_i)$ from the effective two-body propagator for the analogous construction of M_μ ,

$$M_\mu^{\text{QP}} = e_A \langle \Gamma_\mu^{A,\text{eff}} \rangle + e_B \langle \Gamma_\mu^{B,\text{eff}} \rangle \\ = e_A \langle \gamma_\mu^A S_{B,\text{eff}}^{-1}(p_B) \rangle + e_B \langle S_{A,\text{eff}}^{-1}(p_A) \gamma_\mu^B \rangle. \quad (4.1.15)$$

A simple and appealing choice, used in Ref. [39], is $S_{\text{eff}}^{-1} = \Lambda^+ + \Lambda^- = \gamma_0$. With this choice

$$M_\mu^{\text{ID}} = e_A \langle \gamma_\mu^A \gamma_0^B \rangle + e_B \langle \gamma_0^A \gamma_\mu^B \rangle, \quad (4.1.16)$$

and the normalization vertex, analogous to Eq. (4.1.9), of the meson becomes

$$\Gamma_{\text{norm}}^{\text{ID}} = \Lambda^{++} + \Lambda^{+-} + \Lambda^{-+} + \Lambda^{--}. \quad (4.1.17)$$

We label this as the identity current (ID) since $\Gamma_{\text{norm}}^{\text{ID}}$ is essentially the identity. Notice that for mesons with large total mass and small kinetic energies, $\omega \ll E$, this ID vertex weighs the various energy states with ratios equal to those of the BSE vertex Eq. (4.1.9).

However, one may also follow Eq. (4.1.8) and impose

$$\Gamma_{\text{norm}}^{\text{QP}} = \frac{\partial}{\partial P_0} S_{\text{QP}}^{-1}(P, p). \quad (4.1.18)$$

For the ET propagator one then finds the simple form

$$\Gamma_{\text{norm}}^{\text{ET}} = -\Lambda^{++} + \Lambda^{--}, \quad (4.1.19)$$

where we assume equal quark masses for simplicity. This form is also found if the equal-time prescription, i.e. integration over p_0 , is applied to the BSE amplitude

$$\Gamma_{\text{norm}}^{\text{ET}} = S_{\text{ET}}^{-1} \left[\int \frac{dp_0}{2\pi i} S_A \gamma_A^0 S_A S_B + S_A S_B \gamma_B^0 S_B \right] S_{\text{ET}}^{-1}. \quad (4.1.20)$$

Again, notice that for mesons with small total mass and large kinetic energies, $\omega \gg E$, this ET vertex weighs the various energy states with ratios equal to those of the BSE vertex Eq. (4.1.9). This condition on Γ_0^{ET} is consistent with the choice

$$S_{\text{eff}}^{-1} = -\Lambda^+ + \Lambda^- = \frac{\boldsymbol{\gamma} \cdot \mathbf{p} + m}{\omega}, \quad (4.1.21)$$

leading to

$$\begin{aligned} J_\mu^{\text{ET}} &= \frac{1}{2\sqrt{\omega_P} \omega_P} M_\mu^{\text{ET}}, \\ M_\mu^{\text{ET}} &= e_A \langle \gamma_\mu^A \frac{\boldsymbol{\gamma}_B \cdot \mathbf{p}_B + m_B}{\omega_B} \rangle + e_B \langle \frac{\boldsymbol{\gamma}_A \cdot \mathbf{p}_A + m_A}{\omega_A} \gamma_\mu^B \rangle. \end{aligned} \quad (4.1.22)$$

For the BSLT propagator one can try a similar approach, but the vertex found in this way exhibits poles at $E = \pm\omega$ which is undesirable. It should be noted that Eq. (4.1.5) implies that the BSE vertices satisfy $\langle \Gamma_0^A \rangle = \langle \Gamma_0^B \rangle$ if the in- and

outgoing mesons are identical. This is not satisfied by the QP current operators if the quarks have unequal mass.

A second complication in the construction of the current matrix element is due to the fact that the QP wave functions are only well-defined for $k_0 = k'_0 = 0$. This means that the overlap integral of the current matrix element for quark A is only well-defined for relative momenta p satisfying both

$$p \cdot P = 0 \quad \text{and} \quad (p + \beta q) \cdot (P + q) = 0, \quad (4.1.23)$$

where the first condition puts $k_0 = 0$, the second condition puts $k'_0 = 0$. These conditions on p lead to an overlap integral that is only two-dimensional, which is undesirable. Reference [21] proposes to adjust the QP condition on k_0 such that the restrictions are equal for both meson velocities in the specific process studied. Advantages of this method are consistency and the yield of a conserved current. On the other hand, disadvantages are that the meson wave functions are not peaked at $k_0 = 0, k'_0 = 0$ and that one has to solve the bound state wave equations in a moving frame for each photon momentum. The latter involves much numerical effort.

Instead, we relax the condition that the relative energies should be zero to the assumption that the wave functions are independent of their relative energies k_0 and k'_0 (which holds in the ET scheme), and we evaluate the overlap integral in a three-dimensional subspace. The choice of this subspace is subtle and can influence the resulting currents. We choose to integrate over \mathbf{k} . The independence on k_0 gives the possibility to choose some special value for it. We choose k_0 such that

$$d^3 \mathbf{k} = d^3 \mathbf{k}', \quad (4.1.24)$$

so that the current remains invariant under time reversal. These momenta can elegantly be expressed in the frame where the initial and final meson have opposite velocities,

$$P = (\omega_P, -\frac{M}{M+M'} \mathbf{q}), \quad P' = (\omega_{P'}, \frac{M'}{M+M'} \mathbf{q}), \quad (4.1.25)$$

which is the Breit frame for mesons of equal total mass. Here $\mathcal{L}' = \mathcal{L}^{-1}$, $p_0 = 0$ and

$$k = \mathcal{L}^{-1}(0, \mathbf{p}), \quad k' = \mathcal{L}(\beta q_0, \mathbf{p} + \beta \mathbf{q}), \quad k'' = \mathcal{L}(-\alpha q_0, \mathbf{p} - \alpha \mathbf{q}). \quad (4.1.26)$$

The current in the QP model becomes

$$\begin{aligned} J_\mu^{\text{QP}} &= \frac{1}{2\sqrt{\omega_{P'}\omega_P}} M_\mu^{\text{QP}}, \\ M_\mu^{\text{QP}} &= -i \int \frac{d^3 \mathbf{k}}{(2\pi)^3} \left[e_A \bar{\psi}'(P'_{\text{cm}}, k') \Lambda^{-1}(\mathcal{L}') \Gamma_\mu^{A, \text{eff}} \Lambda(\mathcal{L}) \psi(P_{\text{cm}}, k) \right. \\ &\quad \left. + e_B \bar{\psi}'(P'_{\text{cm}}, k'') \Lambda^{-1}(\mathcal{L}') \Gamma_\mu^{B, \text{eff}} \Lambda(\mathcal{L}) \psi(P_{\text{cm}}, k) \right]. \end{aligned} \quad (4.1.27)$$

4.2 Radiative decay

One of the simplest decay processes of an excited meson to a lower mass state takes place through the emission of a single real photon. This process is simple and well-established, since the photon-quark interaction is described by quantum electrodynamics and no strong interactions need to be modeled in some effective way. The combination with the relatively large amount of experimental data on this process makes it a very suitable place for testing the validity of the quasipotential (QP) wave functions found in Chapter 2 and for examining the role of relativity in it. Most calculations of radiative decay rates done up till now are based on nonrelativistic Schrödinger-like equations to which corrections up to $\mathcal{O}(k^2/m^2)$ are added; reviews are given in Refs. [46, 60]. A more relativistic approach has been applied by Daghighian and Silverman [19]. They use a QP model in which the spectator quark is put on its mass shell but the full Dirac structure of the interacting quark is taken into account.

We do not make extensive predictions for yet unobserved decay widths. For the heavy mesons this has already been done in Ref. [19]. The ingredients of our calculation which are not present in [19], i.e. the full Dirac structure of both quarks, are not expected to give large contributions to the radiative decay of heavy mesons. Furthermore, the flavor-independent potential used in this work is adjusted to both the light and heavy meson masses, and it does not give heavy meson mass spectra or heavy meson wave functions as good as can be expected from a potential fitted solely to heavy mesons. For the light mesons the decay is probably dominated by hadronic processes such as vector meson dominance [2]; hadronic processes are not considered in the present calculations. Indeed, we find that the pure electromagnetic radiative widths of the light mesons are much lower than their experimental radiative widths. The QP model probably provides a reliable description for decays of $Q\bar{q}$ systems. These have some amount of interest since they are a nice place for testing heavy quark limit models [44] and for measuring electroweak quark transitions. Unfortunately these decays are difficult to measure and almost no experimental numbers are available.

An interesting question is to what extent the decay rates obtained through various nonrelativistic approximations differ from those found in a complete relativistic analysis; Section 4.2.1 describes which steps are made to obtain the nonrelativistic decay rate from the relativistic QP expression. The QP model is very well suited for giving estimates of the importance of including Lorentz boost and recoil effects, and of including all positive and negative energy states. This is done in Section 4.2.2, which starts with the nonrelativistic radiative decay rates and consecutively adds the relativistic ingredients leading to the QP rates. Although all these ingredients are of order k/m or smaller, it turns out that even for the heavy mesons they can change the rate by more than a factor of four. In Section 4.2.3 the dependence on the model

wave functions is investigated and in Section 4.2.4 a comparison is made between our calculations and rates obtained in other models and from experiment. Finally some concluding remarks are made in Section 4.2.5.

The radiative decay width for an unpolarized meson M to decay into an unpolarized meson M' of momentum P' by emission of a photon of momentum $-q = -(q, \mathbf{q})$ is given by [61]

$$\Gamma(M \rightarrow M' + \gamma) = \frac{(2\pi)^4}{2\omega_P} \frac{1}{2J+1} \sum_{J_z} \sum_{J'_z} \sum_{\lambda} \int \frac{d^3\mathbf{P}'}{(2\pi)^3 2\omega_{P'}} \frac{d^3\mathbf{q}}{(2\pi)^3 2q} \delta^4(P' - P - q) |M_{\mu}\varepsilon^{\mu}(\mathbf{q}, \lambda)|^2, \quad (4.2.28)$$

where the summations run over the z -components of the total angular momenta J_z and J'_z of the initial and final mesons and over the two polarizations λ of the emitted photon. Working out the integrations one finds in the cm system of the decaying meson

$$\begin{aligned} \Gamma(M \rightarrow M' + \gamma) &= \frac{1}{32\pi^2} \frac{q}{M^2} \frac{1}{2J+1} \sum_{J_z} \sum_{J'_z} \sum_{\lambda} \int d^2\Omega_q |M_{\mu}\varepsilon^{\mu}(\mathbf{q}, \lambda)|^2 \\ &= \frac{1}{4\pi} \frac{q}{M^2} \frac{1}{2J+1} \sum_{J_z} \sum_{J'_z} |M_{\mu}\varepsilon^{\mu}(q\hat{\mathbf{z}}, +)|^2, \end{aligned} \quad (4.2.29)$$

where the second equality follows from the fact that both mesons are unpolarized; there is no preferred direction or polarization for the photon so one can choose the photon to be sent in the z -direction with positive helicity. The photon momentum is $q = (M^2 - M'^2)/2M$ and its polarization vector is $\varepsilon^{\mu}(q\hat{\mathbf{z}}, +) = (0, [\hat{\mathbf{x}} + i\hat{\mathbf{y}}]/\sqrt{2})$.

4.2.1 Nonrelativistic reduction

In the nonrelativistic limit the photon energy is small compared to the inverse of the characteristic size a of the mesons, $qa \ll 1$. The transition current \mathbf{J} can then be written as a power series in q of which the coefficients represent the multipole moments of the meson currents [7]. The first two terms lead to the electric dipole and magnetic dipole transitions. The electric dipole transitions only occur between states of opposite parity and which differ one unit in orbital angular momentum ($P' = -P$, $\Delta L = L' - L = \pm 1$). The magnetic dipole transitions only occur between states of equal parity and orbital angular momenta differing not more than one unit ($P' = P$, $|\Delta L| \leq 1$). We will now show how these two terms can be found from Eq. (4.2.29). For simplicity the derivation is restricted to the equal quark mass case and to states having angular momentum $L = 0$ or $L = 1$.

Consider the current of quark A . Keeping only leading terms in k/m yields

$$\mathbf{J}_A \simeq \frac{-ie_A}{2M} \int \frac{d^3\mathbf{k}}{(2\pi)^3} \bar{\psi}'(\mathbf{k}') \Lambda^{-1}(\mathcal{L}') \gamma_\mu^A S_{B,\text{eff}}^{-1}(p_B) \Lambda(\mathcal{L}) \psi(\mathbf{k}). \quad (4.2.30)$$

The meson wave function is now expanded as the product of the two quarks spinors, $\psi(\mathbf{k}) = \psi_A(\mathbf{k})\psi_B(-\mathbf{k})$, and in leading order the spinor structure of quark B is negligible. For the spinor of A only the positive energy component χ needs to be considered,

$$\psi_A(\mathbf{k}) \simeq \sqrt{2M} \begin{pmatrix} 1 \\ \frac{\boldsymbol{\sigma} \cdot \mathbf{k}}{2m} \end{pmatrix} \chi(\mathbf{k}). \quad (4.2.31)$$

The factor $\sqrt{2M}$ ensures that χ has the same normalization as the nonrelativistic wave function, as will be shown in Eq. (4.2.33). Inserting the explicit forms for the spin boosts Λ [Eq. (4.1.11)] gives in leading order

$$\begin{aligned} \mathbf{J}_A &\simeq \frac{-ie_A}{2M} \int \frac{d^3\mathbf{k}}{(2\pi)^3} \bar{\psi}'_A(\mathbf{k}') \left[\boldsymbol{\gamma} - \frac{\gamma_0}{2M} \left\{ (\boldsymbol{\gamma} \cdot \mathbf{P}') \boldsymbol{\gamma} + \boldsymbol{\gamma} (\boldsymbol{\gamma} \cdot \mathbf{P}') \right\} \right]_A \psi_A(\mathbf{k}) \\ &\simeq \frac{-ie_A}{2M} \int \frac{d^3\mathbf{k}}{(2\pi)^3} \psi'^*_A(\mathbf{k}') \left[\gamma_0 \boldsymbol{\gamma} + \frac{\mathbf{P}' + \mathbf{P} + i(\mathbf{P}' - \mathbf{P}) \times \boldsymbol{\sigma}}{2M} \right]_A \psi_A(\mathbf{k}) \\ &\simeq -ie_A \int \frac{d^3\mathbf{k}}{(2\pi)^3} \chi'^*_A(\mathbf{k}') \left[\frac{\mathbf{k}' + \mathbf{k} + i(\mathbf{k}' - \mathbf{k}) \times \boldsymbol{\sigma}}{2m} \right. \\ &\quad \left. + \frac{\mathbf{P}' + \mathbf{P} + i(\mathbf{P}' - \mathbf{P}) \times \boldsymbol{\sigma}}{2M} \right]_A \chi_A(\mathbf{k}) \\ &\simeq -ie_A \int \frac{d^3\mathbf{k}}{(2\pi)^3} \chi'^*(\mathbf{k}') \left[\frac{\mathbf{k}' + \mathbf{k} + i\mathbf{q} \times \boldsymbol{\sigma}}{2m} + \frac{\mathbf{P}' + \mathbf{P}}{2M} \right] \chi(\mathbf{k}), \end{aligned} \quad (4.2.32)$$

where the last equality follows from $\mathbf{k}' - \mathbf{k} = \mathbf{q}/2$, $\mathbf{P}' - \mathbf{P} = \mathbf{q}$ and $M \simeq 2m$. Note that the spin boosts are essential for deriving this current. In a similar way one gets for the charge of quark A

$$J_A^0 \simeq -ie_A \int \frac{d^3\mathbf{k}}{(2\pi)^3} \chi'^*(\mathbf{k}) \chi(\mathbf{k}), \quad (4.2.33)$$

which implies that χ has the usual nonrelativistic normalization $\int d^3\mathbf{x} |\chi(\mathbf{x})|^2 = 1$. For an electric dipole (E1) transition the initial and final states of A have equal spin and one finds in the Breit system

$$\begin{aligned} \mathbf{J}_A &\simeq -ie_A \int \frac{d^3\mathbf{k}}{(2\pi)^3} \chi'^*(\mathbf{k}) \frac{\mathbf{k}}{m} \chi(\mathbf{k}) \\ &\simeq \frac{e_A}{2} \int d^3\mathbf{r} \chi'^*(\mathbf{r}) [H, \mathbf{r}] \chi(\mathbf{r}). \end{aligned} \quad (4.2.34)$$

Here H is the Hamiltonian for which approximately $[H, \mathbf{r}] = -i\partial H/\partial \mathbf{k} \simeq -2i\mathbf{k}/m$. Proceeding further leads to

$$\begin{aligned} \mathbf{J}_A &\simeq \frac{qe_A}{2} \int d^3\mathbf{r} \chi'^*(\mathbf{r}) \mathbf{r} \chi(\mathbf{r}) \\ &= \frac{qe_A}{2} \langle f|\mathbf{r}|i \rangle \sqrt{S}. \end{aligned} \quad (4.2.35)$$

The dipole moment $\langle f|\mathbf{r}|i \rangle$ is the expectation value of \mathbf{r} in the spatial wave functions, and S is a statistical factor which accounts for the spin structure; for spin singlets $S = 1$, and for spin triplets with $L = 0$ or $L = 1$ it reads $S = (2J + 1)(2J' + 1)/9$. Combining Eqs. (4.1.1), (4.1.4) and (4.2.35) gives

$$\begin{aligned} |\mathbf{M}_\mu \varepsilon^\mu(\mathbf{q}, \lambda)|^2 &\simeq \frac{q^2 M^2 S}{2} (e_A + \eta'_C \eta_C e_B)^2 |\langle f|\hat{\mathbf{x}} + i\hat{\mathbf{y}}|i \rangle|^2 \\ &= \frac{4q^2 M^2 S}{3} e_Q^2 |\langle f|r|i \rangle|^2. \end{aligned} \quad (4.2.36)$$

The last equality is only valid if the initial or final state is spherically symmetric. We introduced the average charge $e_Q = (e_A + \eta'_C \eta_C e_B)/2$. Clearly, for systems with quarks of opposite charge, such as charmonium and bottomonium, the average charge is only non-zero if the initial and final mesons have different charge parities. The electric dipole transition now readily follows from Eq. (4.2.29) to be

$$\Gamma^{\text{E1}}(M \rightarrow M' + \gamma) = \frac{S}{2J + 1} \frac{4q^3}{3} \frac{e_Q^2}{4\pi} |\langle f|r|i \rangle|^2. \quad (4.2.37)$$

On the other hand, only the term proportional to $\boldsymbol{\sigma}$ in Eq. (4.2.32) contributes for magnetic dipole (M1) transitions. For the decay ${}^3S_1 \rightarrow {}^1S_0$ one obtains

$$\begin{aligned} J_1^A + iJ_2^A &\simeq \frac{iqe_A}{2m} \int \frac{d^3\mathbf{k}}{(2\pi)^3} \chi'^*(\mathbf{k}) [\boldsymbol{\sigma}_1 + i\boldsymbol{\sigma}_2] \chi(\mathbf{k}) \\ &\simeq -\frac{i\sqrt{2}qe_A}{2m} \int \frac{d^3\mathbf{k}}{(2\pi)^3} \langle f|i \rangle \end{aligned} \quad (4.2.38)$$

and

$$\Gamma^{\text{M1}}({}^3S_1 \rightarrow {}^1S_0 + \gamma) = \frac{4q^3}{3m^2} \frac{e_Q^2}{4\pi} |\langle f|i \rangle|^2. \quad (4.2.39)$$

4.2.2 Comparison with nonrelativistic results

The meson wave functions of the relativistic constituent quark model were Fourier transformed to momentum space and the matrix elements Eq. (4.1.27) of the electromagnetic current were calculated. The matrix elements were inserted in Eq. (4.2.29) to yield the radiative decay widths. The decay width is proportional to the phase space which is fixed by the meson masses. Therefore, in order to avoid inaccuracies, we use the experimental masses and photon energies in the calculation of the decay widths.

Before presenting the final resulting widths, let us first discuss the effects of the various approximations made in Section 4.2.1 that led to the well-known nonrelativistic expressions Eqs. (4.2.37) and (4.2.39) for the dipole transition rate.

The first column of Table 4.1 lists the nonrelativistic dipole transition rates of Eqs. (4.2.37) and (4.2.39). For the wave functions $|i\rangle$ and $|f\rangle$ we used the positive energy components of the wave functions of the BSLT-Coulomb model, which were Fourier transformed to configuration space. The ${}^3D_1^{++}$ component of the ρ meson, which does not contribute to $\mathcal{O}(k/m)$, is neglected; similar approximations are done in the 3P_2 mesons.

The second column of Table 4.1 labeled GI follows the 'mock-meson' prescription of Godfrey and Isgur [29]. It implies relativistic modifications of to the nonrelativistic rates according to

$$\langle f|i\rangle \rightarrow \frac{2\sqrt{\tilde{\omega}'\tilde{\omega}}}{\tilde{\omega}' + \tilde{\omega}} \langle f|\left(\frac{m}{\omega}\right)^{0.7}|i\rangle \quad (4.2.40)$$

in the M1 transition rate, and

$$\langle f|r^n|i\rangle \rightarrow \left(\frac{m}{\sqrt{\tilde{\omega}'\tilde{\omega}}}\right)^{0.5} \langle f|r^n|i\rangle \quad (4.2.41)$$

for electric transition rates. Here $\tilde{\omega} = \langle i|\omega|i\rangle$, $\tilde{\omega}' = \langle f|\omega|f\rangle$ and $\omega = \sqrt{m^2 + k^2}$. The digital exponents follow from a fit. Again the dominant positive energy component of the BSLT-Coulomb wave functions are used. For the forbidden M1 transitions $2^3S_1 \rightarrow 1^1S_0$ one has also to take into account the electric quadrupole transitions which amounts to replacing

$$\langle f|i\rangle \rightarrow \langle f|i\rangle - \frac{q^2}{24} \langle f|r^2|i\rangle. \quad (4.2.42)$$

The corresponding rates are listed in the columns labeled +E2.

The nonrelativistic E1 rates are derived by approximating $2\mathbf{k} \simeq im[H, \mathbf{r}]$ in Eq. (4.2.34). The column Table 4.1 labeled $\langle k\rangle$ shows the decay rate without this approximation, i.e. making the substitution

$$\langle f|r|i\rangle \rightarrow \frac{2}{q} \langle f|\frac{k}{m}|i\rangle \quad (4.2.43)$$

Table 4.1: Electromagnetic dipole decay widths (in keV) calculated from the BSLT-Coulomb model wave functions of Chapter 2, using experimental masses where possible. The first column lists the nonrelativistic decay widths, and the last two columns the full QP results. The columns in between show the accumulative effects of the various relativistic corrections as explained in the text. The widths listed under E1, M1 and +E2 are essentially nonrelativistic expressions. The various widths shown under E1 Γ are calculated from the J^{E1} current to which increasingly more effects are added until the full vertex operator is reached. The rates under ID are obtained from the full J^{ID} current. The experimental data are from the particle data group [61].

	NR	GI	$\langle k \rangle$	E1 Γ	E1 Γ	E1 Γ	E1 Γ	E1 Γ	ID	Exp.
	E1	E1	E1	$ +\rangle$	$+\mathcal{L}q$	$+\Lambda$	$+ eo\rangle$	$+ -\rangle$		
$b_1^+ \rightarrow \pi^+$	170	71	919	17	0.1	0.6	0.7	0.6	0.4	230 ± 60
$a_1^+ \rightarrow \rho^+$	57	25	502	53	57	70	40	41	41	
$\chi_{c2} \rightarrow \psi$	375	336	514	341	298	281	306	307	306	270 ± 30
$\chi_{c1} \rightarrow \psi$	282	251	479	324	325	345	290	290	290	240 ± 40
$\chi_{c0} \rightarrow \psi$	132	117	381	246	254	269	196	196	195	90 ± 40
$\psi' \rightarrow \chi_{c2}$	19.7	17.1	82.6	45.2	45.9	46.4	41.0	41.0	40.9	22 ± 3
$\psi' \rightarrow \chi_{c1}$	24.3	21.0	85.1	47.2	46.8	46.0	43.4	43.4	43.3	24 ± 4
$\psi' \rightarrow \chi_{c0}$	23.4	20.1	55.9	28.0	26.4	24.6	25.2	25.2	25.2	26 ± 4
$\chi_{b2} \rightarrow \Upsilon$	38.4	37.1	39.2	34.0	32.4	31.7	33.0	33.0	33.0	
$\chi_{b1} \rightarrow \Upsilon$	33.8	32.6	38.4	33.7	33.7	34.5	31.8	31.8	31.8	
$\chi_{b0} \rightarrow \Upsilon$	27.2	26.1	36.7	31.1	31.6	32.8	28.3	28.3	28.3	
$\Upsilon' \rightarrow \chi_{b2}$	1.40	1.34	4.47	3.66	3.68	3.69	3.43	3.43	3.43	2.8 ± 0.7
$\Upsilon' \rightarrow \chi_{b1}$	1.28	1.22	3.77	3.10	3.09	3.07	2.90	2.90	2.90	2.9 ± 0.7
$\Upsilon' \rightarrow \chi_{b0}$	0.71	0.68	1.89	1.51	1.50	1.48	1.42	1.42	1.42	1.9 ± 0.6
	NR	GI	NR	GI	ET	ET	ET	ET	ID	Exp.
	M1	M1	+E2	+E2	$+\mathcal{L}q$	$+\Lambda$	$+ eo\rangle$	$+ -\rangle$		
$\rho^+ \rightarrow \pi^+$	215	85	193	76	3	26	29	26	24	68 ± 7
$\psi \rightarrow \eta_c$	2.04	1.78	2.04	1.77	0.37	1.93	1.91	1.85	1.86	1.1 ± 0.3
$\psi' \rightarrow \eta_c^{a)}$	292	222	1888	89	59	1	30	3	9	800 ± 200
$\Upsilon \rightarrow \eta_b^{a)}$	7.7	7.4	7.7	7.4	1.7	7.9	7.8	7.7	7.7	
$\Upsilon' \rightarrow \eta_b^{a)}$	10.7	2.0	22.7	8.1	0.1	3.9	3.7	3.2	3.3	

a) In units of eV.

Table 4.2: Some electric dipole decay widths (in keV). This Table is similar to the first part of Table 4.1 but it uses the calculated masses and photon momenta instead of the experimental ones.

	NR	GI	$\langle k \rangle$
	E1	E1	E1
$b_1^+ \rightarrow \pi^+$	68	28	679
$a_1^+ \rightarrow \rho^+$	23	10	371
$\chi_{c2} \rightarrow \psi$	380	340	517
$\chi_{c1} \rightarrow \psi$	279	249	478
$\chi_{c0} \rightarrow \psi$	166	147	411
$\psi' \rightarrow \chi_{c2}$	92	80	139
$\psi' \rightarrow \chi_{c1}$	85	73	129
$\psi' \rightarrow \chi_{c0}$	44	38	69
$\chi_{b2} \rightarrow \Upsilon$	35.6	34.3	38.2
$\chi_{b1} \rightarrow \Upsilon$	30.2	29.1	37.0
$\chi_{b0} \rightarrow \Upsilon$	23.8	22.9	35.1
$\Upsilon' \rightarrow \chi_{b2}$	6.04	5.79	7.29
$\Upsilon' \rightarrow \chi_{b1}$	4.85	4.64	5.89
$\Upsilon' \rightarrow \chi_{b0}$	2.21	2.12	2.75

in Eq. (4.2.37). Some care should be taken in interpreting the effect of this operation on the rates in Table 4.1. In this Table the experimental photon momenta are used for Eq. (4.2.43), whereas this relation is assumed to be only valid for the calculated photon momenta. Since the calculated photon momenta may differ somewhat from the experimental numbers we also give Table 4.2 which reproduces part of Table 4.1 but uses solely the calculated masses and calculated photon momenta.

Both Tables show that the effect of replacement (4.2.43) is dramatic. Even for the heavy cc system the configuration and momentum dipole moments can differ more than a factor of two. This difference is partly due to the neglect of the relativistic expression for the kinetic energy in H , i.e. $\omega - m$ instead of $k^2/2m$. However, the biggest difference is caused by the neglect in $[H, \mathbf{r}]$ of the momentum dependence of the projection on positive energy states of the confining potential. A nice way of explaining these differences is the following. Let us not take the experimental photon momentum q in Eq. (4.2.43) but instead the theoretical photon momentum q_{th} obtained from the mass spectrum of the Schrödinger equation, shown in Fig. 3.1(a). The Schrödinger spectrum has almost twice as large spacings and hence $q_{\text{th}} \approx 2q$. Using q_{th} in Eq. (4.2.43) one finds more or less consistent configuration and momentum dipole moments. Similarly, if one corrects Eq. (4.2.43) for the relativistic expression for the kinetic energy by replacing $k/m \rightarrow k/\omega$, then it is possible to use q_{th} as obtained from the mass spectrum of the Schrödinger equation with relativistic kinetic energy, shown in Fig. 3.1(b). In general, let us note that all ups and downs in the mass spectra of Fig. 3.1 have corresponding downs and ups in the decay vertices in Table 4.1 which tend to compensate each other to give only moderate modifications of the final decay probabilities. This clearly illustrates the importance of having a current consistent with the dynamics. The need for consistency was already recognized in the slightly different context of baryon photoproduction by Ref. [16] where it is stressed that consistency requires that both the Hamiltonian and the transition current should be evaluated up to $\mathcal{O}(k^2/m^2)$. Indeed, the relativized quark model shows considerable changes in the baryon photoproduction amplitudes if the terms of $\mathcal{O}(k^2/m^2)$ are added to the transition operator [13].

The next step towards the full QP current is to abandon the approximation of keeping only the leading terms in k/m and to consider the full projection of the current on positive energy states,

$$\mathbf{J}_A^{++,++} \equiv \frac{-ie_A}{2\sqrt{M'M}} \int \frac{d^3\mathbf{k}}{(2\pi)^3} \bar{\psi}'(\mathbf{k}) \left[\Lambda_A^+ \boldsymbol{\gamma}^A \Lambda_A^+ \Lambda_B^+ \right] \psi(\mathbf{k}). \quad (4.2.44)$$

The projection operators Λ_i^\pm are defined in Eq. (2.2.16). The effect of this is threefold: first, a replacement in the right hand side of Eq. (4.2.43) is made,

$$\langle f | \frac{k}{m} | i \rangle \rightarrow \langle f | \left(\frac{m + \omega}{2\omega} \right)^2 \frac{2k}{m + \omega} | i \rangle. \quad (4.2.45)$$

The factor $(m + \omega)^2/(2\omega)^2$ comes from the normalization of the positive states. Second, some small extra contributions proportional to $k^3/(m + \omega)^3$ and the ${}^3D_1^{++}$ and ${}^3F_2^{++}$ waves are included. And finally an extra factor M'/M associated with the wave function normalizations enters the decay width. These effects decrease the decay rate considerably, what also can be seen from the corresponding electric dipole rates listed in the column ET|+⟩ of Table 4.1. The M1 transitions are zero if the initial and final relative momenta are equal.

The photon momentum transferred to the struck quark gives a shift between the initial and final relative momenta. It reads [see Eq. (4.1.26)]

$$\mathbf{k}' - \mathbf{k} = \beta \mathcal{L} \mathbf{q}, \quad (4.2.46)$$

where $\beta = \frac{1}{2}$ for equal quark masses. Note that this is the only place where the spatial Lorentz boost \mathcal{L} enters the decay width. Including the shift yields a current

$$\begin{aligned} \mathbf{J}_A^{+,+,+} \rightarrow & \frac{-ie_A}{2\sqrt{M'M}} \int \frac{d^3\mathbf{k}}{(2\pi)^3} \overline{\psi}'(\mathbf{k}') \\ & \left[\Lambda_A^+(\mathbf{k}'_A) \boldsymbol{\gamma}^A \Lambda_A^+(\mathbf{k}_A) \Lambda_B^+(\mathbf{k}'_B) S_{\text{eff}}^{-1}(\mathbf{k}_B) \Lambda_B^+(\mathbf{k}_B) \right] \psi(\mathbf{k}). \end{aligned} \quad (4.2.47)$$

In the QP model no definite prescription exists for the effective inverse propagator S_{eff}^{-1} of the spectator quark. In Section 4.1 two prescriptions were discussed which lead to the QP currents J^{E1} and J^{1D} , and to their associated effective propagators. We concentrate on J^{ET} . The three-dimensional reduction of the current gives a mismatch such that $\mathbf{k}'_B \neq \mathbf{k}_B$, through which the negative energy behavior of S_{eff}^{-1} slips into the projection on positive energy states of the current. Column ET+ $\mathcal{L}q$ lists the decay rates of this vertex.

The Lorentz boosts which bring the mesons to their cm system act on the spin coordinates as well. The spin boosts Λ are included in the column labeled ET+ Λ . The nonrelativistic reduction of the current Eq. (4.2.32) shows that they are of order q/M for E1 transitions, and that for M1 transitions they are responsible for half of the current.

Next the once negative energy states are added; the results are listed under ET+| eo ⟩ in Table 4.1. Most decay rates are reduced by the once negative energy states. For E1 transitions of heavy mesons the once negative energy states are even much more important than the spin boosts. Let us quote some numbers for the decay $\chi_{c0} \rightarrow \psi + \gamma$ which illustrate how these states enter the decay strength. The transition current has as major contributions

$$\begin{aligned} \langle \psi | \boldsymbol{\gamma}^A | \chi_{c0} \rangle \simeq & \text{pw} \langle {}^3S_1^{++} | \boldsymbol{\gamma}^A | {}^3P_0^{++} \rangle_{\text{pw}} + \text{pw} \langle {}^3S_1^{++} | \boldsymbol{\gamma}^A | {}^1S_0^e \rangle_{\text{pw}} \\ & + \text{pw} \langle {}^1P_1^e | \boldsymbol{\gamma}^A | {}^3P_0^{++} \rangle_{\text{pw}} + \text{pw} \langle {}^3P_1^o | \boldsymbol{\gamma}^A | {}^3P_0^{++} \rangle_{\text{pw}}. \end{aligned} \quad (4.2.48)$$

Since γ^A connects upper components with lower components, the contribution of the first term on the right hand side is approximately $\sqrt{2} \langle f|k/2m|i \rangle = 0.34$ (the factor $\sqrt{2}$ follows from the Clebsch-Gordan algebra). The other terms represent currents between once negative energy states (which consist mainly of lower components) and positive energy states (which consist mainly of upper components) so these currents are approximately equal to the spatial overlaps, which are almost one. The probability for the χ_{c0} meson to be found in its $|^1S_0\rangle_{\text{pw}}$ state is 0.12%, so the second term is roughly -0.035 . In a similar way one finds that the last two terms contribute -0.013 and -0.008 . The minus signs reflect the negative charge associated with negative energy states. Altogether one finds that the ratio of decay rates with and without negative energy states is $\simeq [(0.34 - 0.056)/0.34]^2$, which approximately equals the ratio 169/269 of Table 4.1. The double negative energy states have a small contribution to the decay, as could be expected from their smallness. We obtain the rates listed in column ET+| $-$) if they are also included.

Finally we list the decay rate for the full current of J^{D} . The differences with the J^{ET} results are negligible.

4.2.3 Parameter dependence

Table 4.3 lists the electromagnetic dipole decay rates calculated from the three different QP model wave functions of Chapter 2, which are the BSLT model in the Feynman gauge and the BSLT and ET models in the Coulomb gauge. The middle column of Table 4.3 repeats the BSLT-Coulomb results of Table 4.1. The BSLT-Feynman and BSLT-Coulomb model results hardly differ, and the ET results tend to be somewhat higher. However, for most decays the differences are smaller than the experimental uncertainties, and there is no reason to favor one of the models.

4.2.4 Comparison with experiment

Table 4.4 lists various decay rates together with the calculations of Godfrey and Isgur [29], Körner *et al.* [44] and of Daghighian and Silverman [19]. The predictions of [44] are based on the large mass limit for the heavy quark and do not include all multipole contributions. The calculations of [19] are performed within a relativistic quasipotential framework in which the spectator quark is put on mass shell.

The calculated widths for the decays $(a_2^+, a_1^+, b_1^+) \rightarrow \pi^+ + \gamma$ are clearly too small. If we use different meson wave functions, which are found with other parameter sets or other propagators, we also find decay widths which are less than 10 keV. Thus the discrepancy between the calculated and experimental widths is mainly caused by the form of the decay vertex, and not by the form of the wave functions. A good description of these decays can be given by using vector meson dominance [2]. One assumes the hadronic decay of the meson into a π^+ and a vector meson, followed by the

Table 4.3: Comparison of electromagnetic dipole decay widths (in keV) calculated with J^{ET} from different model wave functions, using experimental masses where possible.

	BSLT Feynman	BSLT Coulomb	ET	Experiment
$b_1^+ \rightarrow \pi^+ + \gamma$	3.0	0.6	11.3	230 ± 60
$a_1^+ \rightarrow \rho^+ + \gamma$	39	41	30	
$\chi_{c2} \rightarrow \psi + \gamma$	322	307	348	270 ± 30
$\chi_{c1} \rightarrow \psi + \gamma$	296	290	303	240 ± 40
$\chi_{c0} \rightarrow \psi + \gamma$	211	196	203	90 ± 40
$\psi' \rightarrow \chi_{c2} + \gamma$	42.6	41.0	58.4	22 ± 3
$\psi' \rightarrow \chi_{c1} + \gamma$	41.5	43.3	59.8	24 ± 4
$\psi' \rightarrow \chi_{c0} + \gamma$	28.1	25.2	27.5	26 ± 4
$\chi_{b2} \rightarrow \Upsilon + \gamma$	34.1	33.0	32.8	
$\chi_{b1} \rightarrow \Upsilon + \gamma$	32.8	31.8	30.3	
$\chi_{b0} \rightarrow \Upsilon + \gamma$	29.8	28.3	26.9	
$\Upsilon' \rightarrow \chi_{b2} + \gamma$	3.56	3.43	3.81	2.8 ± 0.7
$\Upsilon' \rightarrow \chi_{b1} + \gamma$	2.90	2.90	3.19	2.9 ± 0.7
$\Upsilon' \rightarrow \chi_{b0} + \gamma$	1.42	1.42	1.31	1.9 ± 0.6
$\rho^+ \rightarrow \pi^+ + \gamma$	38	26	42	68 ± 7
$\psi \rightarrow \eta_c + \gamma$	1.77	1.85	1.62	1.1 ± 0.3
$\psi' \rightarrow \eta_c + \gamma^a)$	42	3	2541	800 ± 200
$\Upsilon \rightarrow \eta_b + \gamma^a)$	8.1	7.7	51	
$\Upsilon' \rightarrow \eta_b + \gamma^a)$	0.7	3.2	64	

a) In units of eV.

Table 4.4: Meson decay widths (in keV) calculated from the BSLT-Coulomb model of Chapter 2 using Γ^{E1} compared with experimental rates and other calculations. The listed decays of the D_1 and D_{s1} mesons are the averages of the decay of their 3P_1 and 1P_1 states.

	Ref. [29]	Ref. [44]	BSLT	Experiment
$a_2^+ \rightarrow \pi^+ + \gamma$	303		0.8	295 ± 60
$a_1^+ \rightarrow \pi^+ + \gamma$	314		2.4	640 ± 250
$b_1^+ \rightarrow \pi^+ + \gamma$	397		0.6	230 ± 60
$\rho^+ \rightarrow \pi^+ + \gamma$	68		26	68 ± 7
$K^{*0} \rightarrow K^0 + \gamma$	117		87	117 ± 10
$K^{*+} \rightarrow K^+ + \gamma$	68		31	50 ± 5
$D^{*0} \rightarrow D^0 + \gamma$	22		15	< 950
$D^{*+} \rightarrow D^+ + \gamma$	0.9		0.4	< 200
$D_1^0 \rightarrow D^0 + \gamma$		245 ± 18	310	
$D_1^0 \rightarrow D^{*0} + \gamma$		161 ± 5	277	
$D_2^{*0} \rightarrow D^{*0} + \gamma$		309 ± 16	417	
$D_2^{*0} \rightarrow D^0 + \gamma$		181	20	
$D_s^* \rightarrow D_s + \gamma$			0.1	
$D_{s1} \rightarrow D_s + \gamma$		1.6 ± 2.3	2.2	
$D_{s1} \rightarrow D_s^* + \gamma$		10.4 ± 1.0	2.9	
$D_{s2}^* \rightarrow D_s^* + \gamma$		9.4 ± 2.0	3.5	
$D_{s2}^* \rightarrow D_s + \gamma$		16	9	

continued on next page →

Table 4.4: Continued.

	Ref. [29]	Ref. [19]	BSLT	Experiment
$\chi_{c2} \rightarrow \psi + \gamma$	250	210	307	270 ± 30
$\chi_{c1} \rightarrow \psi + \gamma$	194	100	290	240 ± 40
$\chi_{c0} \rightarrow \psi + \gamma$	90	56	196	90 ± 40
$\psi' \rightarrow \chi_{c2} + \gamma$	19.6	24	41.0	22 ± 3
$\psi' \rightarrow \chi_{c1} + \gamma$	22.5	23	43.4	24 ± 4
$\psi' \rightarrow \chi_{c0} + \gamma$	19.6	12	25.2	26 ± 4
$\psi \rightarrow \eta_c + \gamma$	1.95	0.91	1.85	1.1 ± 0.3
$\psi' \rightarrow \eta_c + \gamma$	2.3	1.0	0.003	0.8 ± 0.2
$\psi' \rightarrow \eta'_c + \gamma$	1.1	0.60	0.79	
$\chi_{b2} \rightarrow \Upsilon + \gamma$	32	28.3	33.0	
$\chi_{b1} \rightarrow \Upsilon + \gamma$	29	22.5	31.8	
$\chi_{b0} \rightarrow \Upsilon + \gamma$	26	19.0	28.3	
$\Upsilon' \rightarrow \chi_{b2} + \gamma$	1.6	1.81	3.43	2.8 ± 0.7
$\Upsilon' \rightarrow \chi_{b1} + \gamma$	1.4	1.64	2.90	2.9 ± 0.7
$\Upsilon' \rightarrow \chi_{b0} + \gamma$	0.63	0.87	1.42	1.8 ± 0.6
$\chi'_{b2} \rightarrow \Upsilon + \gamma$	8.1	7.7	3.7	9 ± 2
$\chi'_{b1} \rightarrow \Upsilon + \gamma$	4.8	14.3	2.4	7 ± 2
$\chi'_{b0} \rightarrow \Upsilon + \gamma$	2.2	1.8	0.8	4 ± 3
$\chi'_{b2} \rightarrow \Upsilon' + \gamma$	14.4	13.0	19.8	24 ± 6
$\chi'_{b1} \rightarrow \Upsilon' + \gamma$	12.1	11.1	18.2	20 ± 5
$\chi'_{b0} \rightarrow \Upsilon' + \gamma$	10.0	9.7	15.3	(22 ± 13)
$\Upsilon'' \rightarrow \chi'_{b2} + \gamma$	1.9	2.54	4.6	2.8 ± 0.4
$\Upsilon'' \rightarrow \chi'_{b1} + \gamma$	1.8	2.17	3.7	2.8 ± 0.4
$\Upsilon'' \rightarrow \chi'_{b0} + \gamma$	0.9	1.06	1.7	1.3 ± 0.2

transition of the vector meson to a photon, $M \rightarrow \pi^+ + V^0 \rightarrow \pi^+ + \gamma$, ($V^0 = \rho^0, \omega^0, \varphi^0$). In a way, the smallness of the non-hadronic calculations of Table 4.4 strengthens the assumption of vector meson dominance.

Most of the calculated decays of the heavy mesons are close to their experimental values. A number of them show better agreement than the other two models listed in Table 4.4, which both tend to underestimate the decay widths. The major relativistic correction to the E1 rates is the increase due to replacing the configuration dipole moment by the unapproximated momentum dipole moment [cf. Eq. (4.2.43)]. We conclude that use of the momentum dipole moment operator is essential in a relativistic calculation of the electromagnetic current.

The heavy meson wave functions used here follow from a confining potential that has a string tension $\kappa = 0.33 \text{ GeV}^2$, which is almost twice the commonly accepted value. Therefore it is to be expected that our wave functions are less extended in configuration space and that they have correspondingly smaller dipole moments and transition probabilities. Remarkably enough, this is not the case.

The forbidden M1 transition $\psi' \rightarrow \eta_c + \gamma$ is very poorly described. Table 4.1 shows that this probability greatly depends on the approximations made; apparently the QP model is not suited for describing this transition.

4.2.5 Concluding remarks

In this Section we investigated the electromagnetic decay of light, mixed and heavy mesons in the quasipotential (QP) framework of Chapter 2. Special attention was paid to the nonrelativistic approximations to radiative decay rates. It was shown which steps are made in order to reduce the QP expression to the well-known nonrelativistic expressions. For each step quantitative rates were given which illustrate its contributions. It was found that the once negative energy states give an appreciable contribution to the rates. They are more important than the effects of the Lorentz spin boosts, needed to bring the meson wave functions to their center of mass system. Yet the largest approximation is made when the momentum dipole moment is turned into a configuration dipole moment by means of Eq. (4.2.43). The momentum dependence of the QP projection of the confining potential is neglected in this approximation. It was already noted in Chapter 3 that this QP projection has much influence on the mass spectrum. Here we found a corresponding large modification of the decay rates. It is interesting to note that these two changes roughly compensate each other, resulting in an only modest increase of the final decay probability. The compensation manifestly illustrates the necessity of defining the meson current consistently with the $q\bar{q}$ interaction and $q\bar{q}$ propagation. The net increase yielded better agreement for a number of experimental widths of heavy meson systems as compared to previous calculations.

Table 4.5: Parameters of the fixed coupling constant ET model.

	m [GeV]	α	κ [GeV ²]	c [GeV]	β [GeV]
fixed α ET	0.25	0.318	0.20	-0.529	
Schrödinger	0.25	0.318	0.20	-0.878	1.713

4.3 Electromagnetic form factors

In this Section the electromagnetic form factors of the pion and ρ meson are studied. The experimental data on the pion form factor provide a nice tool for testing simultaneously the low momentum region dominated by the non-perturbative confining potential and the high momentum region dominated by the asymptotic one-gluon-exchange potential. Perturbative QCD predicts that the pion electromagnetic form factor F_π falls off like $Q^2 \ln^{-1}(Q^2)$ for high space-like photon momenta $Q^2 = -q^2$ [23, 48]. (However, Ref. [40] argues that this asymptotic behavior can occur only at energies far beyond the range of present-day accelerators.) The pion wave function diverges at small distances or large momenta, and one can expect this behavior to play an important role in the large momentum behavior of the pion form factor. This has indeed been found in Refs. [15, 30] for the full Bethe-Salpeter equation. We will also see this feature in the QP framework.

In this Section we use the the ET propagator and the ET current J_μ^{ET} [Eq. (4.1.22)]; they have the advantage that the normalization implied by J_0^{ET} is consistent with the normalization derived from S_{ET} . The divergences can best be studied when they are maximal. This is obtained with a coupling constant that is fixed and close to its maximum value, which is $1/\pi$ in the Feynman gauge (the short distance behavior of the pion was analyzed in Appendix 2.B). Hence we take a coupling constant $\alpha = 0.318$. The large α also ensures maximal spin-spin splitting between the π and the ρ masses. The other parameters are listed in Table 4.5. The confinement strength $\kappa = 0.20$ GeV² is chosen within the range of values often used in other constituent quark models. Table 4.6 shows the masses for the lowest excitations of the pion and rho as obtained from the fixed coupling ET model. To illustrate the role of relativity, we have also listed in Table 4.6 the results of the Schrödinger equation (3.3.13) with the $\mathcal{O}(1/m^2)$ spin-dependent corrections V_{SD} [Eq. (3.3.15)] of the Breit interaction included. The delta function appearing in V_{SD} is replaced by a Gaussian of width β_1^{-1} and its x^{-3} singularities are cut off at $\beta_2^{-1} = m^{-1}$ and replaced by a smoothly fitting Gaussian (the x^{-1} singularity in V_{SD} is not regularized). From Table 4.6 we see that the bound state energies in the ET case are more closely spaced. The differences between the Schrödinger and the ET spectra have been discussed in Chapter 3.

Table 4.6: Pion and rho mass spectrum (in GeV) for the fixed coupling ET model. The experimental data are from Ref. [61].

meson	$N^{2S+1}L_J$	observed mass	ET	Schrödinger + $O(1/m^2)$
π	1^1S_0	0.135	0.20	0.20
π'	2^1S_0	1.30 ± 0.10	1.24	1.43
π''	3^1S_0	(1.77 ± 0.03)	1.75	2.29
ρ	1^3S_1	0.768	0.83	0.83
ρ'	1^3D_1	1.47 ± 0.03	1.46	1.81
ρ''	2^3S_1	1.70 ± 0.02	1.49	2.45
ρ'''	2^3D_1	(2.14 ± 0.03)	1.89	2.60
ρ''''	3^3S_1		1.91	3.12

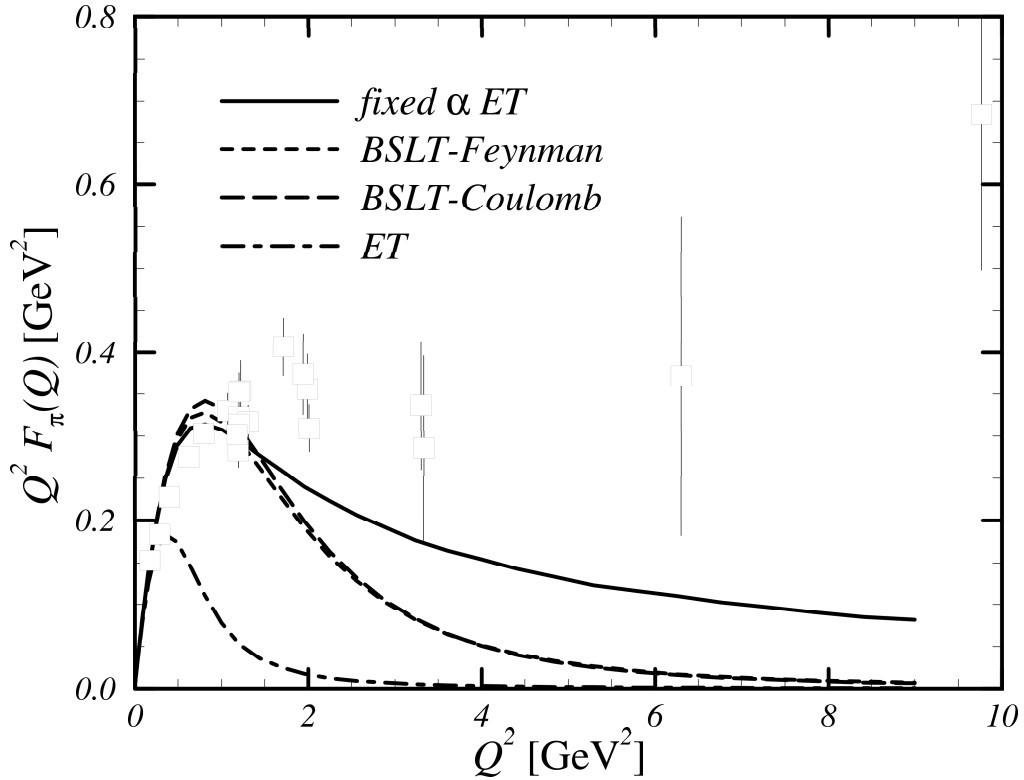


Figure 4.2: Pion form factors F_π as probed with the ET current J_μ^{ET} . The experimental points are taken from Ref. [5]. It has been argued that the analysis by which F_π is extracted from the experimental data is very model dependent [14].

We calculate the electromagnetic form factors with the E1 current J_μ^{E1} . The resulting pion form factors for the fixed α ET model and the running coupling models of Chapter 2 are shown in Fig. 4.2. Their slopes at zero momentum determine the electromagnetic radius $\langle r_{\text{e.m.}}^2 \rangle^{1/2}$, which are 0.48, 0.44, 0.44 and 0.65 fm for the fixed α E1, BSLT-Feynman, BSLT-Coulomb and E1 model, respectively. The experimental radius is 0.663 ± 0.023 fm [20]. Reference [22] gives the general relativistic definition of the electromagnetic multipole form factors. The explicit definitions of these form factors for a spin-one particle are given in Ref. [39]. For the ρ meson we find in the fixed α model $\langle r_{\text{e.m.}}^2 \rangle^{1/2} = 0.43$ fm and for its magnetic and quadrupole moment $\mu = (M_N/M_\rho)F_M(0) = -1.9$ nuclear magnetons and $Q = F_Q(0)/M_\rho^2 = -0.12 \text{ GeV}^{-2}$, respectively. It is difficult to evaluate accurately the ρ meson wave functions in the running coupling models due to the large spatial extension of its $^1P_1^e$ components, so we do not quote the ρ properties in the running coupling models.

A striking feature of the pion form factor is its large tail at high Q^2 , especially in the fixed α E1 model, which resembles the results of perturbative QCD predicting that due to the one-gluon-exchange the meson form factor will fall off like $Q^{-2} \ln^{-1}(Q^2)$ for large Q^2 [23, 48]. A constituent quark model calculation in the light-cone formalism [42] also shows such a large tail. In our model the large tail also follows from the one-gluon-exchange part of the potential. It causes the singular behavior at the origin where ψ_i grows like x^γ , $0 < \gamma < 1$. Its momentum wave function $\psi_i(p)$ consequently falls off like $p^{-1-\gamma}$ for large p . Since the behavior of $F_\pi(Q)$ for large Q follows from that of $\psi(p)$ for large p , one finds that the smaller γ gets the larger the tail of $F_\pi(Q)$ will be. Indeed, the numerical results show that a smaller value of α or a running α , which lead to less singular wave functions, give a faster fall-off in the form factors.

In the next Section it is discussed how the divergence of the wave function at the origin (WFO) can be regularized in order to give finite annihilation decay probabilities. It is pointed out that different approaches to this problem exist which differ in the mechanisms identified as responsible for the divergence. In the renormalization scheme used in the light-front calculations of Ref. [48] the total meson wave function is renormalized whereas in the scheme advocated by Ref. [41] only the annihilation vertex is renormalized. If we apply the renormalization scheme of [48] of the meson wave function to our model then the WFO divergence is absent and the pion form factor will drop as Q^{-4} or faster for large Q . (That the light-front calculation does basically reproduce a Q^{-2} drop is essentially related to the two-dimensionality of the light-front subspace.) However, as we will explain in the next Section, we consider this approach inconsistent and adhere to the interpretation of [41], where only the $q\bar{q}$ annihilation vertex is renormalized. Thus the expression for the pion electromagnetic form factor is not affected and the results and conclusions of this Section are not changed.

4.4 $q\bar{q}$ annihilation decay

Measurement of the decay rate of pseudoscalar mesons through the annihilation of the quark-antiquark pair into a W or Z boson can provide information on the Cabibbo-Kobayashi-Maskawa matrix elements, provided that the annihilation process is well described. The probability for this reaction is determined by the strength of the wave function at small distances. However, calculations of the decay rate in the relativistic framework are troubled by the fact that the wave function at the origin (WFO) diverges as $x \rightarrow 0$, and a prescription must be used to regularize this singularity. In this Section we discuss how the renormalization scheme developed by Ito [41] can be adopted to the FT wave functions. This method is interesting from a theoretical point of view, because it offers a nice understanding of the nature of the divergence and of the renormalization of the WFO. Furthermore, it illustrates how divergent loop expressions can be regularized in the configuration space approach. Yet, this scheme does not give an unambiguous prescription for extracting a finite value for the annihilation decay due to the choices that have to be made for the renormalization point and for the wave function normalization. In view of these, we do not calculate the decay rates in the overview at the end of this Section within this renormalization scheme; the values listed there follow from simply averaging the WFO over a small volume.

The electroweak decay of a pseudoscalar meson is controlled by the coupling of the pseudoscalar meson to the W or Z boson, which is parametrized by the pseudoscalar decay constant f_P . In the constituent quark model this coupling is assumed to take place through the annihilation of the constituent quarks, as shown in Fig. 2.1, and one has in the QP approximation

$$P_\mu f_P = -\frac{1}{\sqrt{2}} \int \frac{d^3\mathbf{p}}{(2\pi)^3} \text{Tr} \left[\gamma_\mu (1 - \gamma_5) \psi(\mathbf{p}) \right] \quad (4.4.49)$$

$$= -\frac{1}{\sqrt{2}} \text{Tr} \left[\gamma_\mu (1 - \gamma_5) \psi(x=0) \right]. \quad (4.4.50)$$

The trace over the color wave functions contributes a factor $\sqrt{3}$. The trace over the Dirac structure can be evaluated by decomposing the pseudoscalar wave function as described in Appendix 2.B,

$$\psi(x, \Omega) = \frac{1}{x} \left[\psi_1(x) |^1S_0^s\rangle + \psi_2(x) |^1S_0^a\rangle + \psi_3(x) |^3P_0^e\rangle \right]. \quad (4.4.51)$$

On this basis, only the $^1S_0^s$ component contributes to the pseudoscalar decay and one finds $\text{Tr} [\gamma_\mu (1 - \gamma_5) \psi] = -2\psi_1(x)/x$.

The leptonic decay width of a vector meson is determined by the probability of the quarks to annihilate into a photon. It is evaluated in a similar way as the

pseudoscalar decay and gives

$$\Gamma(V \rightarrow e^- e^+) = \frac{4\pi\alpha^2 \hat{e}_Q^2}{3M^3} \left\{ \int \frac{d^3\mathbf{p}}{(2\pi)^3} \text{Tr} \left[\gamma_\mu \varepsilon_\mu \psi(\mathbf{p}) \right] \right\}^2, \quad (4.4.52)$$

with \hat{e}_Q the expectation value of the quark charge in units of the elementary charge (e.g. $2/3$ for $c\bar{c}$) and ε_μ the polarization vector of the photon. The expression between curly brackets equals $2\sqrt{3} \lim_{x \rightarrow 0} \psi_j(x)/x$, where the factor $\sqrt{3}$ stems from the color wave function and ψ_j describes the ${}^3S_1^s$ component.

4.4.1 Renormalization of $\psi(0)$

The wave function diverges at the origin. This was discussed in Section 2.3, and Appendix 2.B gives an analysis of the short distance behavior of the pseudoscalar wave function. Reference [48] presents a renormalization method for obtaining finite decay rates in the light-front formalism. It starts from the observation that each quark line should be renormalized by a quark wave function renormalization constant $Z_2^{1/2}$. Hence the total wave function is multiplied by Z_2 . Because of Ward's identity $Z_2 = Z_1$, one may also use the vertex renormalization constant Z_1 for renormalizing the meson wave function. The Z_1 is found to all orders in [48] by exponentiating the explicitly calculated one-loop vertex corrections. The wave function renormalized with this Z_1 is finite at the origin.

Yet this procedure is inconsistent. The meson wave equation does not contain any terms or interactions that give rise to quark self energy effects. Therefore the divergences in the meson wave functions can not and should not be related to the one-quark propagation renormalization. The meson wave equations have as sole input the two-body propagator and the two-body interaction, and they can be the only source of the WFO divergence. This has been recognized by Ito [41] who gives a description of the WFO divergence and renormalization in terms of these two-body operators. Here the annihilation decay is also renormalized by Z_1 , leading to a result that is mathematically equivalent to the approach in [48], but physically different. One can expect different results for other amplitudes, such as the pion electromagnetic form factor as already discussed in the previous Section.

We will now discuss how Ito's renormalization scheme can be adopted for the ET wave functions. The basic idea of the approach is that one must not use the bare annihilation vertex $\hat{\gamma}$ [$\gamma_\mu(1 - \gamma_5)$ or γ_μ] in Eqs. (4.4.49) or (4.4.52), but rather the full vertex Γ which includes the loop corrections to the bare vertex. Since the wave function is calculated in the ladder approximation, the loop corrections are also calculated in the ladder approximation. Thus in the cm system where $P = (W, \mathbf{0})$,

$$\Gamma(W, \mathbf{p}) = \hat{\gamma} - \int \frac{d\mathbf{q}}{(2\pi)^3} V(\mathbf{p} - \mathbf{q}) S(W, \mathbf{q}) \Gamma(W, \mathbf{q}). \quad (4.4.53)$$

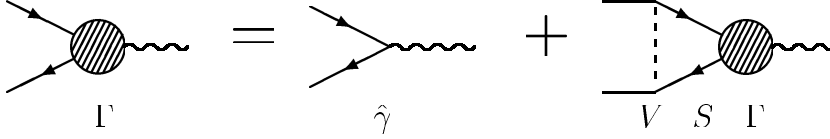


Figure 4.3: Diagrammatic representation of the ladder equation (4.4.53) for the annihilation vertex.

This is illustrated in Fig. 4.3. This equation leads to an infinite Γ due to divergences of the same nature as in the wave equation. They can be regularized by making the bare vertex $\hat{\gamma}$ momentum dependent by introducing a form factor $F(a\mathbf{p})$,

$$\hat{\gamma} \rightarrow \hat{\gamma}F(a\mathbf{p}), \quad (4.4.54)$$

which smears out the point interaction of the annihilation vertex over a small region of size a . The bare vertex is renormalized by the vertex renormalization constant $Z_1(a)$ which is defined by

$$Z_1(a)\Gamma(W_R, \mathbf{p}_R) = \hat{\gamma} \quad (4.4.55)$$

for some special momenta and spinors corresponding to the renormalization point. The choice of this point is ambiguous and is discussed in the next subsection. Inserting the regularized bare vertex and the renormalization constant in Eq. (4.4.49) gives

$$P_\mu f_P = -\frac{1}{\sqrt{2}} \lim_{a \rightarrow 0} Z_1(a) \int \frac{d^3\mathbf{p}}{(2\pi)^3} F(a\mathbf{p}) \text{Tr} [\gamma_\mu (1 - \gamma_5) \psi(\mathbf{p})], \quad (4.4.56)$$

and likewise for the leptonic decay of the vector mesons. In the next paragraphs numerical results are presented which show that this limit does exist and that it gives finite results.

4.4.2 Numerical implementation

For simplicity, we will restrict ourselves to the equal mass ET approximation. Ito [41] has shown how the vertex renormalization for the Dirac hydrogen atom can be carried out in configuration space. This method can be extended to the ET equation as follows. Let $\Phi(W, \mathbf{p}) = S_{\text{ET}}(W, \mathbf{p})\Gamma(W, \mathbf{p})$. Its Fourier transform satisfies

$$\int d\mathbf{x}' S_{\text{ET}}^{-1}(W, \mathbf{x} - \mathbf{x}') \Phi(W, \mathbf{x}') = F(a, \mathbf{x}) \hat{\gamma} - V(\mathbf{x}) \Phi(W, \mathbf{x}). \quad (4.4.57)$$

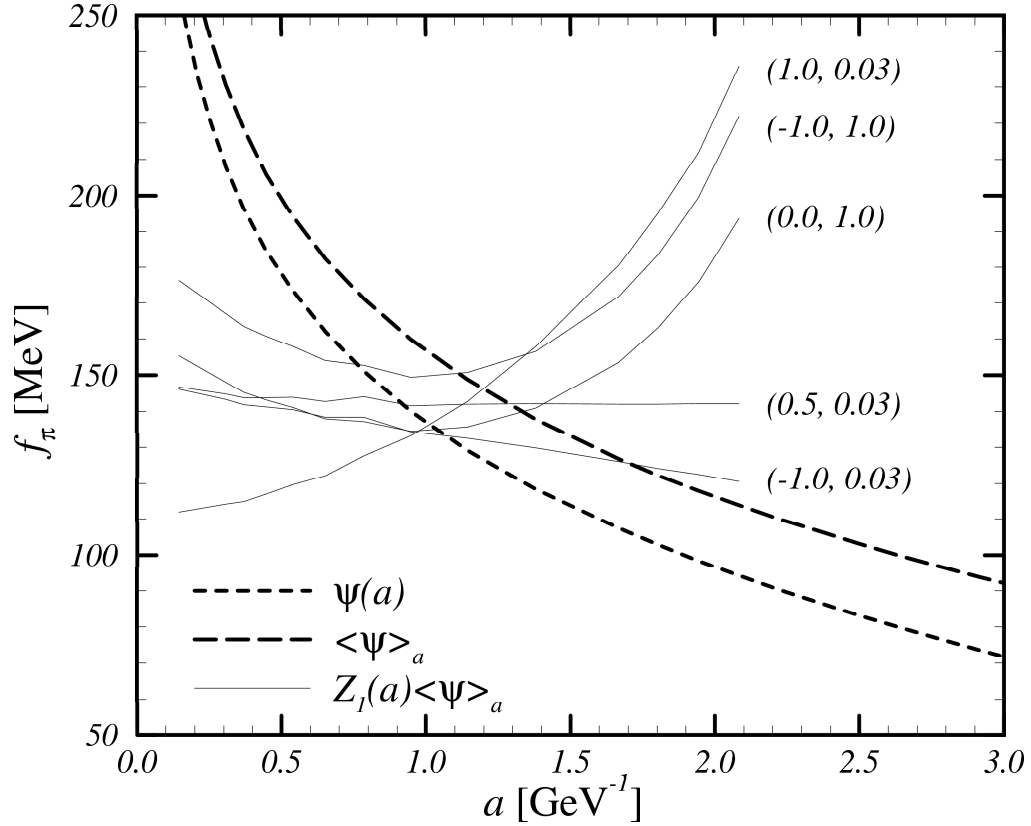


Figure 4.4: The pion decay constant. The thick curves are explained in the text. The thin curves show the dependence of the renormalized decay constants on the renormalization scale a (numerical inaccuracies $\lesssim 5$ MeV below $a = 0.2$ GeV have been removed through averaging). They are labeled by the momenta (W_R, \mathbf{p}_R) [in GeV] of the renormalization point.

Here $F(a, \mathbf{x})$ represents the Fourier transform of the form factor $F(a\mathbf{p})$. Note that the equation for Φ is just the ET wave equation with an additional driving term $F(a, \mathbf{x})\hat{\gamma}$. For the form factor we choose

$$F(a, \mathbf{x}) = \begin{cases} \frac{3}{4\pi a^3} & x < a \\ 0 & x > a. \end{cases} \quad (4.4.58)$$

The numerical solution of Φ can be done using the same configuration space techniques as used in Chapter 2 for solving the ET wave function equations. Since $\hat{\gamma}$ has the J^P of the decaying meson, Φ can be decomposed using the same basis states as needed for the meson wave function. However, the configuration space equations are solved on a limited set of points x_1, \dots, x_k , and thus the method of solution does not distinguish between a driving term $F(a, \mathbf{x})\hat{\gamma}$ cut off at, say, $a = x_3 + \varepsilon$ and $a = x_4 - \varepsilon$. This will give appreciable inaccuracies. In order to avoid these we split $\Phi = \Phi_0 + \varphi$ with

$$\int d\mathbf{x}' S_{\text{ET}}^{-1}(W, \mathbf{x} - \mathbf{x}')\Phi_0(W, \mathbf{x}') = F(a, \mathbf{x})\hat{\gamma} + r(\mathbf{x}), \quad (4.4.59)$$

where $r(\mathbf{x})$ is continuous at $x = a$ and vanishes as $x \rightarrow \infty$. This ensures that the equation for φ is continuous for all x and thus can be solved with much more accuracy than the equation for Φ . We use

$$\Phi_0(W, x) = \begin{cases} G(1 - y^2)y \ln |y| & y < 1 \\ 0 & y > 1, \end{cases} \quad (4.4.60)$$

where $y = (x - a)/a$. For pseudoscalar decay $G = -3/(4\pi^2 a)$ should be used. The resulting $\Phi(W, \mathbf{x})$ was Fourier transformed to momentum space and multiplied by S_{ET}^{-1} to obtain $\Gamma(W, \mathbf{p})$. The $Z_1(a)$ can directly be read from $\Gamma(W, \mathbf{p})$ after choosing the momenta of the renormalization point, and the pseudoscalar decay constant becomes

$$f_P = \frac{\sqrt{3}\sqrt{2}}{M} \lim_{a \rightarrow 0} Z_1(a) \langle \psi \rangle_a, \quad (4.4.61)$$

where

$$\langle \psi \rangle_a = 3a^{-3} \int_0^a dx x \psi_1(x) \quad (4.4.62)$$

represents the $^1S_0^s$ component of the wave function averaged over a spherical volume of radius a .

Let us now use the fixed coupling constant model of Section 4.4 for illustrating the properties of Γ and Z_1 . This model is very well suited for this purpose since the

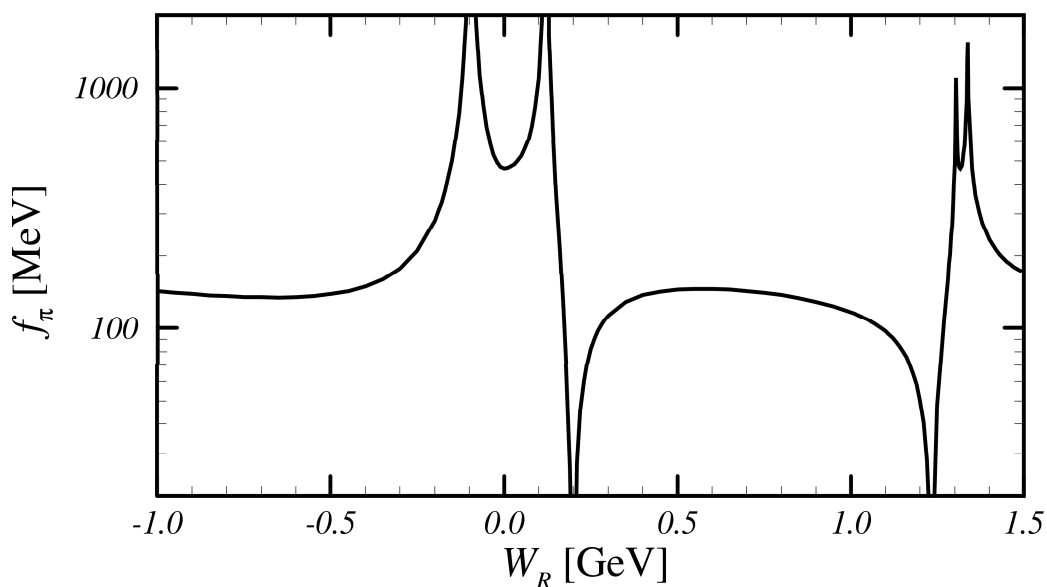


Figure 4.5: The pion decay constant as a function of the total mass W_R with $\mathbf{p}_R = 0.03$ GeV and $a = 0.4$ GeV $^{-1}$. The dips correspond to bound states. The spikes are due to nodes in the ${}^1S_0^s$ component of Γ at (W_R, \mathbf{p}_R) . The negative W curve has been calculated with a purely imaginary W .

pion wave function exhibits a most prominent singular behavior in this model; for short distances $\psi_i/x \sim x^{\gamma_i}$ with $\gamma_1 = -0.258$ and $\gamma_2 = -0.966$. Figure 4.4 shows the pion decay constant for various prescriptions. The dotted line labeled with $\psi(a)$ represents f_π calculated by replacing $\psi(x=0)$ in Eq. (4.4.50) by $\psi(a)$. This function shows the divergent behavior $\sim a^{-0.258}$. The broken line labeled with $\langle\psi\rangle_a$ follows from inserting in Eq. (4.4.50) the wave function averaged over a spherical volume of radius a which also diverges as $a^{-0.258}$. Finally the thin lines labeled with $Z_1(a)\langle\psi\rangle_a$ represent renormalized pion decay constants, each corresponding to a different point of renormalization. The figure clearly shows that the limit $a \rightarrow 0$ in Eq. (4.4.56) exists, but that the renormalized decay constant can depend strongly on the choice of renormalization point.

This dependence is elaborated in Fig. 4.5 where the renormalized pion decay constant is plotted as a function of the total mass W_R of the renormalization point. The dips at $W_R = 0.20$ GeV and $W_R = 1.24$ GeV correspond to the bound states of the pion. The vertex function Γ is symmetric in W . The negative W part of the curve in Fig. 4.5 has been calculated by putting a purely imaginary W in the E Γ equations. This represents space-like total four momentum. The dependence of Z_1 on the renormalization mass W_R is small for W_R far from bound state masses and nodes. Unfortunately, there is no natural choice for the renormalization point. The natural

renormalization point of electrodynamics, two free on mass shell fermions emitting a zero momentum boson, has momenta which lie outside the range of momenta possible in the QP approximation. Besides, free quarks do probably not exist. Ito [41] chooses renormalization momenta which correspond to the dynamics of Compton scattering of a zero momentum photon, $(W_R, \mathbf{p}_R) = (0, \mathbf{0})$. For heavy quark systems this point lies in the region of small dependence of Z_1 on W_R , but for the pion this is not a favorable choice because of the proximity of the bound state pole at $W = 0.20$ GeV.

The decay constants presented here are valid for a pion wave function normalized with $\Gamma_{\text{norm}}^{\text{ET}}$ [Eq. (4.1.19)], which guarantees that the pion has unit charge when measured with the ET current. It is also possible to normalize with $\Gamma_{\text{norm}}^{\text{ID}}$ [Eq. (4.1.17)]. The once negative energy states also contribute to the latter norm, and one finds for the pion considered here that the decay constants in the two schemes relate as $f_\pi(\text{ET}) : f_\pi(\text{ID}) = J_0^{\text{ID}} : J_0^{\text{ET}} = 2.24 : 1$. For other mesons the contribution of the once negative energy states is considerably smaller and the norms differ less than 10%.

4.4.3 Calculated annihilation probabilities

The calculated annihilation probabilities presented in this paragraph have not been calculated with the renormalization scheme of the previous subsection. For the mesons in the running coupling constant model, and especially for the heavy mesons, the singular behavior of the WFO is very mild and the numerical inaccuracies in Z_1 are correspondingly large. In view of the uncertainty involved with the choice of renormalization point, we hold the view that the evaluation of Z_1 requires an amount of numerical work which is unproportionally large to the expected increase of reliability of the calculated annihilation rates. Instead the decay is simply calculated by inserting the averaged wave function $\langle \psi \rangle_a$ [Eq. (4.4.62)] in Eq. (4.4.50). For a the averaged Compton length of the two quarks is used,

$$a = \frac{1}{2m_1} + \frac{1}{2m_2}. \quad (4.4.63)$$

The inaccuracies attached to this simple method are probably not bigger than the uncertainties associated with the choice of vertex renormalization point.

In previous Sections the influence of the relativistic dynamics on the meson mass spectrum and the radiative decay width was investigated by starting from the nonrelativistic expressions and consecutively adding the various relativistic ingredients; this analysis may also be repeated for the annihilation decay. For brevity's sake only the pseudoscalar decay constants f_P of the BSLT-Coulomb normalized with J_0^{ET} are considered. They are shown in Fig. 4.6. Figure 4.6(a) shows the nonrelativistic f_P

$$f_P = \frac{\sqrt{3}\sqrt{2}}{\sqrt{M}} \langle {}^1S_0^{++} \rangle_a, \quad (4.4.64)$$

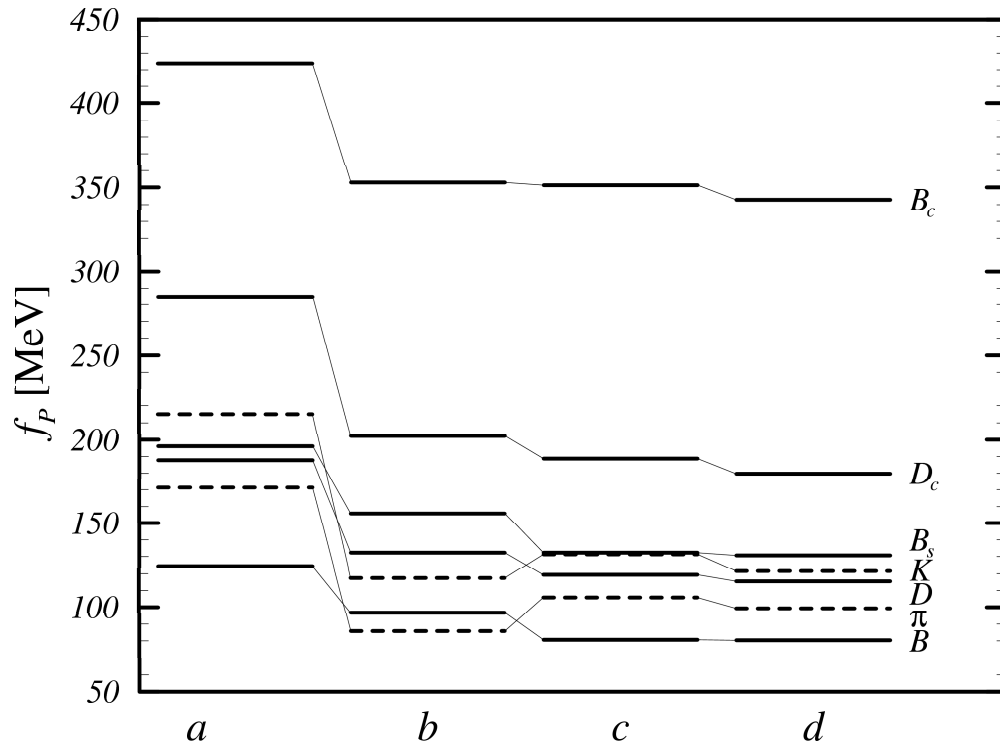


Figure 4.6: Pseudoscalar decay constants calculated from the meson wave functions of the BSLT-Coulomb model. (a) Nonrelativistic annihilation vertex, (b) Full annihilation vertex with $|++\rangle_{\text{pw}}$, (c) Full annihilation vertex with $|++\rangle_{\text{pw}}$, $|+-\rangle_{\text{pw}}$ and $| - + \rangle_{\text{pw}}$, (d) Full annihilation vertex with all states.

Table 4.7: Pseudoscalar decay widths f_P [in MeV] calculated from the models of Chapter 2. Experimental numbers are from [61].

	BSLT Feynman	BSLT Coulomb	ET	Experiment	Ref. [12]
π^\pm	94	100	79	92.5 ± 0.2	
K^\pm	116	122	92	113.0 ± 1.0	
D^\pm	106	116	133	< 220	170 ± 15
D_s	187	180	175		205 ± 15
B^\pm	73	80	89		110 ± 10
B_s	136	131	134		150 ± 15
B_c	367	343	336		290 ± 30

where ${}^1S_0^{++}$ is the positive energy component of the BSLT-Coulomb meson wave function. Since it is usually normalized as $|{}^1S_0^{++}|^2 = 1$ an extra factor $\sqrt{2M}$ is added as compared to Eq. (4.4.61). Performing a full projection of the annihilation vertex on plane wave states leads to replacing

$$\begin{aligned}
{}^1S_0^{++} &\rightarrow -\frac{1}{\sqrt{3}\sqrt{2}} \text{Tr} [\gamma_\mu (1 - \gamma_5) \psi] \\
&= \sqrt{\frac{(m_1 + \omega_1)(m_2 + \omega_2)}{4\omega_1\omega_2}} \left[(1 - \hat{p}_1\hat{p}_2) |{}^1S_0^{++}\rangle_{\text{pw}} - (1 - \hat{p}_1\hat{p}_2) |{}^1S_0^{--}\rangle_{\text{pw}} \right. \\
&\quad \left. + \sqrt{2}(\hat{p}_1 + \hat{p}_2) |{}^3P_0^e\rangle_{\text{pw}} \right], \tag{4.4.65}
\end{aligned}$$

with $\hat{p}_i = p/(m_i + \omega_i)$. Figure 4.6(b) shows the f_P if only the positive energy state ${}^1S_0^{++}$ is taken in Eq. (4.4.65). It differs from Fig. 4.6(a) through the normalization of the wave function and through the factors in Eq. (4.4.65) in front of ${}^1S_0^{++}$. The reduction of the nonrelativistic decay constants is mainly due to these factors. Figures 4.6(c) and 4.6(d) show the pseudoscalar decay constants if the once and double negative energy states are added, respectively. We already pointed out in Section 4.2 that the relativistic corrections to the radiative decay amplitude are partly compensated for by the relativistic corrections to the meson masses. This also happens to the annihilation decay. The meson mass in the denominator of Eq. (4.4.64) causes the ups and downs in the decay constant to be partly compensated for by the ups and downs in the meson mass spectrum [cf. Figs. 3.1 and 3.2]. This again demonstrates the importance of having a vertex that is consistent with the dynamics.

Tables 4.7 and 4.8 list the pseudoscalar decay constants and vector meson decay widths. The predictions for pseudoscalar decay constants of Ref. [12] are also

Table 4.8: Vector meson decay rates $\Gamma(V \rightarrow e^+e^-)$ [in keV] calculated from the models of Chapter 2. Experimental numbers are from [61]. The column labeled $N^{2S+1}L_J$ lists the quantum numbers of the main component of the wave function.

	$N^{2S+1}L_J$	BSLT Feynman	BSLT Coulomb	ET	Experiment
ρ	1^3S_1	1.0	3.41	3.3	6.77 ± 0.32
J/ψ	1^3S_1	8.70	6.73	6.77	5.4 ± 0.4
ψ'	2^3S_1	4.27	3.84	4.13	2.14 ± 0.21
ψ''	1^3D_1	0.08	0.05	0.04	0.26 ± 0.04
ψ'''	3^3S_1	2.66	2.65	2.93	0.75 ± 0.15
ψ^{iv}	2^3D_1	0.09	0.05	0.05	0.77 ± 0.23
ψ^v	4^3S_1	1.8	2.0	2.3	0.47 ± 0.10
Υ	1^3S_1	1.34	1.04	0.94	1.34 ± 0.04
Υ'	2^3S_1	0.82	0.68	0.65	0.57 ± 0.13
Υ''	1^3D_1	0.001	0.001	0.0004	
Υ'''	3^3S_1	0.60	0.54	0.54	0.44 ± 0.07
Υ^{iv}	2^3D_1	0.002	0.001	0.001	
Υ^v	4^3S_1	0.53	0.47	0.47	0.24 ± 0.05
Υ^{vi}	3^3D_1	0.003	0.002	0.001	
Υ^{vii}	5^3S_1	0.5	0.5	0.5	0.31 ± 0.07

shown, who uses the relativized quark model of [29]; the errors list the reliability estimated from the dependence on the model parameters. An overview of other work on f_P can be found in Ref. [12]. All our listed numbers are calculated from wave functions normalized with $\Gamma_{\text{norm}}^{\text{ET}}$. For mesons containing no light quark this normalization differs less than 1% from the $\Gamma_{\text{norm}}^{\text{ID}}$ normalization. For the mesons with light quarks the norms differ less than 3% in the BSLT model, but in the ET model they can differ more, even up to a factor 2 for f_π . The calculated pseudoscalar decay constants f_P agree well with the few that are known. The leptonic decay rates are more sensitive to the strength of the WFO than the f_P , since they depend quadratically on it. Taking that into account one can see from Table 4.8 that the model reproduces most of the vector meson WFO's reasonably well. The model underestimates the ρ decay width $\Gamma(\rho \rightarrow e^+e^-)$. It must be noted that, in contrast to the heavy meson decays, $\Gamma(\rho \rightarrow e^+e^-)$ is considerably influenced by the size a of the volume over which the WFO is averaged. E.g. replacing $a \rightarrow \frac{2}{3}a$ doubles the decay rate. The heavy vector mesons with dominating 3D_1 components (i.e. ψ'' , ψ^{iv} , Υ'' , Υ^{iv} , ...) have only a small admixture of 3S_1 components and should have a small leptonic width. The discrepancies between the calculated and experimental widths for these mesons indicate that the annihilation process is not well modeled or that the assignment of experimental to theoretical excitations is incorrect.

4.4.4 Concluding Remarks

In this Section the annihilation decay of pseudoscalar and vector mesons was investigated in the quasipotential (QP) framework of Chapter 2. The probability of the quark-antiquark annihilation is proportional to the wave function at the origin, which is a divergent quantity in the QP model. We argued that this divergence must be regularized by an annihilation vertex renormalization. This renormalization can be carried out in configuration space and numerical results were given for the pion decay constant. However, in comparing the calculated decay with the experimental decay, we regularized simply by averaging the wave function at the origin over some volume; the inaccuracies attached to this are not bigger than the uncertainties associated with the choice of vertex renormalization point. The various steps that lead from the non-relativistic pseudoscalar decay constant to the QP decay constant were examined. It was noted that their influence on the decay vertex corresponds to their influence on the meson mass spectrum in such a way that they partly compensate each other in the final decay constants. This shows the importance of treating the annihilation vertex and the $q\bar{q}$ dynamics in a consistent way. The calculated pseudoscalar decay constants agreed well with the two experimentally known. The description of the vector meson decay was less satisfying.

Chapter 5

Samenvatting

In 1869 realiseerde Mendelejev zich dat de scheikundige elementen grote regelmaat vertonen in hun eigenschappen, en hij groepeerde ze in het periodiek systeem der elementen. Met behulp van zijn systeem konden voorspellingen gedaan worden over scheikundige eigenschappen en over mogelijke nieuwe elementen. Later werd aangetoond dat de regelmaat van het periodiek systeem voortkomt uit een klein aantal bouwstenen —de protonen, neutronen en elektronen— waaruit alle mogelijke atomen kunnen worden gevormd. Lang werd aangenomen dat protonen en neutronen elementair en ondeelbaar waren. Echter, in de loop van de tijd werden steeds meer elementaire deeltjes ontdekt die bijdragen aan de krachten tussen protonen en neutronen, zoals pionen, kaonen en rho-deeltjes.

Uiteindelijk werden de meeste nieuwe elementaire deeltjes in de jaren zestig gegroepeerd in het quarkmodel. Met behulp van het quarkmodel konden voorspellingen gedaan worden over reactiewaarschijnlijkheden en over mogelijke nieuwe deeltjes. Het quarkmodel wordt tegenwoordig algemeen aanvaard. Volgens dit model komt de regelmaat van de meeste elementaire deeltjes voort uit een zestal nog elementairdere quarks waaruit deze deeltjes zijn opgebouwd. Zulke deeltjes die uit quarks bestaan worden hadronen genoemd. (Sommige deeltjes zoals de gluonen, die de bindende krachten tussen de quarks overbrengen, en de elektronen bestaan niet uit quarks, maar worden net als quarks als elementair beschouwd.) De hadronen worden onderverdeeld in twee groepen. De grotere hadronen zoals protonen en neutronen heten baryonen. Volgens het quarkmodel bestaan zij uit drie quarks. De lichtere hadronen, zoals pionen of kaonen, zijn de mesonen en zij bestaan volgens het model uit twee quarks. In dit proefschrift staan de mesonen centraal.

In het begin van de zeventiger jaren werd een sluitend theoretisch model opgesteld dat de wisselwerkingen beschrijft tussen alle bekende deeltjes (behalve gravitonen). In dit model wordt het quarkmodel gecombineerd met de speciale relativiteitstheorie en de quantummechanica. Deze combinatie wordt de quantum-chromodynamica (QCD)

genoemd. De ontdekking van QCD is een belangrijke stap vooruit voor het quark-model omdat QCD in principe precies aangeeft hoe de quarkbanen in de hadronen uitgerekend moeten worden. Uit deze banen kunnen met grote nauwkeurigheid alle eigenschappen van de hadronen worden afgeleid, zoals hun grootte, massa, en gedrag in kernreacties.

Het probleem van QCD is dat de bijbehorende vergelijkingen zo moeilijk zijn, dat er nog geen oplosmethode voor bekend is. Om toch op basis van QCD berekeningen te kunnen maken, worden altijd sommige aspecten van QCD weggelaten of vereenvoudigd. De verschillende vereenvoudigingen leiden tot verschillende soorten van praktisch bruikbare quarkmodellen. Veel gebruikte modellen zijn het rooster-quarkmodel, het quark-zakmodel en het niet-relativistische bouwsteen-quarkmodel.

De hadroneigenschappen worden met het meeste succes beschreven door het niet-relativistische bouwsteen-quarkmodel, waarvoor de belangrijkste ontwikkelingen waren in de periode 1975 – 1985. In dit model worden twee benaderingen van QCD gecombineerd, waardoor mesoneigenschappen eenvoudig kunnen worden berekend met het oplossen van de Schrödingervergelijking voor de twee quarks. De eerste benadering is de bouwsteen-benadering, die tot het bouwsteen-quarkmodel leidt. De volgende benadering is de niet-relativistische benadering, en deze vereenvoudigt het model verder tot het niet-relativistische bouwsteen-quarkmodel.

In de bouwsteen-benadering wordt gebruik gemaakt van het eenvoudige beeld van elementaire en onveranderbare quarks. Volgens QCD kunnen de vorm en massa's van quarks ingrijpend veranderd worden door de sterke krachten tussen de gluonen en de quarks. De vergelijkingen die deze verzwaringen en vervormingen beschrijven, zijn echter te moeilijk om exact op te lossen. Daarom wordt meestal gebruik gemaakt van het vereenvoudigde beeld van twee of drie elementaire en onveranderbare quarks. Om onderscheid te maken met de quarks uit QCD worden deze quarks bouwsteen-quarks genoemd. Men denkt dat deze vereenvoudiging weinig invloed heeft op de berekening van hadroneigenschappen.

In de niet-relativistische benadering worden de door relativiteitstheorie voorgeschreven effecten verwaarloosd. Volgens de relativiteitstheorie is er geen absoluut oordeel mogelijk is over begrippen zoals 'tegelijkertijd' en 'op dezelfde plaats'. Iedere waarneemer heeft hier zijn eigen relatieve oordeel over. De mate waarin twee personen verschillend oordelen neemt toe naarmate hun snelheid ten opzichte van elkaar toeneemt. De quarksnelheden zijn zo groot dat zulke oordelen een factor twee kunnen verschillen. De relativiteitstheorie kan elegant geformuleerd worden in een vierdimensionale ruimte, waarin de tijdrichting hetzelfde wordt behandeld als de drie ruimterichtingen. De verschillende meningen over 'tegelijkertijd' en 'op dezelfde plaats' worden dan verschillende meningen over welke van de vier richtingen de tijdrichting is. Het verschil in mening heeft een bijzonder gevolg voor de quarkeigenschap die spin heet. Door deze eigenschap gedragen quarks zich in veel opzichten alsof ze draaien rond hun eigen lengte-as. Omdat er geen absoluut oordeel is over

welke richting de tijdrichting is en welke de ruimterichtingen zijn, bestaat er ook geen absoluut oordeel over wat een draaiing rond de lengte-as is, en wat een draaiing rond de tijdas. Dirac leidde af dat een draaiing van een quark rond zijn tijdas overeenkomt met een gedeeltelijke overgang van het quark naar toestanden die kenmerkend zijn voor antiquarks. Zo kon hij de antideeltjes van de elektronen voorstellen, die later inderdaad werden gevonden. De verschillende soorten draaiingen kunnen elegant beschreven worden in een eveneens vier-dimensionale ruimte, die de Diracruimte wordt genoemd. In de Diracruimte worden de twee draairichtingen in de ruimte (linksom en rechtsom) hetzelfde behandeld als de twee draairichtingen in de tijd (quarkachtig en antiquarkachtig). De relativistische effecten voor het quarkmodel zijn dat de vergelijkingen voor de quarkbanen niet alleen in de drie ruimterichtingen moeten worden opgelost, maar ook in de vierde tijdrichting en ook in de volledige Diracruimte.

In dit proefschrift wordt het effect van de niet-relativistische benadering op het bouwsteen-quarkmodel voor mesonen onderzocht. Dit onderzoek is interessant vanwege twee redenen.

Ten eerste is het interessant omdat er een tegenspraak lijkt te zijn tussen de schattingen van de relativistische effecten voor mesonen en de nauwkeurigheid van het niet-relativistische model. Deze schattingen, gebaseerd op de verwachte snelheden van de quarks, geven aan dat de uitkomsten van het niet-relativistische bouwsteen-quarkmodel ingrijpend kunnen veranderen als de relativistische effecten in rekening worden gebracht. Derhalve kan men een overeenkomstige afwijking verwachten tussen de met dit model berekende mesoneigenschappen en de gemeten mesoneigenschappen. De werkelijke afwijking blijkt veel kleiner te zijn. Dit kan betekenen dat iets wezenlijks in QCD verkeerd wordt begrepen. Door de rol van de relativistische effecten te onderzoeken, kan hier wellicht meer duidelijkheid in worden gebracht.

Ten tweede is het onderzoek interessant omdat het kan leren in hoeverre de verwaarlozing van de relativistische effecten de betrouwbaarheid van het bouwsteen-quarkmodel vermindert. Stel dat iemand een verschil vindt tussen een meting en een berekening van de kans op een bepaald soort botsingen tussen elektronen en protonen. Dit kan betekenen dat in de berekening bepaalde reactiestappen vergeten zijn, maar het verschil kan ook veroorzaakt worden door de gemaakte benaderingen van QCD. Om de eerste en interessantste mogelijkheid als de juiste te kunnen aanwijzen en de tweede mogelijkheid uit te sluiten moet de betrouwbaarheid van het niet-relativistische model bekend zijn.

De beste manier om de relativistische effecten te onderzoeken is door het volledige bouwsteen-model door te rekenen, dus zonder deze effecten weg te laten. Zo'n berekening is moeilijk vanwege twee problemen.

Het eerste probleem ontstaat doordat in zo'n berekening naast de relativiteitstheorie ook de quantummechanica in beschouwing moet worden genomen. Vol-

gens de quantummechanica gedraagt elk deeltje zich als een golfpakketje (golfquantum), waardoor het deeltje tegelijkertijd op meerdere plaatsen kan wisselwerken met andere deeltjes. De quantummechanische quarkbanen zijn moeilijker uit te rekenen dan de niet-quantummechanische omdat ze tegelijkertijd de kans moeten beschrijven op alle mogelijke posities van de quarks. Dit zijn niet alleen alle mogelijke plaatsen in de drie ruimterichtingen, maar ook nog de plaatsen in de tijdrichting en in de Diracruimte. Hierdoor kost het uitvoeren van zo'n berekening veel tijd.

Het tweede probleem ontstaat door het bijzondere lange-afstandsgedrag van de krachten tussen de quarks. Dit zit als volgt. De baan van een quarkgolf kan vastgelegd worden door voor iedere plaats aan te geven hoe groot de kans is om het quark daar te vinden. Het is ook mogelijk de baan vast te leggen door voor iedere mogelijke frequentie (d.w.z. trillingssnelheid) van de quarkgolf aan te geven hoe de grootte van de kans is om het quark met die frequentie te vinden. Beide beschrijvingen verschillen totaal van elkaar, maar bevatten dezelfde informatie. De ene beschrijving kan in de andere omgezet worden met een Fourier-transformatie. In het relativistische quarkmodel blijken er bezwaren tegen beide beschrijvingen te zijn. Enerzijds, de relativistische effecten hangen af van de trillingssnelheden van de quarks, en men gelooft dat een beschrijving in termen van plaatskansen hierdoor erg moeilijk wordt. Anderzijds, er zijn nog nooit afzonderlijke quarks waargenomen; ze blijken alleen in groepjes van twee of drie voor te komen. Dit betekent dat een losse quark altijd naar een andere quark moet worden toegetrokken, ongeacht hoe ver ze van elkaar verwijderd zijn. Daarom mogen de krachten tussen de quarks niet afnemen als de afstand toeneemt. Als nu de trillingssnelheid van een quarkgolf kleiner wordt, worden zijn golven langer en neemt hun uitgestrektheid toe. Dit betekent ook dat ze over een steeds groter gebied de aantrekkende kracht van het andere quark gaan voelen, omdat deze kracht niet verdwijnt op grote afstand. Als de frequentie van de golf nul wordt, wordt de kracht erop oneindig groot. Een beschrijving van de bijbehorende golfvergelijkingen met frequentiekansen wordt dan moeilijk.

Het werk voor dit proefschrift bestond uit drie delen.

Het eerste deel was gericht op het vinden van oplossingen voor de twee bovengenoemde problemen die het maken van de volledige relativistische berekeningen bemoeilijken. Het probleem van het lange-afstandsgedrag verdween toen we een Fourier-transformatie vonden die tot een beschrijving in termen van plaatskansen leidde. Deze beschrijving bleek veel eenvoudiger te kunnen dan algemeen werd gedacht. Daardoor bleef voldoende tijd over om het eerste probleem gedeeltelijk op te lossen, namelijk de uitbreiding van het quarkmodel voor bewegingen in de Diracruimte. Het is ons als eerste gelukt een dergelijke berekening voor een systeem van twee quarks uit te voeren. Het viel echter buiten het bestek van dit proefschrift om het quarkmodel ook uit te breiden voor bewegingen in de tijdrichting. We denken dat de bewegingen in de Diracruimte aanzienlijk belangrijker zijn dan die in de tijdrichting.

Het tweede deel van dit werk bestond uit het omzetten van de beschrijving in termen van plaatskansen naar een voor de computer hanteerbare vorm. Dit is gedaan met de hand en met computerprogramma's voor algebraïsche manipulaties. Daarna werd een computerprogramma geschreven dat de omgezette beschrijving voor de quarkbanen, die bestond uit een stelsel van acht gekoppelde differentiaal-integraalvergelijkingen, numeriek oploste.

Het laatste deel bestond uit het interpreteren van de gevonden relativistische quarkbanen, en uit het maken van een vergelijking met de niet-relativistische banen. Dit leidde tot de volgende resultaten.

Als eerste resultaat is gevonden dat, zoals verwacht op basis van ruwe schattingen, de relativistische effecten grote veranderingen geven in mesoneigenschappen, zoals bijvoorbeeld massa. Maar voor bijna ieder meson zijn de veranderingen even groot, en hun onderlinge verhoudingen worden weinig veranderd. De figuren 3.1 tot en met 3.4 laten dit goed zien. In deze figuren geeft iedere lijn de massa van een meson aan. Per figuur worden kolommen getoond, die ieder een aantal meson-massa's laten zien die uitgerekend zijn door meer of minder met de relativistische ingrediënten rekening te houden. Tussen de kolommen kunnen de massa's veel verschillen, maar het patroon blijft hetzelfde. Daarom kan het niet-relativistische model het patroon ook goed beschrijven. Een dergelijk behoud van het patroon blijkt ook bij andere mesoneigenschappen. Dit resultaat brengt meer duidelijkheid in de schijnbare tegenspraak tussen de schattingen van de relativistische effecten voor mesonen en de nauwkeurigheid van het niet-relativistische model.

Als tweede resultaat is meer duidelijkheid geschapen over de betrouwbaarheid van het niet-relativistische model. De betrouwbaarheid kan afgeleid worden uit de figuren 3.1 tot en met 3.4. De patronen en verhoudingen van mesoneigenschappen blijven ongeveer hetzelfde onder de relativistische veranderingen. De uitspraken van het niet-relativistische model over de onderlinge verhoudingen van de mesoneigenschappen zijn dus waarschijnlijk betrouwbaar. De positie en grootte van deze patronen hangen daarentegen af van de relativistische ingrediënten, zodat de uitspraken van het niet-relativistische model over de parameters die de positie en grootte bepalen waarschijnlijk minder betrouwbaar zijn. Dit zijn vooral de parameters die de sterkte van de kracht tussen de quarks, dus van de gluonen, beschrijven. De berekeningen geven aan dat deze kracht bijna twee keer zo groot moet zijn als werd gedacht op grond van het niet-relativistische model, en dat de rol van de spin van de gluonen op grote afstand veel belangrijker is dan werd gedacht.

Bibliography

- [1] T.A. Armstrong *et al.* (E760 collaboration), Phys. Rev. Lett. 69 (1992) 2337.
- [2] J. Babcock and J.L. Rosner, Phys. Rev. D 14 (1976) 1286; J.L. Rosner, *ibid.* D 23 (1981) 1127.
- [3] M. Bander, D. Silverman, B. Klima and U. Maor, Phys. Rev. D 29 (1984) 2038.
- [4] A. Bastai, L. Bertocchi, S. Fubini, G. Furlan and M. Tonin, Nuovo Cim. 30 (1963) 1512.
- [5] C.J. Bebek *et al.*, Phys. Rev. D 17 (1978) 1693.
- [6] W. Bentz, Nucl. Phys. A446 (1985) 678.
- [7] H.A. Bethe and E.E. Salpeter, Quantum Mechanics of one- and two-electron Atoms (Plenum, New York 1977).
- [8] see e.g. J.D. Bjorken and S.D. Drell, Relativistic Quantum Mechanics (McGraw-Hill, New York 1964).
- [9] R. Blankenbecler and R. Sugar, Phys. Rev. 142 (1966) 1051; A.A. Logunov and A.N. Tavkhelidze, Nuovo Cim. 29 (1963) 380.
- [10] G.E. Brown and A.D. Jackson, The Nucleon-Nucleon Interaction (North-Holland, Amsterdam 1976).
- [11] M. Chachkhunashvili, T. Kopaleishvili, Few-Body Systems 6 (1989) 1; A. Archvadze, M. Chachkhunashvili and T. Kopaleishvili, *ibid.* 14 (1993) 53.
- [12] S. Capstick and S. Godfrey, Phys. Rev. D 41 (1990) 2857.
- [13] S. Capstick, Phys. Rev. D 46 (1992) 1965; *ibid.* 2864.
- [14] C.E. Carlson and J. Milana, Phys. Rev. Lett. 65 (1990) 1717; R. Kahler and J. Milana, Phys. Rev. D 47 (1993) 3690.

- [15] M. Ciafaloni, Phys. Rev. 176 (1968) 1898.
- [16] F.E. Close and Zhenping Li, Phys. Rev. D 42 (1990) 2192; Zhenping Li and F.E. Close, *ibid.* 2207.
- [17] E.D. Cooper and B.K. Jennings, Nucl. Phys. A 500 (1989) 553.
- [18] H.W. Crater and P. Van Alstine, Phys. Rev. Lett. 53 (1984) 1527, Phys. Rev. D 37 (1988) 1982.
- [19] F. Daghighian and D. Silverman, Phys. Rev. D 36 (1987) 3401.
- [20] F.B. Dally *et al.*, Phys. Rev. Lett. 48 (1982) 375.
- [21] N.K. Devine and S.J. Wallace, U. of MD. preprint 93-174 (1993).
- [22] L. Durand, P.C. DeCelles and R.B. Marr, Phys. Rev. 126 (1962) 1882.
- [23] G.R. Farrar and D.R. Jackson, Phys. Rev. Lett. 43 (1979) 246.
- [24] G. Feldman, T. Fulton and J. Sucher, Phys. Rev. D 21 (1980) 845.
- [25] D. Flamm and F. Schöberl, Introduction to the Quark Model of elementary Particles (Gordon and Breach, New York 1982).
- [26] J. Fleischer and J.A. Tjon, Nuc. Phys. B 84 (1975) 375, Phys. Rev. D 15 (1977) 2537, *ibid.* D 21 (1980) 87.
- [27] J.L. Gammel, M.T. Menzel and W.R. Wortman, Phys. Rev. D 3 (1971) 2175.
- [28] A. Gara, B. Durand, L. Durand and L.J. Nickish, Phys. Rev. D 40 (1989) 843; A. Gara, B. Durand and L. Durand, *ibid.* D 42 (1990) 1651.
- [29] S. Godfrey and N. Isgur, Phys. Rev. D 32 (1985) 189; S. Capstick and N. Isgur, *ibid.* D 34 (1986) 2809.
- [30] M.L. Goldberger, D.E. Soper and A.H. Guth, Phys. Rev. D 14 (1976) 1117.
- [31] D. Gromes, Phys. Lett. B 202 (1988) 262.
- [32] F. Gross and J. Milana, Phys. Rev. D 43 (1991) 2401; *ibid.* D 45 (1992) 969.
- [33] K.K. Gupta, A.N. Mitra and N.N. Singh, Phys. Rev. D 42 (1990) 1604, and references in there.
- [34] A.H. Guth and D.E. Soper, Phys. Rev. D 12 (1975) 1143.
- [35] A.B. Henriques, B.H. Kellett and R.G. Moorhouse, Phys. Lett. B 64 (1976) 85.

- [36] H. Hersbach, Phys. Rev. A 46 (1992) 3657.
- [37] H. Hersbach, Phys. Rev. D 47 (1993) 3027; Utrecht preprint THU-93/13.
- [38] M. Hirano, K. Iwata, K. Kato, T. Murota and D. Tsuruda, Prog. Theor. Phys. 69 (1983) 1498; C. Yoshida-Habe, K. Iwata, M. Hirano, T. Murota and D. Tsuruda, Prog. Theor. Phys. 86 (1991) 703, and references in there.
- [39] E. Hummel and J.A. Tjon, Phys. Rev. C 42 (1990) 423.
- [40] N. Isgur and C.H. Llewellyn Smith, Nucl. Phys. B 317 (1989) 526.
- [41] H. Ito, Prog. Theor. Phys. 67 (1982) 1553, *ibid.* 70 (1983) 499, *ibid.* 78 (1987) 978, *ibid.* 80 (1988) 874, *ibid.* 84 (1990) 94.
- [42] O.C. Jacob and L.S. Kisslinger in Nuclear and Particle Physics on the Light Cone, Proceedings of the LAMPF Workshop, Los Alamos 1988 (World Scientific, Singapore, 1989); Phys. Lett. B 243 (1990) 323.
- [43] P. Jain and H.J. Munczek, Phys. Rev. D 44 (1991) 1873; H.J. Munczek and P. Jain, *ibid.* D 46 (1992) 438.
- [44] J.G. Körner, D. Pirjol and K. Schilcher, Phys. Rev. D 47 (1993) 3955.
- [45] J.J. Kubis, Phys. Rev. D 6 (1972) 547.
- [46] W. Kwong, J.L. Rosner and C. Quigg, Ann. Rev. of Nucl. Part. Sci. 37 (1987) 325.
- [47] J.-F. Lagaë, Phys. Lett. B 240 (1990) 451, Phys. Rev. D 45 (1992) 305, *ibid.* 317.
- [48] G.P. Lepage and S.J. Brodsky, Phys. Rev. D 22 (1980) 2157.
- [49] R. Levine and Y. Tomozawa, Phys. Rev. D 19 (1979) 1572.
- [50] A. Le Yaouanc, L.L. Oliver, O. Pène and J.-C. Raynal, Hadron Transitions in the Quark Model (Gordon and Breach, New York 1988).
- [51] C.H. Llewellyn Smith, Ann. of Phys. 53 (1969) 521.
- [52] W. Lucha, F.F. Schöberl and D. Gromes, Phys. Rep. 200 (1991) 127.
- [53] see page 224 of Ref. [52].
- [54] D. Lurié, Particles and Fields (Interscience, New York 1968).
- [55] A.J. MacFarlane, Rev. Mod. Phys. 34 (1962) 41.

- [56] V.B. Mandelzweig and S.J. Wallace, Phys. Lett. B 197 (1987) 469.
- [57] E. Merzbacher, Quantum Mechanics 2nd ed. (Wiley, New York 1970), and references in there.
- [58] T. Murota, Prog. Theor. Phys. 69 (1983) 181.
- [59] J.W. Norbury, D.E. Kahana and K.M. Maung, Can. J. Phys. 70 (1992) 86; K.M. Maung, D.E. Kahana and J.W. Norbury, Phys. Rev. D 47 (1993) 1182.
- [60] P.J. O'Donnell, Rev. of Mod. Phys. 53 (1981) 673.
- [61] Particle Data Group, K. Hikasa *et al.*, Review of particle properties, Phys. Rev. D 45 (1992) S1.
- [62] G.L. Payne in Models and Methods in Few-Body Physics (Springer, Berlin 1987); H. Kröger, R.J. Slobodrian and G.L. Payne, Phys. Rev. C 37 (1988) 486.
- [63] J. Praschifka, R.T. Cahill and C.D. Roberts, Int. J. Mod. Phys. A 4 (1989) 4929.
- [64] J.L. Richardson, Phys. Lett. B 82 (1979) 272.
- [65] E.E. Salpeter, Phys. Rev. 87 (1952) 328.
- [66] C. Schwartz and C. Zemach, Phys. Rev. 141 (1966) 1454.
- [67] Yu.A. Simonov, V.D. Mur, V.S. Popov and V.P. Yurov, ITEP preprint (1992).
- [68] P.C. Tiemeijer and J.A. Tjon, Phys. Rev. C 42 (1990) 599.
- [69] P.C. Tiemeijer and J.A. Tjon, Phys. Lett. B 277 (1992) 38.
- [70] P.C. Tiemeijer and J.A. Tjon, Utrecht preprint THU-92/31 (1992).
- [71] P.C. Tiemeijer and J.A. Tjon, Utrecht preprint THU-93/12 (1993), to be published in Phys. Rev. C.
- [72] J.R. Spence and J.P. Vary, Phys. Rev. D 35 (1987) 2191; Phys. Rev. C 47 (1993) 1282.
- [73] S.J. Wallace in Nuclear and Particle Physics on the Light Cone, Proceedings of the LAMPF Workshop, Los Alamos 1988 (World Scientific, Singapore, 1989).
- [74] S.J. Wallace and V.B. Mandelzweig, Nucl. Phys. A 503 (1989) 673.
- [75] G.C. Wick, Phys. Rev. 96 (1954) 1124.
- [76] M.J. Zuilhof and J.A. Tjon, Phys. Rev. C 22 (1980) 2369.

Curriculum vitae

De auteur werd geboren op 4 februari 1966 te Son en Breugel. Vanaf 1978 bezocht hij het Eindhovens Protestants Lyceum, waar hij het diploma Gymnasium β behaalde in juni 1984. Daarna studeerde hij aan de Rijksuniversiteit te Utrecht, en kreeg hij de propaedeuse natuurkunde (cum laude) in juni 1985. Voor het experimentele deel van zijn afstudeerwerk bestudeerde hij op NIKHEF-K de reactie ${}^6\text{Li}(e,e'p)$, en voor het theoretische deel analyseerde hij verschillende beschrijvingen voor de ladingsverdelingen van niet-vrije nucleonen. Dit leidde tot een doctoraal diploma natuurkunde (cum laude voor zowel de richtingen experimentele natuurkunde als theoretische natuurkunde) in mei 1989. Hierna kwam hij als Onderzoeker in Opleiding in dienst van de Stichting Fundamenteel Onderzoek der Materie en werkte aan het Instituut voor Theoretische Fysica te Utrecht. Hier deed hij berekeningen aan de ladingsverdelingen van niet-vrije nucleonen, en daarnaast verrichtte hij het in dit proefschrift beschreven onderzoek.

In spite of the various simplifications in the picture on the front cover (from Luca Cambiaso), it is not trivial to establish the relations between all persons. In the situation shown the falling persons are mainly concerned with their velocity. Nevertheless the global scene is best described by specifying all positions. All this has a clear correspondence with quark dynamics.

Het promotiewerk heb ik gelukkig niet hoeven te doen in eenzame afzondering, en daarom wil ik hier de collega's van het Instituut voor Theoretische Fysica bedanken voor de verschillende manieren waarop zij dit hebben voorkomen. In het bijzonder bedank ik John Tjon, die niet alleen aangename gesprekken over van alles voerde, maar die vooral gevraagd en ongevraagd een verbazingwekkende hoeveelheid kennis beschikbaar stelde die erg waardevol en stimulerend was voor dit werk. Tevens bedank ik Joost voor de bereidheid op elk moment elk onderwerp te bespreken. Hans en Theo bedank ik voor de aangename gedachtenwisselingen over quarkmodellen. Alle collega's, vooral de promovendi, bedank ik voor hun behulpzaamheid en gezelligheid tijdens werk, pauze en andere sociale gebeurtenissen.